PhD thesis

Constraints on Primordial Magnetic Fields with Cosmic Microwave Background and 21-cm Line Observations

Teppei Minoda

Department of Physics and Astrophysics, Nagoya University

February 11, 2021

Abstract

While the existence of the magnetic fields in galaxies and galaxy clusters is reported, their origin is still unknown. An attractive scenario is that the Primordial Magnetic Fields (PMFs), which are the tiny seed fields generated in the early universe, evolve to become the astrophysical magnetic fields. However, the PMFs are not yet confirmed observationally, and it is an open question that whether or not the PMFs exist, and how their strength is. To solve this problem, many efforts have been made to investigate the observational signatures of the PMFs. Currently, the upper limits on the PMFs are given by the Cosmic Microwave Background (CMB) and the Large-Scale Structure (LSS) observations. The purpose of this thesis is to discuss the improvement of the PMF constraints with the latest and future CMB observations and a new cosmological probe, HI 21-cm line global signal measurement.

First, we revisit the impact of the PMFs on the primary CMB anisotropies. We calculate the baryon velocity perturbations induced by the Lorentz force due to the PMFs before the CMB decoupling from baryons. We especially focus on perturbations of smaller scales than the mean free path of CMB photons, which are not discussed in the previous studies. We find the PMFs enhance the CMB anisotropies on such small scales. As a result, an improved constraint on the PMF strength is obtained from the CMB observations of Planck and South Pole Telescope (SPT).

Next, we investigate the secondary CMB anisotropies created by the PMFs after the decoupling epoch. One of the important generation mechanisms of the secondary CMB anisotropies is the thermal Sunyaev-Zel'dovich effect (tSZ effect), which is the inverse-Compton scattering by hot electron gas. The PMFs create the gas density fluctuations through the Lorentz force, and heat up gas due to the so-called ambipolar diffusion. The resultant fluctuations of gas density and temperature depending on the PMF structure create the CMB anisotropies via the tSZ effect. We calculate the time evolutions of the gas density and temperature by a numerical simulation including the Lorentz force and MHD dissipation effect. Then, we evaluate the CMB temperature anisotropies from the tSZ effect. The PMFs strongly affect the thermal history of baryon gas in low-density regions, and create significant CMB anisotropies on very small angular scales around 1 arc second.

Furthermore, we discuss the impact of the PMFs on the redshifted HI 21-cm line observation. In the cosmological context, the observation of the redshifted 21-cm line can probe the cosmic history of the baryon gas temperature in the Cosmic Dawn (CD) and the Epoch of Reionization (EoR). The PMFs can strongly affect the baryon gas thermal history during these periods through their energy dissipation. We calculate the baryon gas temperature history including the heating due to the PMF dissipation until the EoR. The recent 21-cm line signal measurement by Experiment to Detect the Global EoR Signature (EDGES) gives a clue to the thermal history of baryon gas around the CD and EoR. Employing the measurement of EDGES, we can set the stringent upper limit on the PMFs, which is less than sub-nano Gauss.

For future prospects, our results suggest that the constraints on the PMFs can be improved more from future CMB and 21-cm line observations such as CMB-S4, and Square Kilometre Array (SKA). Additionally, the possible existence of small-scale density structure induced by the Lorentz force of the PMFs, which we find, might be checked by the on-going or next-generation observations of LSS, for examples, Hyper Suprime-Cam (HSC), Vera C. Rubin Observatory's Legacy Survey of Space and Time (LSST), Euclid, and so on.

Acknowledgment

First of all, I sincerely thank to Professor Naoshi Sugiyama, who is my supervisor, the PI of C-lab, and the Provost of Nagoya University. He taught me the basic of the cosmology, the ideal attitude as a scientist, and assisted my PhD research so much economically and scientifically.

Next, I am really grateful for my other collaborators. Tomo Takahashi, who is a professor in Saga University, gave me an essential idea of the PMF constraint with 21-cm global signal, and carefully helped me to publish a paper. Kiyotomo Ichiki, an associate professor in C-lab, has brought me not only scientific knowledges, but a lot of analytic and numerical calculation techniques. In particular, I frequently asked him about the usage of the numerical Boltzmann code, `CosmoMC`. I always discussed with Assist. Prof. Hiroyuki Tashiro when I had troubles about the researches, studying, academic career, and daily life. Dr. Kenji Hasegawa also gave me a wide knowledge about the astrophysics, numerical calculations, and academic society.

I also grateful for many researchers, Jens Chluba, Alexander Kusenko, Koji Yoshikawa, Hidenobu Yajima, Shohei Saga, Koichiro Horiguchi for the fruitful discussions and useful advices. I also appreciate academic staffs in C-lab, Takahiko Matsubara, Shuichiro Yokoyama, Atsushi J Nishizawa, Atsushi Nishizawa, Yuko Urakawa, Sachiko Kuroyanagi, Hironao Miyatake, Naoya Kitajima, Takeshi Kobayashi, Daisuke Nitta, Jean-Baptiste Durrive, Daichi Kashino, Yuichiro Tada, for discussion in weekly seminar and coffee break. I thank all students of C-lab (and Ω-lab and Ta-lab) who I have shared a lot of time with during my PhD course, especially Mutsumi Minoguchi and Toshiyuki Tanaka. I am profoundly grateful for the secretaries in C-lab, Hitomi Tanaka and Mio Kato, who carefully developed our research environment.

Finally, I thank my dear parents and sisters to complete this thesis.

Contents

Chapter 1

Introduction

1.1 Magnetic fields present everywhere

Magnetic fields exist on different scales in the universe. Figure 1.1 shows the typical strength of magnetic fields of various astrophysical objects with different scales, e.g., planets, ordinary stars, compact objects, molecular clouds, interstellar medium, galaxies, galaxy clusters, and superclusters [1]. These magnetic fields with astrophysical objects are measured in several different ways. For example, the synchrotron radiation is caused by free electrons spirally moving around magnetic field lines. The polarization of an electromagnetic wave is also useful to measure magnetic fields because an electromagnetic wave is scattered by aligned dust grains, which are the tracers for magnetic fields. Observed polarization is also affected by Faraday rotation, which is the rotation effect of an electromagnetic wave polarization plane during its propagation through the magnetized medium. The measurement of the Zeeman effect is another traditional method, which is the splitting of energy levels occurred by the interaction between charged particles spins and the magnetic fields. Although a wide variety of astrophysical objects are found to be magnetized by the methods introduced above, the origin and evolution of the cosmic magnetic fields are still mysterious. Especially, the large-scale magnetic fields with galaxies, galaxy clusters, and superclusters invoke the interest of people because such magnetic fields are possibly connected to the physics in the early universe or the particle physics beyond the Standard Model. Therefore, we focus on the magnetic fields with larger scales than galaxies (~ 10 kpc) in this thesis.

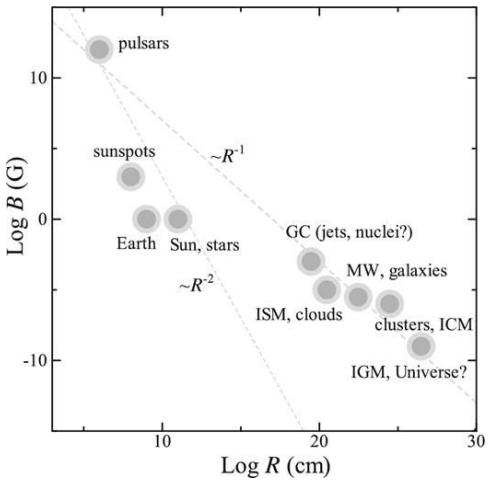

Figure 1.1: The typical strength of magnetic fields are shown versus scales of various objects which they accompany. GC, ISM, MW, ICM, and IGM are the abbreviations for Globular Clusters, Interstellar Medium, Milky Way, Intracluster Medium, and Intergalactic Medium, respectively. Horizontal and vertical axes represent the physical scale of astronomical objects R and strength of magnetic fields B, respectively. (This figure is referred from literature [1].)

1.1.1 Magnetic fields in galaxies and galaxy clusters

Magnetic fields present in many galaxies including the Milky Way [2]. In the 1960s, the first observations of the magnetic fields inside our Galaxy have been made by the measurements of the optical and radio linear polarization and the synchrotron emission [3,4]. More detailed observations have carried out after that, and they have found the structure of the Galactic magnetic fields; magnetic fields along the spiral arms and randomly distributed fields inside the disk region [5–7]. Moreover, many studies have reported the existence of magnetic fields in extragalaxies [8,9] and in galaxy clusters [10]. The typical strength of galactic magnetic fields is a few μG [11–14], and the field strength of galaxy clusters is around 1 μG [15–18]. For much larger scales, Virgo supercluster, Perseus-Pisces supercluster, and Hercules superclusters are reported to be magnetized as 0.5 μG [19–22]

1.1.2 Magnetic fields in the intergalactic medium

It is difficult to probe magnetic fields in the intergalactic region in direct ways mentioned above. Instead, the magnetic fields of strength 10^{-18}–10^{-15} G in the intergalactic region are suggested by the high energy γ-ray observations indirectly [23–29]. These studies estimate the strength of intergalactic magnetic fields based on rapidly repeated GeV γ-ray from blazars and so on, Although MeV and GeV γ-ray is considered to travel to the earth with almost no scatterings, TeV γ-ray scatters with the surrounding low-energy photons from galaxies during propagation, and the pair creation of relativistic electrons and positrons occurs. Then, high-energy charged particles produced from TeV γ-ray inject energy into surrounding photons through inverse-Compton scattering, and then the photons gained energy reach to the earth as cascaded GeV γ-rays. Here, if magnetic fields exist in the intergalactic region, the propagation of the produced electrons and positrons can be bent, and the arrival time of the cascaded γ-ray is expected to be delayed. Thus, in the presence of the intergalactic magnetic fields, in addition to the GeV γ-ray emitted by high-energy objects and reaching the Earth directly, the delayed GeV γ-ray that receives energy from high-energy charged particles should be observed. This hypothetical repeated γ-ray emissions due to the intergalactic magnetic fields is called "pair echo", and proposed by Plaga in 1995 [30]. Afterward, γ-ray observation data with *Fermi* put a constraint on the pair echo flux [27], and they have suggested that intergalactic magnetic fields on 1 kpc scale are $B_{1\ \mathrm{kpc}} \gtrsim 10^{-20.5}$ G. The cascade of the γ-ray energy spectra emitted from blazars have also put lower limits on the intergalactic magnetic fields as $B \gtrsim 10^{-16}$–10^{-15} G [24, 31]. Besides, the bending effect due to the intergalactic magnetic fields can introduce multiple trajectories of the cascaded γ-ray photons to us. As a result, it causes the "pair-halo" of cascaded γ-ray signals from a point source [32]. These pair-halo signals have been applied to estimate intergalactic magnetic fields as $B \approx 10^{-15}$ G in 2010 [23], and 5 years later as 10^{-17} G $\lesssim B \lesssim 10^{-15}$ G [28]. We note that, in addition to the γ-ray observation, a cosmic ray is also applicable to estimate the strength of intergalactic magnetic fields, as previously reported as 10^{-17} G $\lesssim B \lesssim 3 \times 10^{-14}$ G [25], and $B_{1\ \mathrm{Mpc}} \lesssim 0.7 - 2.2 \times 10^{-10}$ G [33]. These estimations from γ-ray observations are remarkable since all of the estimated field strengths are in good agreement at about 10^{-20}–10^{-15} G, even though they are independent studies using different data and methods.

1.2 Origin of cosmic magnetic fields

It is under discussion how the magnetic fields in galaxies, galaxy clusters, and intergalactic region introduced above are generated. The scenarios about the origin and evolution of the cosmic magnetic fields are roughly classified into two classes.

- **Astrophysical origin:** Seed magnetic fields are generated around the epoch of formation of the first astrophysical objects, and the following activities or explosion spread them into the intergalactic region.
- **Primordial origin:** Tiny magnetic fields are generated in the early universe before recombination, and they provide the seed magnetic fields of the galactic magnetic fields and so on. These hypothetical magnetic fields in the early universe are called the "Primordial Magnetic Fields" (PMFs).

What is the difference between the magnetic fields generated by these scenarios? Or, which is more favorable for the observation data? To answer these questions, we argue the theoretical prediction of typical field strength from each scenario in this section, and current constraints on the PMFs obtained by some observations in the next section.

1.2.1 Astrophysical origin

One of the most widely accepted ways of generating magnetic fields is the so-called Biermann battery mechanism [34]. This mechanism is caused by the rotational turbulence in electromagnetic fluid, which induces the relative velocity between electrons and ions and the resultant rotational electric current produces magnetic fields. Biermann battery can produce magnetic fields even when the initial magnetic fields are absent, and it may support the astrophysical origin of the cosmic magnetic fields. The first magnetic field strength produced by the Biermann battery mechanism has been theoretically predicted as 10^{-21}–10^{-18} G around protogalaxies [35, 36], 10^{-17}–10^{-14} G around supernova remnants of first stars [37], 10^{-9} G in the central region of first stars [38], 10^{-19} G around first stars [39], and $B_{100\ \mathrm{kpc}} \sim 10^{-23}$ G around reionization sources [40]. Additionally, the subsequent amplification due to the turbulence [41] and injection into the intergalactic region throughout the outflow or astrophysical jet [42–46] have been discussed.

1.2.2 Primordial origin

On the other hand, there are many mechanisms proposed for generation of the magnetic fields in the early universe; e.g., the generation during the inflation epoch [47–51], the magnetogenesis due to the phase transition of the universe [52–54] and the other scenarios [55–58] (For recent review, see [59–61]). Regardless of the mechanisms, however, the predicted magnetic field strength is less than 10^{-30}–10^{-20} G. Therefore it is an open question whether or not such tiny PMFs can be amplified to the magnetic fields in galaxies or galaxy clusters, which have larger magnitudes than the PMFs by 10 orders [62]. Dynamo theory, which enables the magnetic fields to be amplified and sustained inside the rotating electromagnetic fluid, such as inside ordinary stars, is expected to solve this question [63, 64]. However, the efficiency of magnetic amplification with dynamo theory has a large uncertainty because it strongly depends on the physical state of astrophysical objects [65–67]. On the other hand, the observations of the intergalactic magnetic fields seem to be naturally explained by the PMFs, which is left behind in intergalactic space by the expansion of the universe. To confirm the evolutions of the PMFs, it is important to investigate their observational signatures with many observables. In this thesis, we focus on the observational constraints on the PMFs, especially with the primary CMB anisotropies, thermal Sunyaev-Zel'dovich effect, and 21-cm line observations.

1.3 Observational status on large-scale magnetic fields

The origin of the cosmic magnetic fields is one of the most mysterious problems in cosmic magnetism. As explained above in section 1.2, a lot of mechanisms are suggested to produce the first magnetic fields, and they have different scales and strength of generated magnetic fields. Therefore it is necessary to put a stringent observational constraint on the PMFs to access the origin of the cosmic magnetic fields. However, in the direct observational methods introduced at the beginning of this chapter, such signals from the PMFs are extremely smaller than the nearby astrophysical magnetic fields. While it is difficult to use them as probes of the PMFs, there are several approaches to constrain the large-scale cosmic magnetic fields. Figure 1.2 shows the theoretical and observational constraints on the (cosmologically-produced) large-scale magnetic fields, and the constraints are roughly divided into three parts.

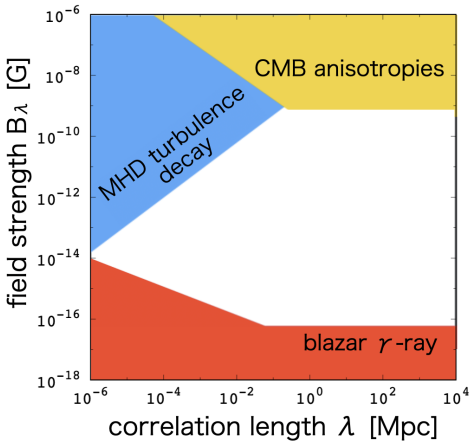

Figure 1.2: The current constraints on the large-scale cosmic magnetic fields. The color shaded regions are excluded by the MHD turbulence decay, observations of CMB anisotropies, and the γ-ray from blazars. This plot is referred in [68].

First, the γ-ray observations put the lower limit on the large-scale magnetic fields as explained in section 1.1. In addition, the MHD turbulence decay limits the magnetic field at small scales [69]. The magnetic field evolution in the early universe is calculated by solving MHD equations. The time-scale of the MHD turbulence depends on the correlation length of the magnetic fields. Consequently, the smaller the correlation length scale is, the more efficiently the magnetic fields decay. Therefore the upper limits on the magnetic fields are more stringent on smaller scales. Finally, various cosmological observations including the CMB anisotropies have put upper limits on the magnetic fields on larger scales than Mpc. Other observational probes for large-scale constraints are weak lensing [70], Lyman alpha [71,72], CMB spectral distortions [71,73], and the Sunyaev-Zel'dovich effect [74]. These different observations give constraints on the PMFs at different epochs. However, there are little observations at the Dark Ages, which are from the recombination around $z \sim 1100$ to the Cosmic Dawn around $z \sim 15 - 30$. Future radio observations, such as measurements of the redshifted 21-cm line, are expected to find cosmological signals from the Dark Ages. Therefore we revisit the effects on the CMB anisotropies and 21-cm line signal as cosmological observations theoretically and put constraints on the PMFs.

1.4 Purpose and structure of this thesis

In this thesis, we discuss the constraints on the PMFs from the current and future observations. Particularly, we focus on the small-scale CMB anisotropies induced by the PMFs [75], and the impact of the PMFs on the thermal history of baryon gas during the Dark Ages [76–78]. In Chapter 2, we introduce the principal assumptions and mathematical formalizations of the PMFs, and previous constraints of the PMFs. Next, we investigate the impacts of the PMFs on the primary CMB anisotropies on small scales, and show their constraint from Planck and SPT measurements in Chapter 3. Then, we dedicate Chapter 4 to the secondary CMB anisotropies induced by the PMFs due to the thermal Sunyaev-Zel'dovich effect, and discuss the possibility for current and future constraints. Finally, we propose a novel constraint on the PMFs from the 21-cm global signal, obtained by the EDGES experiment in Chapter 5, and we conclude in Chapter 6. We also describe special functions that are related to the treatment of the CMB temperature anisotropies in Appendix A. Throughout this thesis, we adopt the cosmological concordance flat ΛCDM model, and cosmological parameters are set as Hubble constant $H_0 = 67.8$ km/s/Mpc, density parameters for dark energy $\Omega_\Lambda = 0.692$, non-relativistic matter $\Omega_\mathrm{m} = 0.308$, and baryon $\Omega_\mathrm{b} = 0.048$, based on Planck 2015 results [79] unless explicitly mentioned otherwise.

Chapter 2

Basic Equations and the Primordial Magnetic Fields

2.1 MHD equations

In this section, we briefly review the basic Magnetohydrodynamics (MHD) equations. At first, Maxwell equations in CGS units are

$$\nabla \cdot \boldsymbol{E} = 4\pi\rho_e \ , \tag{2.1}$$

$$\nabla \times \boldsymbol{E} = -\frac{1}{c}\frac{\partial \boldsymbol{B}}{\partial t} \ , \tag{2.2}$$

$$\nabla \cdot \boldsymbol{B} = 0, \tag{2.3}$$

$$\nabla \times \boldsymbol{B} = \frac{4\pi}{c}\boldsymbol{j}_e + \frac{1}{c}\frac{\partial \boldsymbol{E}}{\partial t} \ , \tag{2.4}$$

with the electric field $\boldsymbol{E}$, the magnetic field $\boldsymbol{B}$, the electric charge density ρ_e, and the electric current density $\boldsymbol{j}_e$. From Eq. (2.2), the electric field is smaller than the magnetic field, as $|\boldsymbol{E}| \sim (v/c) \times |\boldsymbol{B}|$ with v being the bulk velocity of the fluid. Therefore, we may neglect the displacement current $c^{-1}\partial \boldsymbol{E}/\partial t$ in Eq. (2.4). This is called the MHD approximation. Because the conductivity of astrophysical plasma is actually very large, this is the case. Thus, Ampere's law (2.4) becomes

$$\nabla \times \boldsymbol{B} = \frac{4\pi}{c}\boldsymbol{j}_e \ . \tag{2.5}$$

We also assume that the electric current density is equivalent to the conduction current, which is determined by the Ohm's law as

$$\boldsymbol{j}_e = \sigma \left(\boldsymbol{E} + \frac{\boldsymbol{v}}{c} \times \boldsymbol{B} \right) \ , \tag{2.6}$$

where σ is the electric conductivity, and $\boldsymbol{v}$ is the velocity of the fluid. Using Eqs. (2.5) and (2.6), the induction equation (2.2) is represented by

$$\frac{\partial \boldsymbol{B}}{\partial t} - \nabla \times (\boldsymbol{v} \times \boldsymbol{B}) = -\nabla \times (\eta \nabla \times \boldsymbol{B}) \ , \tag{2.7}$$

where we denote the electrical resistivity η by

$$\eta \equiv \frac{c^2}{4\pi\sigma} \ . \tag{2.8}$$

From Eq. (2.5), the Lorentz force density is written as

$$\boldsymbol{f}_{\rm Lorentz} = \boldsymbol{j}_e \times \frac{\boldsymbol{B}}{c} = \frac{(\nabla \times \boldsymbol{B}) \times \boldsymbol{B}}{4\pi} \ . \tag{2.9}$$

Therefore, the continuity equation and the Euler equation are

$$\frac{\partial \rho}{\partial t} + \nabla \cdot (\rho \boldsymbol{v}) = 0 \ , \tag{2.10}$$

$$\rho \left[\frac{\partial \boldsymbol{v}}{\partial t} + (\boldsymbol{v} \cdot \nabla) \, \boldsymbol{v} \right] = -\rho \nabla \Phi - \nabla P + \boldsymbol{f}_{\rm Lorentz} \ . \tag{2.11}$$

Here, ρ is the mass density of the fluid, Φ is the gravitational potential, and P is the thermal pressure. The gravitational potential Φ satisfies the Poisson equation,

$$\Delta \Phi = 4\pi G \rho \ . \tag{2.12}$$

Besides, the thermal pressure P is given by the equation of state (EoS). For ideal gas through the adiabatic process, the EoS is simply with some constant C and the adiabatic index γ,

$$P = C \rho^\gamma \ . \tag{2.13}$$

Eqs (2.3), (2.7), and (2.10)-(2.13) are the complete set of MHD equations.

For cosmological applications, we define the co-moving spatial coordinates $\boldsymbol{x}_{\rm c}$ in an expanding universe. The co-moving coordinates $\boldsymbol{x}_{\rm c}$ is related to the static coordinates $\boldsymbol{x}$ as

$$\boldsymbol{x} = a(t) \boldsymbol{x}_{\rm c} \ , \tag{2.14}$$

with the cosmic scale factor $a(t)$, which corresponds to the size of the universe at time t. The time- and spatial-derivatives in the static frame can be related to those in the co-moving frame with the subscription "c" as

$$\frac{\partial}{\partial t} = \frac{\partial}{\partial t_{\rm c}} - \frac{\dot{a}}{a}\,\boldsymbol{x}_{\rm c}\cdot\nabla_{\rm c}\ , \qquad \nabla = \frac{1}{a}\,\nabla_{\rm c}\ . \tag{2.15}$$

Similarly, the co-moving velocity $\boldsymbol{v}_{\rm c}$, gravitational potential $\Phi_{\rm c}$, and magnetic fields $\boldsymbol{B}_{\rm c}$ are respectively

$$\boldsymbol{v} = \dot{a}\boldsymbol{x}_{\rm c} + \boldsymbol{v}_{\rm c}\ , \tag{2.16}$$

$$\Phi = \Phi_{\rm c} - \frac{1}{2}a\ddot{a}|\boldsymbol{x}_{\rm c}|^2\ . \tag{2.17}$$

With these co-moving variables Eqs. (2.14)-(2.17), the fluid equations (2.10) and (2.11) are transformed to

$$\frac{\partial\rho}{\partial t_{\rm c}} + 3\frac{\dot{a}}{a}\rho + \frac{1}{a}\nabla_{\rm c}\cdot(\rho\boldsymbol{v}_{\rm c}) = 0\ , \tag{2.18}$$

$$\rho\left[\frac{\partial\boldsymbol{v}_{\rm c}}{\partial t_{\rm c}} + \frac{\dot{a}}{a}\,\boldsymbol{v}_{\rm c} + \frac{1}{a}(\boldsymbol{v}_{\rm c}\cdot\nabla_{\rm c})\boldsymbol{v}_{\rm c}\right] = -\frac{1}{a}\,\rho\nabla_{\rm c}\Phi_{\rm c} - \frac{1}{a}\,\nabla_{\rm c}P + \boldsymbol{f}_{\rm Lorentz}\ . \tag{2.19}$$

In Chapter 3, we use this Euler equation (2.19).

From here, we omit the subscription "c", and use $\dot{A}$ for the time derivative of A for simplicity. Then, we introduce the perturbed density field as

$$\delta(\boldsymbol{x},t) \equiv \frac{\rho(\boldsymbol{x},t) - \bar{\rho}(t)}{\bar{\rho}(t)}\ , \tag{2.20}$$

where $\bar{\rho}(t)$ is the spatially homogeneous background density field. We rewrite the continuity equation (2.18), the Euler equation (2.19), and the Poisson equation (2.12) with the overdensity δ. As a result, the perturbed equations are

$$\dot{\delta} + \frac{1}{a}\,\nabla\cdot[(1+\delta)\boldsymbol{v}] = 0\ , \tag{2.21}$$

$$\dot{\boldsymbol{v}} + \frac{\dot{a}}{a}\,\boldsymbol{v} + \frac{1}{a}(\boldsymbol{v}\cdot\nabla)\boldsymbol{v} = -\frac{1}{a}\,\nabla\Phi - \frac{1}{a\bar{\rho}(1+\delta)}\,\nabla_{\rm c}P + \frac{\boldsymbol{f}_{\rm Lorentz}}{\bar{\rho}(1+\delta)}\ , \tag{2.22}$$

$$\Delta\Phi = 4\pi G a^2\bar{\rho}\delta\ . \tag{2.23}$$

At the first order of the density perturbation δ, we can obtain the evolutionary equation for δ from Eqs. (2.21)-(2.23) as

$$\ddot{\delta} + 2\frac{\dot{a}}{a}\dot{\delta} - 4\pi G\bar{\rho}\delta = \frac{\nabla P}{\bar{\rho}a^2} - \frac{1}{\bar{\rho}a}\nabla\cdot\boldsymbol{f}_{\rm Lorentz}\ . \tag{2.24}$$

By neglecting the thermal pressure, we can obtain the evolutionary equations for cold dark matter (4.1) and baryon density fluctuations (4.2) in Chapter 4.

2.2 Statistical properties of the PMFs

In this section, we argue the time evolution and the spatial distribution of the PMFs. First, we mention about the time evolution of the PMFs. Adiabatic evolution of the PMFs as $\boldsymbol{B}(\boldsymbol{x},t) \propto 1/a^2(t)$ is a good approximation in the high-redshift universe. In Chapter 5, we give a more realistic estimate of the PMF evolution.

Then, we discuss the statistical property of the PMF spatial distribution. Throughout this paper, we assume the PMFs as Gaussian random fields. Therefore the statistical property of the PMFs is completely determined by the two-point correlation function. Additionally, we assume that the spatial distribution of the PMFs are statistically homogeneous and isotropic. Thus, the two-point correlation function of the PMFs in wave-number space can be written with the form of power spectrum $P_B(k)$ with $k = |\boldsymbol{k}|$ as [80, 81]

$$\langle B_i(\boldsymbol{k})B_j^*(\boldsymbol{k}')\rangle = \delta_{\rm D}(\boldsymbol{k}-\boldsymbol{k}')(\delta_{ij} - \hat{k}_i\hat{k}_j)P_B(k)\ . \tag{2.25}$$

Here $\hat{k}_i$ is the normalized wave number vector, $\delta_{\rm D}$ is the Dirac's delta function, and $B_i(\boldsymbol{k})$ is the PMF in Fourier space as defined by $\boldsymbol{B}(\boldsymbol{k}) = \int d^3x\ \mathrm{e}^{i\boldsymbol{k}\cdot\boldsymbol{x}}\boldsymbol{B}(\boldsymbol{x})$. Here we neglect the helical component of the PMFs.

For simplicity, we assume that the power spectrum of the PMFs has a single power-law shape in k-space as

$$P_B(k) = A_B k^{n_B} \quad (\text{for}\ \ k < k_{\rm cut})\ . \tag{2.26}$$

Here A_B is the amplitude of the PMF power spectra and n_B gives the scale dependence. In the context of the constraints on the PMFs, the smoothed PMF strength on $\lambda_n = 1$ Mpc scale, $B_{\rm 1Mpc}$ is often introduced. This smoothed PMF strength is related to the amplitude of the PMF power

spectrum as

$$B_{1\mathrm{Mpc}}^2 = \int \frac{d^3k}{(2\pi)^3}\, \mathrm{e}^{-k^2\lambda_n^2} P_B(k)$$
$$= \frac{A_B}{4\pi^2 \lambda_n^{n_B+3}}\, \Gamma\left(\frac{n_B+3}{2}\right). \tag{2.27}$$

We note that we choose a Gaussian filter as the smoothing window function. [1] Also, in derivation of the second line in equation (2.27), we have used the definition of the Gamma function, $\Gamma(x) \equiv \int_0^\infty e^{-t} t^{x-1} dt$. In this thesis, we do not specify any generation mechanisms of the PMFs. Instead of that, we use the model parameter for the PMFs as $B_{1\mathrm{Mpc}}$ and n_B to cover a wide range of PMF models. However, some previous observational and theoretical works discuss the PMFs with different smoothing scales of the PMFs from $\lambda_n = 1$ Mpc. In comparison with such works, we can relate the PMF strength smoothed on any scale λ as

$$B_\lambda = B_{1\mathrm{Mpc}} \left(\frac{1\mathrm{Mpc}}{\lambda}\right)^{(n_B+3)/2}. \tag{2.28}$$

Equation (2.28) implies that the case of $n_B = -3.0$ corresponds to the scale-invariant PMFs. Additionally we adopt $n_B > -3.0$ throughout this thesis to avoid the infrared divergence of the PMFs.

On the other hand, in the ultraviolet regime, the PMFs have the cut-off scale due to the MHD effect in the early universe. According to the previous studies [86, 87], the radiative diffusion before the recombination epoch damps the PMFs on small scales. The damping scale increases as the universe evolves. Therefore, we assume that the power spectrum has the sharp cut-off on the damping scale at the recombination epoch,

$$P_B(k) = 0 \qquad (\text{for} \quad k \geq k_{\mathrm{cut}})\ . \tag{2.29}$$

According to Ref. [88], the cut-off scale at the recombination epoch is given

[1] We have used this definition of the smoothed amplitude of the PMFs from [82]. Although this definition is slightly different from some other works (such as [83, 84]), the value of B_λ is almost unchanged among different definitions. There are some different definitions of the power spectrum of PMFs, for example, see Eq. (3.8) in [85]. We follow the above one with which most previous studies have worked.

by

$$\left(\frac{k_{\rm cut,rec}}{k_n}\right)^{-2} = \frac{V_{\rm A}^2}{\sigma_{\rm T}}\int_0^{t_{\rm rec}} \frac{dt}{a^2(t)n_e(t)} \\ \simeq \left[1.32\times10^{-3}\left(\frac{B_n}{1\ {\rm nG}}\right)^2\left(\frac{\Omega_{\rm b}h^2}{0.02}\right)^{-1}\left(\frac{\Omega_{\rm m}h^2}{0.15}\right)^{1/2}\right]^{\frac{2}{(n_B+5)}}, \tag{2.30}$$

where $\sigma_{\rm T}$ and $n_e(t)$ are the cross section for Thomson scattering and the electron number density, respectively. Here, the Alfvén velocity, $V_{\rm A}$, is defined as

$$V_{\rm A} \equiv \frac{B_{\lambda_{\rm cut}}(t_{\rm rec})}{\sqrt{4\pi\rho_\gamma(t_{\rm rec})}}\,, \tag{2.31}$$

with $\lambda_{\rm cut} = 2\pi/k_{\rm cut}$. From Eq. (2.30), we can find that the larger B_n and n_B give the shorter cut-off length.

Chapter 3

Impact on CMB primary anisotropies

In this chapter, we briefly review the CMB, which is considered to be the footprint of Big Bang theory, and give an updated constraint on the PMFs from CMB anisotropies.

3.1 The Big Bang theory and discovery of the CMB

Currently, the Big Bang theory as the cosmological model is widely accepted, and this describes that the earliest observable universe is the high density and temperature state. Friedmann and Lemaître have independently shown that the universe might expand as the solution of the Einstein equation [89,90]. So far, there are three strong observational pieces of evidence of the Big Bang theory.

In 1929, Edwin Hubble reported that the line-of-sight velocity of galaxies (called "nebulae" at that time) is proportional to the distance to them [91]. He estimates the distance to the galaxies from the apparent brightness and their velocity from the spectral energy distribution including the Doppler effect. [1] Here we define the redshift z as

$$z = \frac{\lambda_{\rm o} - \lambda_{\rm e}}{\lambda_{\rm e}} \,, \tag{3.1}$$

with the wavelength of the emitted photon from the galaxy in the rest frame

[1] Vesto Slipher had already measured the Doppler shift of the spiral galaxies in 1912 [92]. However, Hubble pointed for the first time the relation between the corresponding velocities of measured galaxies and the distances to them.

$\lambda_{\rm e}$ and the observed wavelength $\lambda_{\rm o}$. Together with the speed of light c and the recessional velocity of the galaxy v, Doppler's law suggests [2]

$$v = cz \ . \tag{3.3}$$

On the other hand, the distance to the galaxy is required to be calculated, in addition to the recessional velocity v. Hubble has used Cepheid variables in galaxies as a "standard ruler", and discovered that the recessional velocities of galaxies are proportional to the distances to them r as

$$v = Hr \ , \tag{3.4}$$

with the Hubble constant H. This relation is known as "Hubble-Lemaître law". Expanding spacetime, which is the most basic idea of the Big Bang theory, gives us a straightforward explanation of the relation (3.4).

What we can use as standard rulers are not only Cepheid variables, but also annual parallax, stars in the main sequence, Tully-Fisher relation for the spiral galaxies, Fundamental Plane for the elliptical galaxies, and Type Ia supernovae (SNe Ia). In particular, SNe Ia are the brightest standard candle among them, and their observations have told us the fact that the Hubble constant H is not a constant; i.e., dark energy exists. To uncover the nature of dark energy is the physicists' biggest dream.

In 1948, Alpher, Bethe, and Gamow reported that the Big Bang universe gets colder as it expands, and then light chemical elements such as hydrogen and helium are synthesized [93]. Because their prediction of abundance is in good agreement with the fraction of elements in the present universe, this supports the validity of the Big Bang cosmology. This nucleosynthesis model is also known as $\alpha\beta\gamma$ theory named after the authors. Afterward, this nucleosynthesis model is revisited by Hayashi, and the abundance of the light elements is explained more precisely [94].

In 1951, Alpher and Herman suggested that the Universe continues to get colder even after the nucleosynthesis, and the atomic nuclei produced by the Big Bang nucleosynthesis capture the free electrons, leading to the most amount of hydrogen and helium becoming neutral [95]. Therefore this epoch is called the cosmic "recombination". Before the recombination, the

[2] Here we assume that the galactic motion is non-relativistic. Consideration for the relativistic Doppler effect changes the relation between the redshifts and the recessional velocities of the galaxies as

$$1 + z = \sqrt{\frac{1 + v/c}{1 - v/c}} \, . \tag{3.2}$$

Taylor-series expansion of this equation with $v/c \ll 1$ leads to Eq. (3.3).

photons are strongly coupled to the free electrons via Thomson scattering. After that, the photons decouple from baryons and they start to travel a long distance with little scattering. Alpher and Herman calculated these decoupled photons would be observed as isotropic radiation with about 28 K at the present epoch. More recent precise calculation of the thermal history revealed that the recombination occurs around 380 thousand years after the Big Bang, and this isotropic background radiation is around 2.7 K. As described below, the discovery of the cosmic microwave background radiation is considered as the evidence of big bang cosmology together with the confirmation of light element abundance produced by Big Bang nucleosynthesis.

The CMB has the almost perfect black body spectrum, which was discovered by Arno Penzias and Robert Woodrow Wilson in 1964 [96]. Later, a lot of the CMB measurements were provided, including Cosmic Background Explorer (COBE) satellite and Wilkinson Microwave Anisotropy Probe (WMAP) of National Aeronautics and Space Administration (NASA), and Planck of the European Space Agency (ESA). Their measurements of the CMB conclude that its temperature is almost isotropic. According to the COBE results [97], the mean temperature is

$$T_0 \simeq 2.72548\mathrm{K} \ . \tag{3.5}$$

Currently, the CMB temperature map has small anisotropies as shown in Fig. 3.1.

3.2 CMB temperature anisotropy

In this section, we discuss how to treat observables of the CMB temperature anisotropy. Observed CMB temperature anisotropy has roughly two components; the primary anisotropy, which is created before the recombination, and the secondary anisotropy, which is induced after the recombination. The primary anisotropy is caused by the metric perturbations, which is originated in the inflation mechanism. The secondary anisotropies include the dipole component from the Milky Way's motion, integrated Sachs-Wolfe effect, Sunyaev-Zel'dovich effect, which is discussed in the next chapter, and so on. Because the relevant epochs and the spatial scales differ from these effects, these components are roughly distinguished by decomposing CMB anisotropies with different angular scales.

Here, we write the observed temperature $T(\boldsymbol{n})$ of the CMB photon coming from a direction vector $\boldsymbol{n}$. In general, $T(\boldsymbol{n})$ is different from the averaged

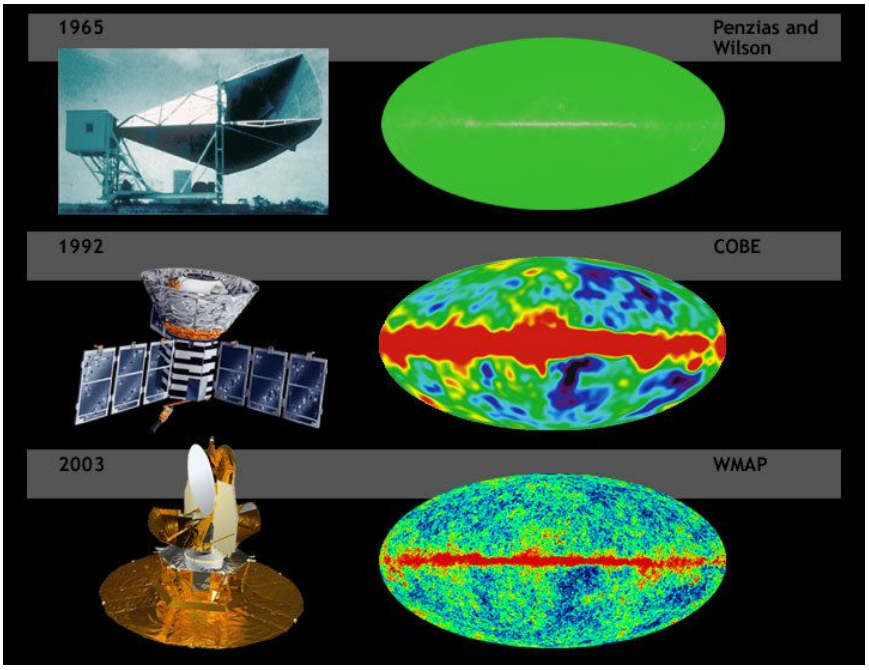

Figure 3.1: (top) the all-sky CMB temperature map measured by Penzias and Wilson. Galactic foreground radiation can be observed at the center of the image. (center) the CMB map measured by COBE satellite. For the first time, dipole anisotropy due to the Galactic motion was observed. (bottom) the CMB map measured by WMAP satellite. The small-scale anisotropies of the CMB temperature were precisely measured, and then WMAP contributed to the precise cosmology. (This figure was brought by NASA/WMAP Science Team.)

CMB temperature T_0 in Eq. (3.5). We define this differential value of temperatures as

$$\delta T(\boldsymbol{n}) \equiv T(\boldsymbol{n}) - T_0 \tag{3.6}$$

It is convenient to expand the fraction of temperature difference to the mean temperature, with the spherical harmonics $Y_{lm}(\boldsymbol{n})$ as

$$\frac{\delta T(\boldsymbol{n})}{T_0} = \sum_{l=1}^{\infty} \sum_{m=-l}^{m=l} a_{lm} Y_{lm}(\boldsymbol{n}) \ . \tag{3.7}$$

Spherical harmonics is a complete set of functions that is a orthonormal basis on the surface of a sphere (For details, see Reference [98] and Appendix A.2).

From the positivity of temperature and property of the spherical harmonics $Y^*_{l,m} = (-1)^{-m} Y_{l,-m}$, coefficients a_{lm} satisfy the following relation,

$$a^*_{l,m} = (-1)^m a_{l,-m}. \tag{3.8}$$

Since the spherical harmonics form a orhonormalized functions, We rewrite a_{lm} with the integral form as

$$a_{lm} = \int d\boldsymbol{n} \frac{\delta T(\boldsymbol{n})}{T_0} Y^*_{lm}(\boldsymbol{n}) \ . \tag{3.9}$$

Here integration is for the unit sphere surface. Using this equation, we can obtain the coefficients a_{lm} from measured values $\delta T_0(\boldsymbol{n})$. Then we consider the physical meaning of the coefficients a_{lm}. From the asymptotic expression of the spherical harmonics (A.36), which is valid for $l \gg 1$, multipole l roughly corresponds to an angular scale $\theta \sim \pi/l$, and a_{lm} represent the temperature anisotropy smoothed on the corresponding angular scale. The largest contribution to the CMB temperature anisotropies is $l = 1$, which corresponds to the dipole moment. This component arises from the proper motion of the earth at the CMB rest frame. In the cosmological analysis, we usually neglect this dipole anisotropy due to this Doppler effect for the proper motion. Unless the isotropy of the universe is broken, coefficients a_{lm} are not correlated for different l and m. This idea is applied to an imaginary set of universe"s", which consists of many independent universes including our universe. We assume that the ensemble average for such a set of universes satisfies the following property.

$$\langle a_{lm} a^*_{l'm'} \rangle = C_l \delta_{ll'} \delta_{mm'} \ , \tag{3.10}$$

where proportional constant C_l depends on only total angular momentum l, and does not on m. Also, if the initial density perturbations completely follow a Gaussian distribution, a higher-order correlation function (3-point and more) cannot be produced. Therefore, under these assumptions, the coefficients C_l completely determine the property of the CMB temperature anisotropy. We can access the information of only one universe, and we can obtain one value of a_{lm} for one combination (l, m). Therefore, in principle, we cannot confirm the statistical relation (3.10) directly from the observational data. However, for large multipole ℓ, we can confirm whether or not many a_{lm} for the subsamples satisfy the Eq. (3.10). We have no evidence for such inconsistency from the current CMB observations.

Under the assumption (3.10), one can sum the variances of a_{lm} over m to estimate C_l as

$$C_l = \frac{1}{2l+1} \sum_{m=-l}^{m=l} |a_{lm}|^2 \tag{3.11}$$

We note that C_l follows χ^2_{2l+1} distribution because of the definition of C_l in Eq. (3.11) and assumption that a_{lm} obey the Gaussian distribution with the mean value 0. Therefore, the variance of C_l is $(\delta C_l)^2 = 2C_l^2/(2l+1)$, and the statistical uncertainty of C_l is order of $1/\sqrt{l+1/2}$. This statistical uncertainty is inevitable because we can obtain one all-sky CMB temperature map, and it is called the "cosmic variance". Thus the theoretical prediction of C_l values may differ from the measurements within the fraction of $1/\sqrt{l+1/2}$. We note that the cosmic variance affects the precision to determine the cosmological parameters from the measurement of the matter power spectra, as well as from those of the CMB anisotropies.

Coefficients C_l determine the two-point correlation function of the CMB temperatures $\langle \delta T(\boldsymbol{n}_1)\delta T(\boldsymbol{n}_2)\rangle$. If the temperature fluctuations follows the Gaussian distribution perfectly, the property of their spatial distribution can be described by the two-point correlation function. Using Eq. (3.7), we can write down the two-point correlation function as

$$\begin{aligned}\langle \delta T(\boldsymbol{n}_1)\delta T(\boldsymbol{n}_2)\rangle &= T_0^2 \sum_l C_l \sum_m Y_{lm}(\boldsymbol{n}_1) Y^*_{lm}(\boldsymbol{n}_2) \\ &= T_0^2 \sum_l \frac{2l+1}{4\pi} C_l P_l(\boldsymbol{n}_1 \cdot \boldsymbol{n}_2) \ , \end{aligned} \tag{3.12}$$

where P_l is Legendre polynomial (see Appendix A.2). We used Eqs. (A.19) and (A.34). From Eq. (3.12) We can also find the temperature variance as

$$\langle \delta T^2(\boldsymbol{n})\rangle = T_0^2 \sum_l \frac{2l+1}{4\pi} C_l \sim T_0^2 \int d(\log l) \frac{l(l+1)}{2\pi} C_l \ . \tag{3.13}$$

Note that we have assumed the large l in the second approximation. We have derived the quantity

$$\mathcal{D}_l \equiv T_0^2 \frac{l(l+1)}{2\pi} C_l \ , \tag{3.14}$$

which represents the squared amplitude of the differential temperature with varying a multipole $d(\log l)$. the CMB temperature angular power spectrum is often plotted with $\mathcal{D}_l$.

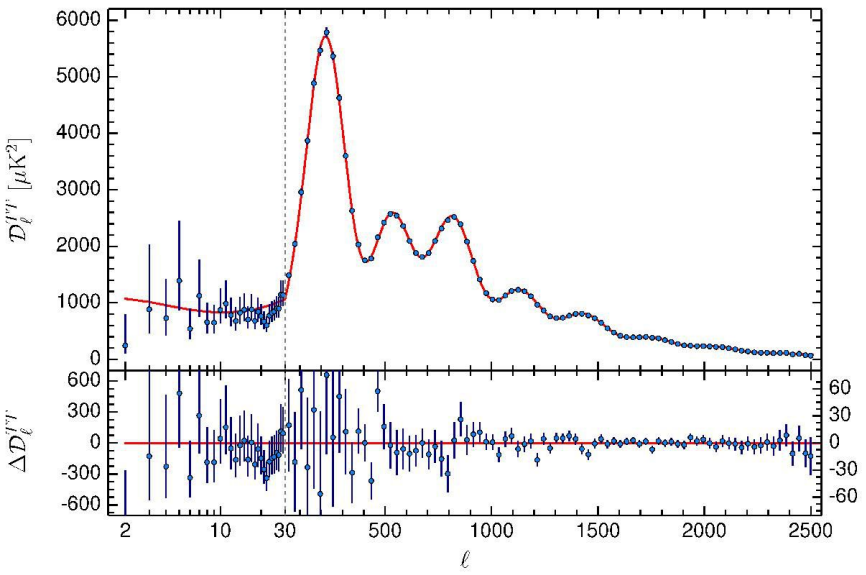

Figure 3.2: The CMB temperature anisotropies measured by *Planck* satellite. The horizontal axis shows the multipole l, and the vertical axis shows the anisotropy $\mathcal{D}_l$, defined by Eq. (3.14). In the horizontal axis, plots are logarithmically for $2 \leq l \leq 30$ and linearly for $l \geq 30$. The Planck observational data are plotted with the blue points with error bars, and the theoretical curve obtained by regression analysis is shown with the red solid line. The error bars represent one standard deviation of uncertainty, $\pm 1\sigma$. In the theoretical calculation, the concordance ΛCDM cosmological model is adapted with the best-fitted cosmological parameters. obtained by the Markov chain Monte Carlo analysis. The bottom panel shows the deviation of the observational data from the theoretical values. (The figure is provided by ESA/*Planck* collaboration [79].)

Figure 3.2 shows the CMB temperature anisotropies measured by *Planck* satellite. This plotting has the following characteristics of the primary CMB anisotropies:
(1) The typical amplitude of the CMB temperature anisotropy is $\delta T/T_0 \sim 10^{-4}$–$10^{-5}$.
(2) The angular power spectrum has oscillations, whose peaks are at $l \sim 200, 500, 800, 1100, 1400$.
(3) The anisotropy decreases with increasing l for $l \gtrsim 500$.
(4) The oscillations rapidly decay for $l \gtrsim 1000$.

These signatures can be explained by adiabatic scalar-type curvature perturbations in ΛCDM model and the flat primordial curvature spectrum with the amplitude of 10^{-5}. The oscillation in the angular power spectrum is caused by the acoustic wave in the baryon-photon plasma at the recombination epoch [99, 100]. [3] Finally, this acoustic oscillation starts to damp around $l \gtrsim 1000$, and this is called the "Silk damping" [101]. Although the CMB photons are coupling with baryons before the recombination epoch, each photon can travel a finite distance as a random walk with scattering repeatedly. As a result, the density perturbations below the random walk distance should be smoothed out due to the diffusion effect. Therefore the amplitude of the angular power spectrum starts to decay for $l \gtrsim 1000$.

3.3 CMB polarization

In addition to the CMB temperature anisotropies, its polarization fields are important in cosmology. The CMB photons are polarized from the quadrupole temperature anisotropies because of the existence of the Thomson scattering, as shown in Fig. 3.3.

If neglecting the circular polarization, two variables are needed to represent the polarization of a propagating photon. In such a case, the Stokes parameters, Q and U are often used. While the temperature anisotropy is a rotational invariant value, Q and U change under the rotational transformation of the coordinates on a spherical surface, and thus they are spin-2 quantities. Therefore, instead of Eq. (3.7), we can expand the Stokes Q and

[3] This oscillating feature is called the "acoustic oscillation", and important to constrain the cosmological models. The first mentioning of this acoustic oscillation is in [99], and this paper also predicts the Sunyaev-Zel'dovich effect (SZ effect) for the first time. (We treat the SZ effect in Chapter 4.) It is surprising that two important effects on the CMB anisotropies, i.e., the acoustic oscillation and the SZ effect, were predicted in a single paper in 1970, which is only 5 years later than the discovery of the CMB! (Of course, it was not clear that the CMB temperature anisotropy can be observed or not.)

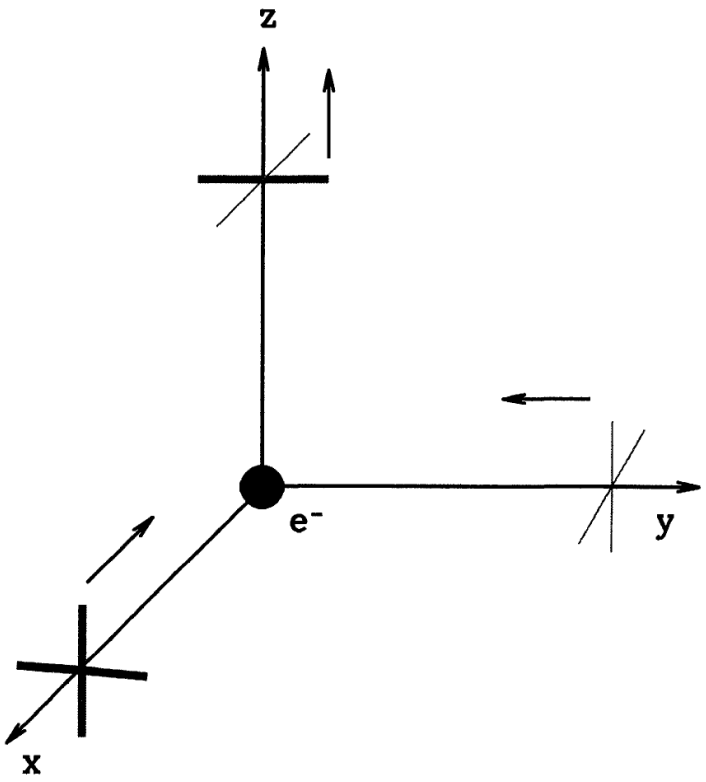

Figure 3.3: An outgoing polarized photon along z-axis, which is scattered with an electron at the origin. The temperature difference between the incoming photon along x-axis and one along y-axis can produce polarization after the scattering. (This figure is reprinted from Ref. [102].)

U with the spin-weighted spherical harmonics ${}_{\pm2}Y_{lm}$ as

$$Q(\boldsymbol{n}) \pm iU(\boldsymbol{n}) = \sum_l \sum_m a_{\pm2,lm}\ {}_{\pm2}Y_{lm}(\boldsymbol{n}) \ . \tag{3.15}$$

Instead of $a_{\pm2,lm}$, it is convenient to define different two quantities: E_{lm} and B_{lm} as

$$E_{lm} \equiv -\frac{(a_{2,lm} + a_{-2,lm})}{2} \ , \tag{3.16}$$

$$B_{lm} \equiv \frac{i(a_{2,lm} - a_{-2,lm})}{2} \ . \tag{3.17}$$

This enables to decompose the polarization fields into the parity-even E-mode and the parity-odd B-mode.

Now, we introduce the useful points for this E-B decomposition. As described at the beginning of section 3.2, temperature anisotropies including the quadrupole moments arise from the metric perturbations. In the cosmological perturbation theory, the metric perturbations are decomposed into the scalar-, vector-, and tensor-types with respect to the rotational symmetry. The temperature anisotropies from the tensor-type perturbations (the gravitational wave) can create the B-mode polarization while those from the scalar-type perturbations cannot because of the above nature of parity. Therefore, detecting the CMB B-mode polarization is a useful tool to search for the primordial gravitational wave. Note that the vector-type perturbations are not discussed very much because they must decay unless there is some anisotropic stress tensor to source them. In the following sections, we discuss the velocity perturbations and the vector-type CMB anisotropies induced by the anisotropic stress tensor of the PMFs.

3.4 CMB anisotropies created by the PMFs

As mentioned in section 1.3, the CMB observations put upper limits on the PMF strength. One of the most important works is carried out from the Planck 2015 observation [112]. Recently, Zucca et al. [103] have improved the PMF constraints from the combined data of Planck and SPT B-mode polarization. Because the anisotropic stress tensor of the PMFs induces all types of metric perturbations, the measurement of the B-mode polarization is a powerful probe for the PMFs, as well as for the primordial gravitational wave. Although the stringent limit on the PMFs have

already obtained from the B-mode observations, we show that the small-scale temperature anisotropies can also give a powerful constraint on the PMFs. While the primary CMB anisotropy, which is caused by the inflationary metric perturbation, experiences the so-called Silk damping around multipoles $\ell \sim 2000$, the PMFs can create CMB anisotropies much smaller than the Silk scale, not only for B-mode but also for T-mode and E-mode. SPT has recently detected TT, EE, and TE power spectrum for a wide multipole range, $50 < \ell < 8000$ [104]. This precise measurement of small-scale CMB fluctuations can give us a tighter constraint on the PMFs, especially with blue-tilted power spectra. We put the first PMF constraint with both temperature and polarization from Planck and SPT. We introduce the CMB angular power spectra sourced by the stress-energy tensor of the PMFs in this section.

3.4.1 Formalisms of the PMFs

Since the primordial plasma in the Universe has high conductivity, the ideal MHD is valid to provide the evolution of the PMFs. Besides, the back-reaction from the primordial plasma motion on the PMFs is described as a higher-order effect in the linear cosmological perturbation theory, and we can neglect them in this work. Therefore, the PMF evolution can be described adiabatically. Following the cosmological expansion, the PMFs evolve as $\boldsymbol{B}(\boldsymbol{x}, t) \propto \boldsymbol{B}_0(\boldsymbol{x})/a^2(t)$, where $a(t)$ is the scale factor at time t, which is normalized in $a(t_0) = 1$ at the present epoch, t_0.

In this study, we do not focus on any specific PMF generation mechanism, but calculate the CMB anisotropies with three free parameters, $B_{1\mathrm{Mpc}}, n_B$, and η_B for characterizing our PMF model. Here, η_B is the conformal time at which the PMFs are generated, and this determines the initial condition of the PMF induced perturbations. The effect on the CMB anisotropies of varying η_B is discussed later.

Under the above assumptions, the energy-momentum tensor of the PMFs in Fourier space, ${T_B}^{\mu}{}_{\nu}$, is given by

$$
\begin{aligned}
{T_B}^0{}_0(\boldsymbol{k}, t) &= -\frac{1}{8\pi a^4(t)} \int \frac{d^3k'}{(2\pi)^3} B^a(\boldsymbol{k}') B_a(\boldsymbol{k} - \boldsymbol{k}') \equiv -\rho_\gamma \Delta_B \ , && (3.18)\\
{T_B}^0{}_i(\boldsymbol{k}, t) &= 0 \ , && (3.19)\\
{T_B}^i{}_j(\boldsymbol{k}, t) &= \frac{1}{4\pi a^4(t)} \int \frac{d^3k'}{(2\pi)^3} \left[\frac{1}{2} B^a(\boldsymbol{k}') B_a(\boldsymbol{k} - \boldsymbol{k}') \delta^i{}_j - B^i(\boldsymbol{k}') B_j(\boldsymbol{k} - \boldsymbol{k}') \right] \\
&\equiv p_\gamma (\Delta_B \delta^i{}_j - \Pi_B{}^i{}_j) \ . && (3.20)
\end{aligned}
$$

Here we have defined the dimensionless parameters Δ_B and $\Pi_B{}^i{}_j$ with the energy density ρ_γ and pressure p_γ of CMB photons. The dimensionless magnetic energy density Δ_B and the anisotropic stress $\Pi_B{}^i{}_j$ source the cosmological perturbations via Einstein-Boltzmann equations. The scalar-vector-tensor decomposition is powerful to analyze the evaluations of perturbation quantities at the linear order in cosmological perturbation theory. Since Δ_B is a scalar quantity, it can source only the scalar-type perturbations. On the other hand, the PMF anisotropic stress tensor $\Pi_B{}^i{}_j$ can be decomposed into the scalar $\Pi_B^{(0)}$, vector $\Pi_B^{(\pm1)}$, and tensor part $\Pi_B^{(\pm2)}$ (for detailed discussion, see, e.g., Refs. [88, 105]) and, then, it can source all types of perturbations.

Besides the metric perturbation induced by the energy-momentum tensor of the PMFs via the Einstein equation, the PMFs can generate perturbations through the Lorentz force on the baryon plasma. The Lorentz force L_i can be related to the magnetic energy density and anisotropic stress. Thus the Lorentz force term is also decomposed into the scalar-type $L^{(\mathrm{S})} = 2\Pi_B^{(0)}/9 - \Delta_B/3$ with the scalar-type values, Δ_B and $\Pi_B^{(0)}$, and the vector-type $L_i^{(\mathrm{V})} = ik(\Pi_B^{(+1)}\hat{k}_{(i}\mathrm{e}^+_{j)} + \Pi_B^{(-1)}\hat{k}_{(i}\mathrm{e}^-_{j)})\hat{k}_j$ with the vector-type value $\Pi_B^{(\pm1)}$. Here, $\mathbf{e}^\pm \equiv -i/\sqrt{2}(\mathbf{e}^1 \pm i\mathbf{e}^2)$ are the helicity basis with complex orthonormal bases, $\mathbf{e}^1$ and $\mathbf{e}^2$, which are perpendicular to $\boldsymbol{k}$ [88, 105].

3.4.2 Impact of the PMFs on the CMB spectra

To study the evolution of the cosmological perturbations, we solve the Boltzmann and Einstein equations with some initial conditions. In practice, we set the initial condition on the super-horizon scale and well after the neutrino decoupling. However, it is known that neutrinos provide different effects on the perturbations induced by the PMFs before and after the neutrino decoupling. After the neutrino decoupling, neutrinos freely stream, and then they can create the non-zero anisotropic stress to compensate for that of the PMFs. On the other hand, before the neutrino decoupling, neutrinos tightly couple with the photon-baryon fluid. As a result, neutrinos have no anisotropic stress and cannot compensate for that of PMFs. This difference between before and after the neutrino decoupling brings two modes with different initial conditions; passive and compensated modes.

The passive mode arises due to the anisotropic stress of the PMFs before the neutrino decoupling. The non-zero contribution of the PMF anisotropic stress on the metric evolution grows the passive mode logarithmically soon after the generation of the PMFs. When neutrinos decouple from the photon-baryon fluid, the anisotropic stress of the PMFs is compensated by

free-streaming neutrinos, as mentioned before. Although the perturbation growth halts after that, the induced perturbation can exist as a constant perturbation, similar to an inflationary adiabatic perturbation. The amplitude of this mode depends on $\ln(\eta_\nu/\eta_B)$, with the conformal time of the neutrino decoupling η_ν and that of the PMF generation η_B [105]. The vector-type perturbation for the passive mode after the neutrino decoupling decays in the same way as the inflationary adiabatic vector-type perturbation does. Therefore the CMB anisotropies arise from the scalar and tensor-type perturbation for the passive mode. The angular power spectrum of the CMB anisotropies due to the passive mode are proportional to $\langle \Pi_B^{(0)*} \Pi_B^{(0)} \rangle$ for the scalar-type contribution and $\langle \Pi_B^{(\pm 2)*} \Pi_B^{(\pm 2)} \rangle$ for the tensor-type contribution.

On the other hand, the perturbation induced by the PMFs after the neutrino decoupling is called the compensated mode. After the neutrino decoupling, the PMF anisotropic stress is canceled by the neutrino free streaming motion. There is no contribution of the PMF anisotropic stress to the metric perturbation. As a result, the metric perturbation for the compensated mode is not generated at the leading order on super-horizon scales. In this respect, the compensated mode is similar to the isocurvature perturbation. With this initial condition, the PMFs induce the perturbation sourced by the stress-energy tensor of the PMFs including the Lorentz force on sub-horizon scales. The compensated mode is important on small-scale CMB anisotropies. Although some fraction of the compensated mode perturbation is erased by the Silk damping effect, the CMB anisotropies on smaller scales than the Silk scale can be created by the compensated mode. This is because the PMFs can survive and continue to source the CMB anisotropies even below the Silk damping scale. We discuss the behavior of such small-scale CMB anisotropies in section 3.5. In the compensated mode, the scalar, vector, and tensor types can generate the CMB anisotropies. In the scalar type, the amplitude of the CMB angular power spectrum is proportional to $\langle \Delta_B^* \Delta_B \rangle$, $\langle \Pi_B^{(0)*} \Pi_B^{(0)} \rangle$, and $\langle \Delta_B^* \Pi_B^{(0)} \rangle$. In the vector and tensor types, $\langle \Pi_B^{(\pm 1)*} \Pi_B^{(\pm 1)} \rangle$ and $\langle \Pi_B^{(\pm 2)*} \Pi_B^{(\pm 2)} \rangle$ appear on the CMB angular power spectrum, respectively.

Figure 3.4 shows that the CMB temperature-temperature (TT) auto-power spectra induced by the PMFs for three dominant contributions, namely, the passive scalar mode, the compensated vector mode, and the passive tensor mode. The PMF contributions to the CMB angular power spectra with $B_{1\mathrm{Mpc}} = 4.0$ nG, $n_B = -2.5$ are plotted in the left panel, and those with $B_{1\mathrm{Mpc}} = 3.0$ nG, $n_B = -1.5$ are shown in the right panel. It is clear that the passive tensor mode has a significant contribution on large-scale as $\ell \lesssim 100$

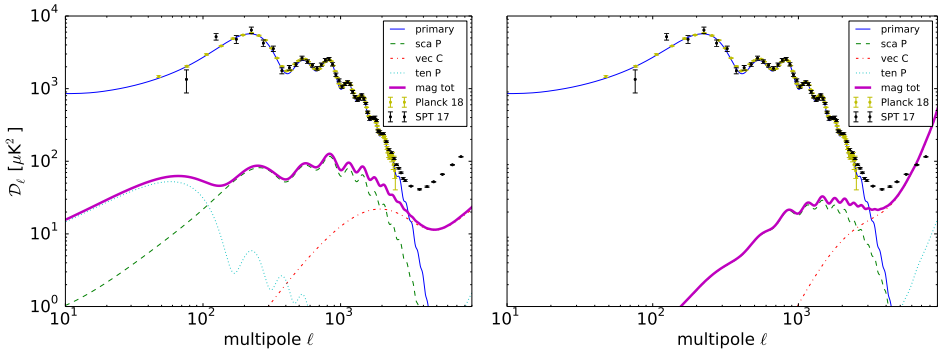

Figure 3.4: The top thin solid line is the primary CMB temperature angular power spectrum, which is due to the adiabatic perturbation created by the inflation mechanism. We show the magnetically induced power spectra for three magnetic modes, the passive scalar mode (sca P) with the dashed line, the compensated vector mode (vec C) with the dash-dotted line, and the passive tensor mode (ten P) with the dotted line. In the plots, we take the PMF parameters as $B_{1\mathrm{Mpc}} = 4.0$ nG and $n_B = -2.5$ for the left panel, and $B_{1\mathrm{Mpc}} = 3.0$ nG and $n_B = -1.0$ for the right panel. The compensated scalar and tensor modes are not shown because they have relatively smaller amplitudes. We also show the total magnetic contribution as the thick solid line.

in case that $B_{1\mathrm{Mpc}} = 4.0$ nG and $n_B = -2.5$, while the compensated vector mode is dominant for $\ell \gtrsim 4000$. When plotting Fig. 3.4, we fix the PMF generation epoch at the grand unified theory (GUT) phase transition, as $\eta_\nu/\eta_B = 10^{17}$. We also plot the measurements of the CMB temperature anisotropies obtained by Planck and SPT in Fig. 3.4.

3.5 Calculation of the compensated vector mode on small-scales

In this section, we focus on the compensated vector mode because it is the dominant PMF contribution to small-scale CMB anisotropies as mentioned in section 3.4. The vector-type induced CMB temperature anisotropies arise from the Doppler and integrated Sachs-Wolfe (ISW) effect [106], and the observable temperature anisotropies can be written as

$$\Theta(\eta_0, k, \hat{\boldsymbol{n}}) = \Big[\boldsymbol{v}_{\mathrm{b}}(\eta, k)\cdot\hat{\boldsymbol{n}}\Big]_{\eta_0}^{\eta_{\mathrm{rec}}} - \int_{\eta_0}^{\eta_{\mathrm{rec}}} d\eta\ \dot{\boldsymbol{V}}(\eta, k)\cdot\hat{\boldsymbol{n}}\ , \tag{3.21}$$

where $\hat{\boldsymbol{n}}$ is a line-of-sight unit vector, and $\eta_{\rm rec}$ denotes the recombination time. Also, $\boldsymbol{v}_{\rm b}(\eta)$ is divergence-free baryon velocity perturbation, and $\boldsymbol{V}(\eta)$ is the vector component of metric perturbation, which satisfies the gauge-invariance as defined in [107]. Therefore we need to solve the Euler equation of baryons for $\boldsymbol{v}_{\rm b}(\eta)$ and Einstein equation for $\boldsymbol{V}(\eta)$ to calculate the CMB anisotropies from the compensated vector mode. [4] In this work, we do not discuss the evolution of the vector potential $\boldsymbol{V}(\eta)$ because its contribution to the CMB anisotropies via the ISW effect is negligible. In other words, it is expected that the enhancement of the CMB anisotropies on small scales comes from the scale-dependence of the baryon velocity at the recombination, $\boldsymbol{v}_{\rm b}(\eta_{\rm rec}, k)$. In order to confirm this, we plot the fully numerical solution for $\boldsymbol{v}_{\rm b}(\eta_{\rm rec}, k)$ calculated by the Boltzmann code [103] in figure 3.5. This shows that the behavior of baryon velocity can be divided into three different scales: the large scale $k \lesssim k_S \approx 0.14$ Mpc^{-1}, the intermediate scale $k_S \lesssim k \lesssim k_{\rm mfp} \approx 0.38$ Mpc^{-1}, and the small scale $k \gtrsim k_{\rm mfp}$. Here k_S and $k_{\rm mfp}$ denote the Silk damping scale and the mean free path scale of the CMB at the recombination epoch, respectively.

For large and intermediate scales as $k \lesssim k_{\rm mfp}$, the evolution of the vector perturbation has been analytically studied with the tight-coupling approximation, $\boldsymbol{v}_{\rm b} \simeq \boldsymbol{v}_\gamma$ [88, 108]. According to their results, for the larger scales than the Silk scale (or on the earlier phase of the evolution), the baryon velocity is sourced by the PMF Lorentz force, and the photon velocity (i.e., dipole anisotropy $\boldsymbol{v}_\gamma$) catches up the baryon due to the Compton scattering. As a result, the baryon velocity and the photon dipole moment are growing with wavenumber (or time) together for $k \lesssim k_S \approx 0.1$ Mpc^{-1}. For the intermediate scales, the photon viscosity effect partially erases the baryon and photon velocity perturbations. Therefore the baryon velocity $\boldsymbol{v}_{\rm b}$ and the photon velocity $\boldsymbol{v}_\gamma$ starts to decay.

In fact, as shown in figure 3.5, the coupling between the baryons and photons continue to keep below the Silk scale. However, in case the velocity perturbation scale is smaller than the photon mean free path, the baryon-photon coupling no longer holds, and the baryon velocity starts to grow due to the PMFs again. Here, we try to explain k-dependence of the baryon velocity on such small scales, by analytically solving the Euler equation. When the dipole moment of photon is completely damped, the Euler equation in

[4] In fact, we also consider the Boltzmann equations of photons, dark matter, and neutrinos. However, these components do not give an impact on our discussion. Therefore we do not mention their evolution.

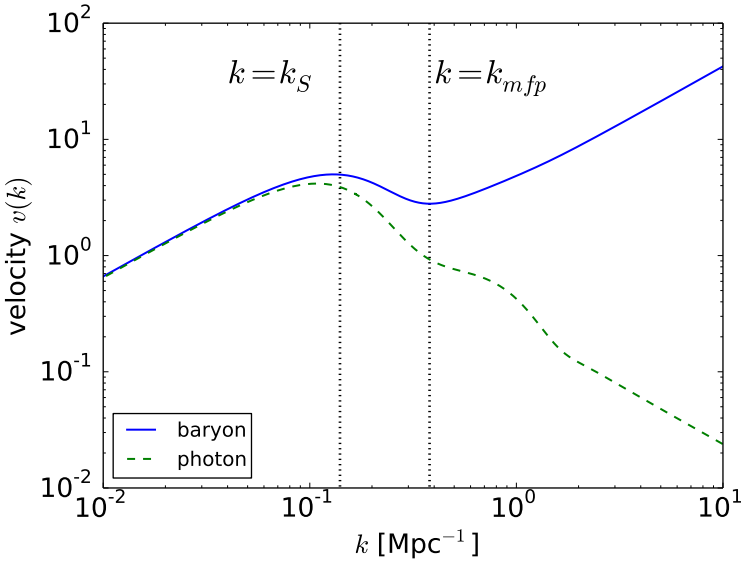

Figure 3.5: The scale-dependent baryon velocity perturbation and the photon dipole moment at the recombination are shown by the solid and dashed lines, respectively. The model parameters of the PMFs are fixed with $B_{1\mathrm{Mpc}} = 3.0$ nG and $n_B = -1.0$.

presence of the PMFs is given by

$$\left(\frac{\partial}{\partial t} + H + \frac{\tau'}{R}\right) \boldsymbol{v}_{\rm b} = -\frac{\rho_\gamma \boldsymbol{L}^{(V)}}{2a\rho_{\rm b}} \,, \tag{3.22}$$

in the non-relativistic limit [69, 109]. Here $\rho_{\rm b}$ and ρ_γ are the energy density of baryon and photon respectively, $R \equiv 3\rho_{\rm b}/4\rho_\gamma$ is the pressure ratio of baryon and photon, and $\tau' \equiv a n_e \sigma_{\rm T}$ is the photon opacity. The left side of equation (3.22) includes the Hubble expansion, Compton scattering, and the right side represents the Lorentz force due to the PMFs. After solving equation (3.22) with an initial condition as $\boldsymbol{v}_{\rm b}(a = a_{\rm i}) = \boldsymbol{v}_{\rm i}$, we obtain

$$\begin{aligned}\boldsymbol{v}_{\rm b}(k,a) =& \boldsymbol{v}_{\rm i} \exp\left\{\frac{\tau'}{2aHR}\left[1 - y^2(a)\right]\right\} \\ &- \frac{\rho_\gamma \boldsymbol{L}^{(V)}}{4aH\rho_{\rm b}}\left[{\rm Ei}\left(-\left.\frac{\tau'}{2aHR}\right|_{\rm i}\right) - {\rm Ei}\left(-\frac{\tau'}{2aHR}\right)\right] \exp\left(\frac{\tau'}{2aHR}\right) \,,\end{aligned} \tag{3.23}$$

with $y(a) \equiv a/a_{\rm i}$ is the scale factor normalized at the initial time, subscript "i" denotes the value at the initial time, and ${\rm Ei}(x) \equiv \int_{-\infty}^{x} e^t/t \; dt$ is the exponential integral. The first term on the right side in equation (3.23) represent the decaying due to the Compton scattering, and the second term is the inhomogeneous solution, which comes from the PMF source term, i.e., from the right side in the equation (3.22). We have confirmed that the solution (3.23) agrees with the full numerical calculation on much smaller scales than the Silk damping wavenumber, i.e., $k \gg k_S$, as shown in figure 3.6.

3.6 Data Analysis with Planck and SPT

In this work, we perform data analyses to constrain the PMF parameters, $(B_{\rm 1Mpc}, n_B, \tau_B)$, with the observational data of the CMB anisotropies. We apply the Markov Chain Monte Carlo (MCMC) method to the constraint on the PMFs. As one of the most popular methods to evaluate convergence, We impose a convergence criterion as the so-called Gelman-Rubin diagnostic with $R-1 < 0.01$. Here, R is the square root of the ratio of the marginalized variance of all chains and that for each chain. For the MCMC analysis, we use publicly available numerical codes, `MagCAMB` and `MagCosmoMC`, which are developed by Zucca et al. [103]. `MagCAMB` can solve the linearized Boltzmann and Einstein equations with the PMFs. Based on `CAMB` [110] and its modification [105], it was extended to calculate the CMB angular power spectra for

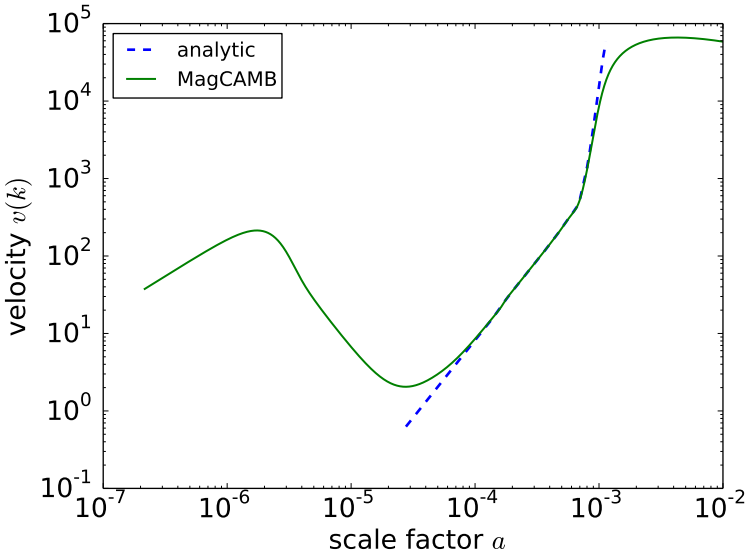

Figure 3.6: Numerical solution for the baryon velocity and the analytical solution that we have obtained. After the baryon velocity damps due to the photon viscous effect, our analytical solution is in good agreement with the numerical solution for $10^{-5} \lesssim a \lesssim 10^{-3}$. Here we fix $k = 1000$ Mpc^{-1} and the PMF parameters are the same as in figure 3.5.

all types of contributions sourced by the PMFs mentioned in the previous section. `MagCosmoMC` is developed, based on `CosmoMC` [111]. It enables us to explore cosmological parameters and the PMF model parameters with the foreground and data calibration parameters.

This study aims to investigate how the small-scale measurement of the CMB anisotropy by SPT improves the constraint on the PMF parameters, compared to the previous constraints by Planck data [103, 112]. First, we perform a likelihood analysis with only Planck low-ℓ ($2 \leq \ell \leq 29$) TT, EE, TE, and BB power spectra data, and high-ℓ ($30 \leq \ell \leq 2508$) TT, TE, and EE power spectra. This analysis has been already presented in references [103, 112]. Next, we use the combined data for Planck 2015 and SPTpol 2015/2017 for the first time. SPTpol 2015 data includes the BB power spectra in $300 \leq \ell \leq 2300$ for three spectral combinations, 95 GHz $\times$ 95 GHz, 95 GHz $\times$ 150 GHz, and 150 GHz $\times$ 150 GHz [113], and SPTpol 2017 data contains the TT, TE, and EE power spectra in $50 \leq \ell \leq 8000$ for the frequency band, 150 GHz $\times$ 150 GHz [104]. We note that Zucca et al. [103] has already studied the constraint on the PMFs with the Planck and SPTpol 2015 BB bandpowers. In this work, we update the constraint on the PMFs by adding small-scale TT, TE, and EE data from SPTpol 2017.

One problem is that the SPT 2017 bandpowers are partially overlapped with the Planck power spectra for $50 \leq \ell \leq 2508$. We have used both Planck and SPT for these multipole scales, and this leads to erroneously tighter constraints on the standard cosmological parameters. However, this BAO wiggle region around $200 \lesssim \ell \lesssim 3000$ is mainly determined by the standard cosmological parameters. Therefore we can expect that the constraint on the PMF parameters is not affected very much by using the duplicated CMB data on these scales.

We show the CMB temperature anisotropies measured by Planck and SPT in Figure 3.4. The PMF contributions to the CMB angular power spectra with $B_{1\mathrm{Mpc}} = 4.0$ nG, $n_B = -2.5$ are plotted in the left panel, and those with $B_{1\mathrm{Mpc}} = 3.0$ nG, $n_B = -1.5$ are shown in the right panel. Both of these parameter combinations are allowed by the previous constraint from Planck collaboration [112] with a 95% confidence level (C.L.). However, we expect that the high-ℓ CMB spectrum measured by SPT can constrain large n_B as shown in Figure 3.4. As clearly seen in Fig. 3.4, the CMB spectra observed by SPT have tiny errors on small-scales as $\ell \gtrsim 2000$, and the effect on such small-scale CMB anisotropy is dominated by the compensated vector mode, which is relevant for the parameter estimation using the SPT data. Finally, the blue-tilted PMF spectra (this corresponds to a large

spectral index n_B) that enhance the small-scale CMB anisotropies are tightly constrained by the high-ℓ CMB measurement of SPT.

3.7 Results and Discussion

First, we show the constraint on the PMF parameters, ($B_{1\mathrm{Mpc}}$, n_B), derived from `MagCosmoMC` with the Planck and SPT data in figure 3.7. The 2D constraint only with the Planck data is, as we have expected, almost the same in size and shape as the previous works [103, 112]. We have found the normalized PMF strength and the PMF spectral index can be constrained more tightly with the SPT data. For the constraint with Planck and SPT, the MCMC analysis consumes computing time dozens of times longer than for the Planck only. This is because the calculation includes the CMB anisotropies up to $\ell \sim 8000$, and there arises a strong degeneracy between the PMF parameters and foreground ones on such small scales. In figure 3.7, our analysis with the Planck and SPT does not reach the convergence of the MCMC analysis. Our analysis with the Planck and SPT in figure 3.7 finds $R > 10$. Therefore the 2D color contour in Figure 3.7 is not a smooth shape. However, the marginalized one-dimensional constraints on $B_{1\mathrm{Mpc}}$ and n_B seem to have smooth probability distribution functions in Figure 3.7. Besides, we found that, after reaching the current level of the constraint in Figure 3.7, the upper limit on the PMF parameters does not change for a long time during the calculation. Therefore we conclude that the constraint on the PMF parameters in Figure 3.7 is not far from the result that would be obtained from the converged MCMC analysis.

The results for the constraints on the standard cosmological parameters and the PMF ones from Planck and SPT data are presented in table 3.1. The PMF amplitude smoothed on 1 Mpc is constrained as $B_{1\mathrm{Mpc}} < 1.52$ nG for a 95 % confidence level (C.L.) when we include the SPT bandpowers for MCMC analysis, while the Planck 2015 data only put the upper limit as $B_{1\mathrm{Mpc}} < 3.18$ nG. The constraint on the magnetic spectral index is also improved, as $n_B < -1.14$ for Planck and SPT data and $n_B < -0.28$ for only Planck data. We find the high-ℓ SPT temperature anisotropy data favor the nearly scale-invariant PMF spectrum, as discussed in section 3.6. On the other hand, the change on η_ν/η_B mainly affects the amplitudes of the passive mode perturbation, and consequently, it influences the large-scale CMB anisotropies. Therefore we have an almost unchanged constraint on the η_ν/η_B when adding the small-scale SPT data for the parameter estimation. In table 3.1, although we put the best-fitted value for η_ν/η_B, we do not show

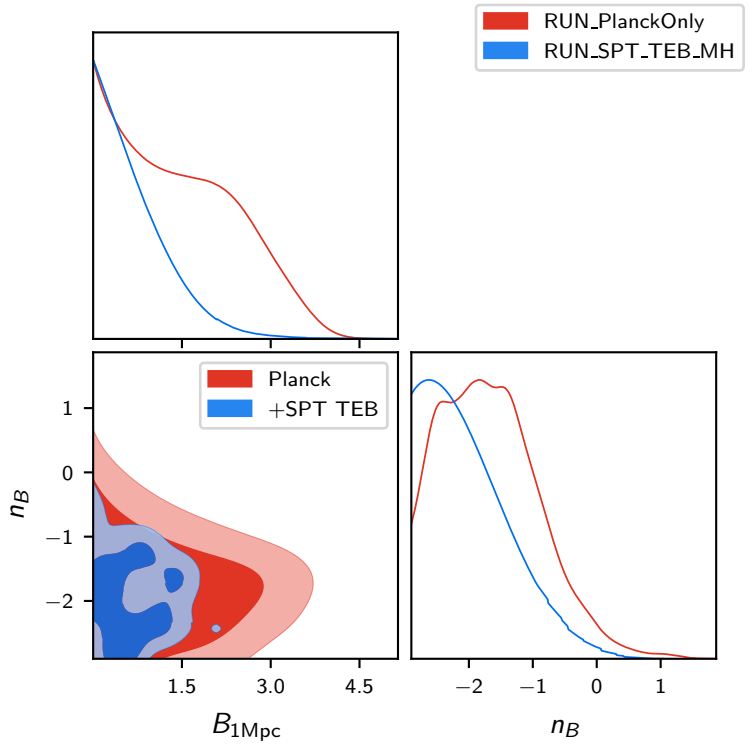

Figure 3.7: The constraint on the magnetic field strength $B_{1\mathrm{Mpc}}$ and the spectral index of PMFs n_B. The thick and thin color region stands for 68% and 95% confidence level (C.L.), respectively.

Table 3.1: The best-fitted values and constraints on the cosmological parameters and PMF model parameters are shown. The constraints on the cosmological parameters are with 68% C.L. Those for the epoch of the PMF generation, η_B, and the upper limits for $B_{1\mathrm{Mpc}}$ and n_B are with 95% C.L. The left two columns show the constraints from the Planck data and the Planck and SPT data without the PMF parameters, and the right two columns include the PMF parameters.

Parameters	ΛCDM		PMF	
	Planck	Planck + SPT	Planck	Planck + SPT
-log(likelihood)	6472.072	6557.605	6491.749	6610.238
# of parameters	78	94	81	97
$\Omega_b h^2$	0.0222 ± 0.00016	0.0223	0.0222	0.0224
$\Omega_c h^2$	0.1199 ± 0.0015	0.1190	0.1201	0.1177
$100\theta_{\mathrm{MC}}$	1.0407 ± 0.0003	1.0408	1.0408	1.0409
τ	0.078 ± 0.017	0.069	0.066	0.036
$B_{1\mathrm{Mpc}}$			< 3.182	< 1.515
n_B			$<$ -0.28	$<$ -1.14
$\log(\eta_\nu/\eta_B)$			$9.92^{+2.09}_{-5.92}$	9.41
$\ln(As \times 10^{10})$	3.092 ± 0.033	3.070	3.068	2.997
n_s	0.964 ± 0.005	0.966	0.962	0.968
H_0	67.20 ± 0.65	68.16	67.64	68.73

the error-bars for the Planck and SPT case. This is because we have used duplicated information of CMB angular power spectra for $50 \leq \ell \leq 2500$, and may we underestimate the error, as explained in section 3.6.

Next, we discuss the impact of the PMF parameter on the determination of the ΛCDM cosmological parameter. In Fig. 3.8, we compare the ΛCDM cosmological parameter constraint with only Planck data and that with Planck and SPT TT/TE/EE, and BB data, including the PMF parameters. As a comparison, we also summarize the best-fitted values of the cosmological parameters and the PMF parameters in case of Planck-only and Planck and SPT data analyses in table 3.1. Our results indicate that the cosmological parameter estimation can be biased when considering the PMF effects and the SPT high-ℓ data. In particular, Thomson optical depth

τ and the amplitude of the primordial power spectrum for the scalar sector A_s decrease by 1-2 σ compared with the Planck only analysis. The SPT TT data favor nearly scale-invariant spectra of the PMFs as shown in Fig. 3.7. For such PMFs, the passive tensor mode significantly enhances the low-ℓ EE power spectrum. To compensate for the enhancement on large scales by the PMFs, the MCMC chooses the small optical depth τ, which also contributes to the signals on the large-scale EE power spectrum.

As dedicated in section 3.6, the measured multipole ranges of the TT/TE/EE spectra which we have used are overlapped for Planck and SPT in $50 \lesssim \ell \lesssim 2500$. However, this is not harmful to our results because the CMB power spectra for these angular scales are almost determined only by the cosmological parameters, and are not affected by the PMF contribution very much. We have confirmed that the best-fitted values of the cosmological parameters are not changed for Planck and Planck+SPT when excluding the PMFs for our analyses (ΛCDM case). For similar reasons, we do not perform BICEP2/Keck-Planck joint analysis [103, 112].

Before closing this section, we make some comments on other PMF effects on the CMB anisotropies, which are not included in our analysis. Previous studies predict the generation of the helical PMFs during inflation [114–117]. While such helical PMFs can induce the parity-odd spectrum, TB and EB, the contributions of the helical part of the PMFs to the parity-even TT, TE, EE, and BB power spectra are always subdominant in comparison with the contribution of the non-helical PMFs [112]. Therefore, adding the helical component of the PMFs to parameter estimation would not significantly change our constraint. The dissipation of magnetic fields before the recombination epoch also affects the thermal history and recombination history of the baryon gas [109, 118–120]. Including this effect can improve the constraint on the PMFs via increasing the energy density of CMB photons [121], creating y-type distortion [122, 123], and changing the evolution of Thomson optical depth [73]. Including these effects may improve our constraint on the PMFs, in particular, with a large spectral index. However, the dissipation of the PMFs is a highly non-linear effect, and there is still a large uncertainty in the calculation of this effect. Therefore we neglect the dissipation process in our analysis. Besides, the PMFs can induce non-Gaussian CMB anisotropies [124, 125]. The current constraint on the non-Gaussianity in the CMB anisotropies by Planck observation provides the same order of ours [112]. Furthermore, the CMB polarization map should be altered by Faraday rotation if the PMFs exist. The Planck collaboration puts an upper limit on the PMF strength via the Faraday rotation, and the resultant constraint is much weaker than via the other effects de-

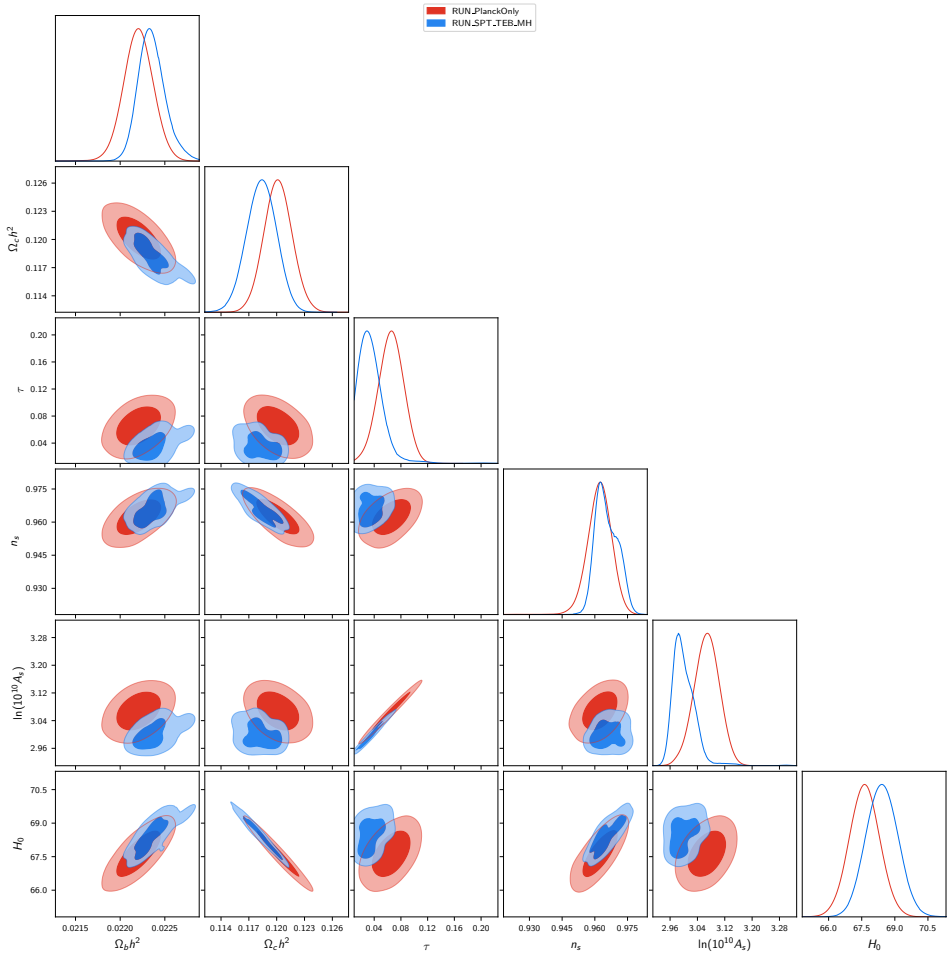

Figure 3.8: The constraint on the magnetic field strength $B_{1\mathrm{Mpc}}$ and the spectral index of the PMFs n_B. The thick and thin color region stands for 68% and 95% confidence level, respectively. The red (RUN-PlanckOnly) and blue (RUN-SPT-TEB-MH) contours indicate the constraints from Planck 2015 data and those from both Planck and SPT data, respectively.

scribed here. Therefore, we have neglected the effect of the Faraday rotation from the PMFs in our analysis.

Chapter 4

Creation of CMB secondary anisotropies

4.1 Cosmic magnetism and gas physics

The PMFs affect the baryon gas dynamics even after the recombination epoch. In particular, we focus on two effects: creation of the matter density fluctuations due to the Lorentz force, and heating of the IGM gas due to the ambipolar diffusion of the PMFs. Such hot and dense IGM gas can leave an observational signature with the CMB temperature anisotropies, via the so-called thermal Sunyaev-Zel'dovich (tSZ) effect as explained in section 4.2. In this section, we discuss the time evolution of the IGM gas density and temperature with consideration of the PMFs.

4.1.1 IGM density fluctuations due to PMFs

As investigated in the previous study [126, 127], the evolutional equations of the density fluctuations for cold dark matter $\delta_{\rm c}(t)$ and baryons $\delta_{\rm b}(t)$ at time t are written as

$$\ddot{\delta}_{\rm c}(t) + 2\frac{\dot{a}(t)}{a(t)}\dot{\delta}_{\rm c}(t) - 4\pi G[\rho_{\rm c}(t)\delta_{\rm c}(t) + \rho_{\rm b}(t)\delta_{\rm b}(t)] = 0 \ , \tag{4.1}$$

$$\ddot{\delta}_{\rm b}(t) + 2\frac{\dot{a}(t)}{a(t)}\dot{\delta}_{\rm b}(t) - 4\pi G[\rho_{\rm c}(t)\delta_{\rm c}(t) + \rho_{\rm b}(t)\delta_{\rm b}(t)] = S(t) \ . \tag{4.2}$$

where $\dot{X}$ represents the time derivative of X, and $\rho_{\rm b,c}$ are the densities of baryons (b) and cold dark matter (c), respectively. Also, $S(t)$ is the source

term due to the Lorentz force of the PMFs and given by

$$S(t) = \frac{\nabla \cdot (\nabla \times \boldsymbol{B}(\boldsymbol{x}, t)) \times \boldsymbol{B}(\boldsymbol{x}, t)}{4\pi \rho_{\rm b}(t) a^2(t)} \,, \tag{4.3}$$

where ∇ is taken in the comoving coordinate.

Now we write the total matter density and density fluctuation as $\rho_{\rm m}(t) = \rho_{\rm c}(t) + \rho_{\rm b}(t)$ and $\delta_{\rm m}(t) \equiv [\rho_{\rm c}(t)\delta_{\rm c}(t) + \rho_{\rm b}(t)\delta_{\rm b}(t)]/\rho_{\rm m}(t)$, the evolutionary equation for $\delta_{\rm m}(t)$ can be obtained from Eqs. (4.1) and (4.2) as

$$\ddot{\delta}_{\rm m}(t) = -2\frac{\dot{a}(t)}{a(t)}\,\dot{\delta}_{\rm m}(t) + 4\pi G \rho_{\rm m}(t)\delta_{\rm m}(t) + \frac{\rho_{\rm b}(t)}{\rho_{\rm m}(t)} S(t) \tag{4.4}$$

We can obtain the solution of Eq. (4.4) analytically by the Green function method. Taking $D_1(t)$ and $D_2(t)$ as the special solutions of Eq. (4.4) with $S(t) = 0$, we can obtain the general solution as

$$\delta_{\rm m}(t) = AD_1(t) + BD_2(t) - D_1(t)\int_{t_i}^{t} dt' \frac{S(t')D_2(t')}{W(t')} - D_2(t)\int_{t_i}^{t} dt' \frac{S(t')D_1(t')}{W(t')} \,. \tag{4.5}$$

Constants A and B are determined by the initial conditions of $\delta_{\rm m}$ and $\dot{\delta_{\rm m}}$, and $W(t)$ is the Wronskian and given by $W(t) = D_1(t)\dot{D}_2(t) - D_2(t)\dot{D}_1(t)$.

From here, we assume the matter-dominated universe because we are interested in the structure formation after the recombination. Then, we can find the homogeneous solutions for Eq. (4.4) as

$$D_1(t) \propto t^{-1}, \quad D_2(t) \propto t^{\frac{2}{3}} \,. \tag{4.6}$$

With these homogeneous solutions, we can find the inhomogeneous one as

$$\delta_{\rm m}(t) = \frac{3}{5}\frac{\Omega_{\rm b}}{\Omega_{\rm m}}\left[\frac{3}{2}\left(\frac{t}{t_i}\right)^{\frac{2}{3}} + \left(\frac{t}{t_i}\right) - \frac{5}{2}\right] S(t_i)t_i \,, \tag{4.7}$$

and $\delta_{\rm b} = 0$ initially, we can write the evolution of $\delta_{\rm b}$ as

$$\begin{aligned}\delta_{\rm b} = \frac{2S(t)}{15H^2(t)}\Bigg[&\left(3y_{\rm r} + 2y_{\rm r}^{-3/2} - 15\ln y_{\rm r}\right)\frac{\Omega_{\rm b}}{\Omega_{\rm m}} \\ &+15\ln y_{\rm r} + 30\left(1 - \frac{\Omega_{\rm b}}{\Omega_{\rm m}}\right)y_{\rm r}^{-1/2} - \left(30 - 25\frac{\Omega_{\rm b}}{\Omega_{\rm m}}\right)\Bigg] \,,\end{aligned} \tag{4.8}$$

where $\Omega_{\rm m}$ and $\Omega_{\rm b}$ are the density parameters of total matter and baryons, respectively, and $a_{\rm rec}$ is the cosmic scale factor at the recombination epoch. Note that Eqs. (4.1) and (4.2) are valid only when $\delta_{\rm b} \ll 1$ and the baryon pressure is negligible. We discuss the validity of these assumptions later.

4.1.2 Thermal history of the IGM gas

In addition to the density fluctuations, IGM gas temperature is also affected by the PMFs. After the cosmic recombination, the ionization fraction of the IGM gas rapidly decreases. However, a small fraction of the IGM gas remains ionized, and these ionized particles feel the Lorentz force of the PMFs, while neutral particles do not feel it. Resultantly, there comes a relative motion between ionized and neutral particles. The bulk energy due to this relative motion is dissipated to the thermal energy of the IGM gas by collisional friction between ionized and neutral particles, which is the process known as the ambipolar diffusion. The evolutional equation of the gas temperature $T_{\rm gas}$ with the ambipolar diffusion is given by [128]

$$\begin{aligned}\frac{dT_{\rm gas}}{dt} =& -2H(t)T_{\rm gas} + \frac{\dot{\delta}_{\rm b}}{1+\delta_{\rm b}}T_{\rm gas} + \frac{x_{\rm i}}{1+x_{\rm i}}\frac{8\rho_\gamma\sigma_{\rm T}}{3m_{\rm e}c}(T_\gamma - T_{\rm gas}) \\ &+ \frac{\Gamma(t)}{1.5k_{\rm B}n_{\rm b}} - \frac{x_{\rm i}n_{\rm b}}{1.5k_{\rm B}}[\Theta x_{\rm i} + \Psi(1-x_{\rm i}) + \eta x_{\rm i} + \zeta(1-x_{\rm i})],\end{aligned} \tag{4.9}$$

where $x_{\rm i}$ is the ionization fraction of the IGM gas, $\sigma_{\rm T}$ is the Thomson scattering cross section, $m_{\rm e}$ is the electron mass, $k_{\rm B}$ is the Boltzmann constant, $n_{\rm b}$ is the IGM baryon number density, and the subscript γ denotes the values for the CMB photons. The first, second, and third term in the right-hand side of Eq. (4.9) represent the adiabatic cooling by the expansion of the Universe, adiabatic compression or expansion due to the local density fluctuations, and the Compton cooling (or heating), respectively. The fourth term represents the extra heating of the IGM gas due to the PMF energy dissipation. Here the heating rate $\Gamma(t)$ is given by [119]

$$\Gamma(t) = \frac{|(\nabla\times\boldsymbol{B}(t,\boldsymbol{x}))\times\boldsymbol{B}(t,\boldsymbol{x})|^2}{16\pi^2\xi\rho_{\rm b}^2(t)}\frac{(1-x_{\rm i})}{x_{\rm i}}, \tag{4.10}$$

where we adopt the drag coefficient $\xi = 3.5\times10^{13}$ [cm^3 g^{-1} s^{-1}] from Ref. [129]. The last term in the Eq. (4.9) stands for the several cooling effects; i.e., the free-free cooling (bremsstrahlung), the collisional excitation cooling, the recombination cooling, and the collisional ionization cooling. We write these cooling coefficients as Θ, Ψ, η, and ζ, respectively, and these values are referred from Fukugita and Kawasaki [128].

When solving Eq. (4.9), we need to calculate the ionization fraction $x_{\rm i}$. According to Refs. [119, 130], time evolution of the IGM ionization fraction

is given by

$$\frac{dx_{\rm i}}{dt} = \left[-\alpha_e n_{\rm b} x_{\rm i}^2 + \beta_e (1-x_{\rm i}) \exp\left(-\frac{\Delta E_{12}}{k_{\rm B} T_\gamma}\right)\right] D + \gamma_e n_{\rm b} (1-x_{\rm i}) x_{\rm i}, \quad (4.11)$$

where we adopt the three-levels model, with the ground state ($n = 1$), the first excited state ($n = 2$), and the continuum ($n > 2$) based on the `RECFAST` code [130, 131]. In Eq. (4.11), $\Delta E_{12} = h_{\rm Pl} c/\lambda_{12} = 10.2$ eV represents the energy of Ly-α photon, and D is the suppression factor due to the Ly-α resonance photons, which is given by

$$D = \frac{1 + K\Lambda n_{\rm b}(1-x_{\rm i})}{1 + K\Lambda n_{\rm b}(1-x_{\rm i}) + K\beta_e(1-x_{\rm i})}, \quad (4.12)$$

with the Ly-α redshift rate $K \equiv \lambda_{12}^3/8\pi H(t)$, and the two-photon emission coefficient $\Lambda = 8.22458$ s^{-1} [130]. The first, second, and last terms in the right-hand side in Eq. (4.11) represent the collisional recombination, the photoionization and the collisional ionization, respectively. With the definitions of the hydrogen energy levels, $E_n = -13.6/n^2$ [eV] (n=1,2), those coefficients are given by

$$\alpha_e = 1.14 \times 10^{-13} \times \frac{4.309\ T_4^{-0.6166}}{1 + 0.6703\ T_4^{0.5300}}\ \ [{\rm cm}^3\ {\rm s}^{-1}], \quad (4.13)$$

$$\beta_e = \alpha_e \left(\frac{2\pi m_{\rm e} k_{\rm B} T_\gamma}{h_{\rm Pl}^2}\right)^{\frac{3}{2}} \exp\left(\frac{E_2}{k_{\rm B} T_\gamma}\right)\ \ [{\rm s}^{-1}], \quad (4.14)$$

$$\gamma_e = 0.291 \times 10^{-7} \times U^{0.39} \frac{\exp(-U)}{0.232 + U}\ \ [{\rm cm}^3\ {\rm s}^{-1}], \quad (4.15)$$

with $T_4 = T_{\rm gas}/10^4$ K and $U = |E_1/k_{\rm B} T_{\rm gas}|$ as in `RECFAST` code [131]. Here, note that the original `RECFAST` code uses the gas temperature $T_{\rm gas}$ instead of the CMB one T_γ in the definition of β_e in Eq. (4.14). However, Chluba et al. [120] has pointed out the `RECFAST` code might overestimate the ionization fraction when the extra heating decouples the gas temperature from the CMB photon temperature. In this work, the PMFs can heat up the IGM gas up to $T_{\rm gas} \sim 10^{3-4}$ K, as described in section 4.4. Therefore, we adopt Eq. (4.14) to calculate the ionization fraction of the IGM gas.

For simplicity, we do not include any astrophysical ionizing sources, such as the UV and X-ray photons emitted from the stars, galaxies, AGNs, and so on. We also neglect the primordial helium and heavier elements. When we calculate the IGM thermal history Eqs. (4.9) and (4.11), we take into account the fluctuations of the hydrogen number density $n_{\rm H}$ and mass density $\rho_{\rm b}$ in situ, which are evaluated by Eq. (4.8).

4.2 SZ angular power spectrum

In the previous section, we discuss the impacts of the PMFs on the IGM gas density, temperature, and the ionization fraction. When the PMFs are tangled, these physical values in the IGM gas fluctuate. Such fluctuated gas can create the CMB temperature anisotropies through the inverse-Compton scattering, which is the so-called thermal Sunyaev-Zel'dovich (tSZ) effect. In this section, we describe the tSZ effect and its angular power spectrum induced by the PMFs.

4.2.1 tSZ effect as a secondary CMB anisotropy

In Chapter 3, we introduce the CMB temperature anisotropy and the relation between the observable temperature and the angular power spectrum. In this subsection, we focus on the Sunyaev-Zel'dovich effect, which is the mechanism to distort the black-body spectrum of CMB photons, and to induce the secondary CMB temperature anisotropies [132, 133]. Sunyaev and Zel'dovich 1969 [132, 133] have suggested that the energy spectrum of the CMB photon can be changed when hot ionized gas causes the inverse Compton scattering with the CMB photons. This effect is called "thermal Sunyaev-Zel'dovich effect" (tSZ effect), and a lot of radio telescopes have already confirmed this effect. tSZ effect is usually caused by the hot electron gas in galaxy clusters with typical temperature $\sim 10^7$–10^8 K. For another case of the CMB spectral distortion due to the inverse-Compton scattering, the kinematic SZ effect (kSZ effect) is caused by the line-of-sight component of the bulk velocity of the hot electron gas cloud. The tSZ effect and kSZ effect are called the SZ effect, generally.

The photon distribution function $f(\nu, t)$ with time t and frequency ν obeys the photon Boltzmann equation. Using the Fokker-Planck expansion of the Boltzmann equation lead us to obtain the following Kompaneets equation [99]

$$\frac{\partial f(\nu,t)}{\partial y} = \frac{1}{x^2}\frac{\partial}{\partial x}\left(x^4 \frac{\partial f(\nu,t)}{\partial x}\right) , \tag{4.16}$$

where

$$x(\nu) \equiv \frac{h_{\rm Pl}\nu}{k_{\rm B}T_\gamma} , \tag{4.17}$$

and

$$y(\hat{\boldsymbol{n}}, t) \equiv \frac{k_{\rm B}\sigma_{\rm T}}{m_{\rm e}c^2}\int_0^{\chi(t)} d\chi' \; a'_\chi w(\chi', \hat{\boldsymbol{n}}) . \tag{4.18}$$

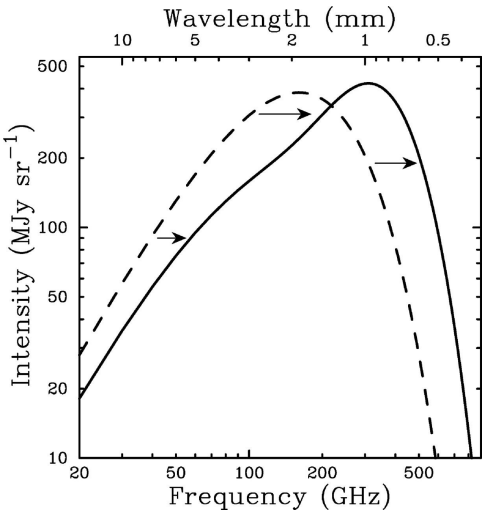

Figure 4.1: The undistorted CMB spectrum (dotted) and the distorted one by SZ effect (solid). To illustrate the distortion clearly, this distortion is assumed to be caused by a galaxy cluster which is 1000 times more massive than the typical galaxy clusters. The dotted and solid lines intersect at the frequency of 218 GHz (wavelength of 1.38 nm). This figure is referred to as from [134].

This quantity $y(\hat{\boldsymbol{n}}, t)$ is called the Compton y-parameter on the line-of-sight direction [99], and this characterize the strength of the tSZ effect. In Eq. (4.18), χ, a_χ, and $\hat{\boldsymbol{n}}$ are the comoving distance, the unit vector to the line-of-sight, and the scale factor corresponding to χ, respectively. Also, $w(\chi, \hat{\boldsymbol{n}})$ is the function of $n_{\rm b}$, $x_{\rm i}$ and $T_{\rm gas}$ at a comoving three-dimensional position $\boldsymbol{x} = \chi\hat{\boldsymbol{n}}$, and given by

$$w(\chi, \hat{\boldsymbol{n}}) = x_{\rm i} n_{\rm b} (T_{\rm gas} - T_\gamma)\big|_{\boldsymbol{x}} \ . \tag{4.19}$$

Kompaneets equation (4.16) is derived with the assumptions that the free electrons are non-relativistic and follow the Maxwell-Boltzmann distribution function. After solving Eq. (4.16), we can find the altered photon spectral energy distribution as the decrement in the low-energy side (Rayleigh-Jeans region) and increment in the high-energy side (Wien region). Also, the frequency where the photon distribution function is unchanged is independent on the gas temperature or when the scattering occurs, and this is determined as $x \simeq 3.83,\ \nu \simeq 218$ GHz, $\lambda \simeq 1.38$ nm. For the illustrative understanding, we show the CMB spectral distortion due to the tSZ effect in Fig. 4.1.

4.2.2 CMB temperature angular spectrum due to the tSZ effect

The Compton y-parameter in Eq. (4.18) is related with the CMB temperature anisotropies caused by the tSZ effect depending observed frequencies as

$$\frac{\Delta T}{T}(\hat{\boldsymbol{n}}, \nu) = g(\nu)\ y(\hat{\boldsymbol{n}}, t_0)\ , \tag{4.20}$$

where t_0 is the present time, and $g(\nu)$ is the spectral function of the tSZ effect given by $g(\nu) = -4 + x/\tanh(x/2)$ with $x \equiv h_{\rm Pl}\nu/k_{\rm B}T$. Especially, $g(\nu)$ in the Rayleigh-Jeans (low-frequency) limit goes to $g(\nu) \to -2$ as $\nu \to 0$.

According to Eq. (4.20), we can obtain the tSZ angular power spectrum as

$$C_\ell = \left[\frac{g(\nu)k_{\rm B}\sigma_{\rm T}}{m_{\rm e}c^2}\right]^2 \int d\chi \frac{P_w(\chi, \ell/\chi)}{\chi^2}\ . \tag{4.21}$$

Here ℓ is a multipole moment, and $P_w(\chi, k)$ is the three-dimensional power spectrum of the Compton y-parameter at a comoving distance χ. We obtain $P_w(\chi, k)$ from w defined by Eq. (4.19). When deriving Eq. (4.21), we adopt the Limber's approximation because we are interested in large ℓ modes.

4.3 Simulation Setup

We calculate the CMB angular power spectrum due to the tSZ effect from Eqs. (4.18) and (4.21) with the solutions for Eqs. (4.8), (4.9) and (4.11) for a given spatial distribution of the PMFs. Because this equation system is nonlinear, we perform numerical simulations to find the spatial distributions of the gas density, temperature, and ionization fraction and calculate the tSZ angular power spectrum from their fluctuations.

As explained in Chapter 2, the statistical property of the PMFs in our work is determined by only two parameters, B_n and n_B. We investigate the tSZ anisotropies induced by the PMFs with some combinations of these PMF parameters in Table 4.3. These parameters are consistent with the Planck constraint on the PMFs [112].

Now we explain the details of the simulation setup. At first, we set the calculation box size to $(1\ {\rm Mpc})^3$. It is required to resolve the cut-off scale in Eq. (2.30) to accurately generate the magnetic field distribution. We adopt the grid numbers as summarized in Table 4.3, which are enough to resolve the cut-off scale of the PMFs.

Table 4.1: The models of PMFs adapted in this work. Each column represents the model number, the PMF strength B_n, the spectral indices n_B, the cut-off length in real space λ_c, the box length of the calculation volume $L_{\rm box}$, the grid size of numerical calculation $L_{\rm grid}$, from left to right, respectively.

No.	B_n [nG]	n_B	λ_c [kpc]	$L_{\rm box}$ [Mpc]	$L_{\rm grid}$ [kpc]
1	0.5	2.0	318	2.0	31.25
2	0.5	1.0	263	1.0	15.625
3	0.5	0.0	201	1.0	15.625
4	0.5	-1.0	135	1.0	15.625
5	0.1	2.0	200	1.0	15.625
6	0.1	1.0	154	1.0	15.625
7	0.1	0.0	106	1.0	15.625
8	0.1	-1.0	60.3	0.5	7.8125
9	0.05	2.0	165	1.0	15.625
10	0.05	1.0	122	1.0	15.625
11	0.05	0.0	80.1	0.5	7.8125
12	0.05	-1.0	42.6	0.25	3.90625
13	0.01	2.0	104	0.5	7.8125
14	0.01	1.0	71.3	0.5	7.8125
15	0.01	0.0	42.1	0.25	3.90625
16	0.01	-1.0	19.1	0.25	3.90625

To erase the divergence of the PMFs numerically, we first make a distribution of the vector potential field, $\boldsymbol{A}(\boldsymbol{k})$, in three-dimensional wave-number space. Then, the PMF strength $\boldsymbol{B}(\boldsymbol{k})$ are obtained by

$$\boldsymbol{B}(\boldsymbol{k}) = i\boldsymbol{k} \times \boldsymbol{A}(\boldsymbol{k}). \tag{4.22}$$

In this way, the divergenceless condition $\nabla \cdot \boldsymbol{B} = 0$ is automatically satisfied. Besides, a distribution of $\nabla \times \boldsymbol{B}(\boldsymbol{k})$ is calculated by the outer product of $i\boldsymbol{k}$ and $\boldsymbol{B}(\boldsymbol{k})$ in wave-number space. Then, we perform the inverse Fourier transformation of these values to obtain $\boldsymbol{B}$ and $\nabla \times \boldsymbol{B}$ in real space. From these distributions, we can evaluate the source terms of the density fluctuation and gas temperature in Eqs. (4.8) and (4.9) in real space.

To save the computational resources, our calculation of gas density, temperature, and ionization fraction, which are represented by Eqs. (4.8), (4.9), and (4.11), are performed at each cell in the simulation box, independently. We adopt the fourth-order Runge-Kutta method as the solver for Eqs. (4.9)

and (4.11), and make output data at 67 redshift slices taken logarithmically from $z = 1000$ to $z = 10$. We then calculate the power spectrum $P_w(\chi(z), k)$, at each redshift slice. We integrate these power spectra with the linear interpolation between the slices and, finally, we obtain the angular power spectrum in Eq. (4.21).

4.4 Results and Discussion

We perform our simulations for four different PMF models with the parameter sets listed in Table 4.3. Depending on the PMFs, the evolutions of the gas quantities, $\delta_{\rm b}$, $T_{\rm gas}$ and $x_{\rm i}$, are different. First, we focus on the PMF dependence of these values.

In the left column of Fig. 4.2, we show the co-moving two-dimensional structure of the x-component of $(\nabla \times \boldsymbol{B}) \times \boldsymbol{B}$, which are the Lorentz force terms appeared in Eqs. (4.3) and (4.10). Each panel in Fig. 4.2 corresponds to the case for models 1–4 listed in Table 4.3, from top to bottom, respectively. We do not show the results for models 5–16 while we have calculated these cases. The middle and right columns are the results for the ionization fraction and the hydrogen number density maps at $z = 10.0$, respectively. For all PMF models, the IGM gas is heated up to ~ 20000 K due to the ambipolar diffusion, in regions where the Lorentz force is strong. In addition, the gas densities are extremely lower in such regions because the divergence of the Lorentz force is negative. Since the collisional recombination rate is not so effective in such underdense regions, the ionization fraction of the IGM gas maintains around the unity, even when the redshift is around 10. Therefore, the correlation between $x_{\rm ion}$ and $n_{\rm H}$ is always negative. We also comment that the cut-off length in Table 4.3 corresponds to the fluctuation scale shown in Fig. 4.2. We also find that the density contrast rapidly evolves as $|\delta_{\rm b}| \gg 1$, as small scale as the resolution of our simulation, even soon after the recombination. Therefore we set the lower limit of the density fluctuations to $\delta_{\rm b} = -0.9$ to avoid the negative density. Since it is linearized, Eq. (4.8) is not valid in such a highly nonlinear regime. We discuss this point at the end of this section.

Figure 4.3 shows the time evolutions of the spatial-averaged gas temperature (top) and the ionization fraction (bottom), for different PMF models. We obtain these values by density-weighted averaging. Thus Fig. 4.3 mainly reflects the quantities in overdense regions. Here, the heating rate of the IGM gas due to the PMF dissipation in Eq. (4.9) is proportional to the inverse square of the baryon mass density, and heating efficiency be-

comes suppressed in high-density regions. Actually, the top panel of Fig. 4.3 shows that although the gas mean temperature keeps increasing soon after the recombination, it turns downward after reaching 3000–4000 K around $z \sim 300$. At the earlier stage of the evolution as $z \gtrsim 300$, the density fluctuation has not yet grown so much, and, the heating efficiency can be still high at almost all cells. However, the non-linear evolution of the density contrast starts after $z \sim 300$, and the heating rate due to the Lorentz force keeps lowering because of the cosmic expansion. Consequently, the gas densities in the high-density regions start to drop. We also find the dependence of the gas temperature on the PMF models is small, as shown in Fig. 4.3. The difference between the gas temperatures for model 1 and 4 is within the factor of 2, even at $z = 10$. This is because the saturated temperature at high redshifts does not depend on the PMF model, and it is mainly determined by the atomic cooling effects and the ionization fraction. After the saturation, the gas temperature gradually decreases with the balance of the cooling and heating effects. Thus, the PMF model dependence of the IGM gas temperature is small for the magnetic field strengths considered in this work. Although it is not apparent in Fig. 4.3, we also investigate the gas temperature evolutions in the underdense regions. We find that the gas temperature in such low-density regions quickly increases soon after the recombination epoch as well as that in the high-density regions. However, the gas temperature in the low-density regions keeps as high as the saturated temperature even in the lower redshifts.

We show the density-weighted average of the ionization fractions $x_{\rm i}$ in the bottom panel of Fig. 4.3. Contrary to the gas temperature evolution, the averaged value of the ionization fraction does not simply agree with the values in high-density regions. This is because the typical ratio of the ionization fraction values in the high-density region to the low-density region is much larger than that of the density contrast values, i.e., $(\rho x_{\rm i})^{\text{high density}} < (\rho x_{\rm i})^{\text{low density}}$. As we can expect, the ionization fraction in lower density regions keeps $x_i \approx 1$ after the recombination epoch. This is because the collisional recombination term in Eq. (4.11) becomes small in such a low-density region. On the other hand, as the IGM gas density evolves in the high-density region, the collisional recombination becomes effective and the ionization fraction quickly drops down. We find out that, while $x_{\rm i} \approx 1$ at the lowest density regions where $\delta_{\rm b} = -0.9$, $x_{\rm i} \approx 10^{-7}$ at the highest density regions with $\delta_b > 10^3$. Because of this huge gap in $x_{\rm i}$ between low- and high-density regions, the density-weighted average value of $x_{\rm i}$ does not only reflect $x_{\rm i}$ in high-density regions. Basically, the full ionization in low-density regions makes the average value of the ionization fraction larger than that

without PMFs plotted in black in Fig. 4.3. On the other hand, the almost neutral gas in high-density regions can decrease the average value below that without PMFs (see the yellow short dash-dotted line around $z \sim 600$ in the bottom panel of Fig. 4.3). In summary, the averaged value of $x_{\rm i}$ is determined by the balance between low and high-density regions. Although the ionization fraction is larger for the stronger PMF strength at the cut-off scale, the model dependence is not so significant.

We show the CMB temperature angular power spectrum due to the tSZ effect in the IGM caused by PMFs in Fig. 4.4. The tSZ angular power spectrum has a peak around the cut-off scale of the PMFs and the amplitude depends on the PMF strength at the cut-off scale. Therefore, the angular spectrum in model 1 has the largest amplitude among our PMF models. However, it is difficult to provide the dependence of the power spectrum amplitude on the PMF parameters in the analytical form. This is because the physical gas quantities related to the tSZ effect are highly nonlinear and become saturated in some regions. We also find that the tSZ angular power spectrum decays proportional to ℓ on larger scales than the cut-off scale independently on the spectral index of the PMF, n_B. This means that the tSZ effect comes from the magnetic field predominantly on the cut-off scale, and magnetic fields on larger scales have little impact on the tSZ CMB power spectrum. Although we have shown the results with $n_B = 0.0$ and -1.0 in Fig. 4.4, we have confirmed that n_B indeed affects tSZ anisotropies only through the cut-off scale in the cases with $-1.0 < n_B < 2.0$. However, it does not necessarily mean that the tSZ angular power spectrum is insensitive to n_B because the cut-off scale does depend on n_B. Therefore, we conclude that, although the measurement of the tSZ effect due to the PMFs can provide the information about the cut-off scale of the PMFs, it is required to perform a careful comparison between the observational data and the theoretical prediction to deduce the properties of the PMFs, such as the field strength and the spectral index.

At the end of this section, we make comments on the validity of the gas density evolution and the impact on the final results. To obtain the density evolution, we solve Eqs. (4.1) and (4.2) in which we make two important assumptions, i.e., neglecting the thermal pressure and employing linear perturbations. For the validity of the former assumption, we have confirmed that the grid scales of our simulations are always larger than the Jeans scale. On the other hand, as already mentioned above, we find that there are many regions where the density contrast is much larger than unity and the linear approximations are no longer valid. However, such high-density regions have a tiny ionization fraction in general due to the collisional recombination

process. As a result, the contribution to the tSZ angular power spectrum is negligibly small. The overestimation of the gas density does not harm our final results. As regards low-density regions, we set the lower limit of the IGM density contrast to $\delta_{\rm b} = -0.9$ in order to avoid a negative IGM density. This procedure means that we artificially take into account the nonlinear structure formation, that is, the void formation, because voids are observed as significant underdense regions with $\delta_{\rm b} < -0.85$ [136]. This limit violates the mass conservation in a simulation box. However, although this violation leads to the overestimation of the density in overdense regions, it does not seem to give a negative impact on the estimation of the y-parameter in low-density regions which produces significant contributions on the tSZ angular power spectrum. To confirm this point, it is required to calculate the tSZ spectrum including the nonlinear effect in the IGM density evolution. We perform the numerical simulations in our future work to take into account this nonlinear effect.

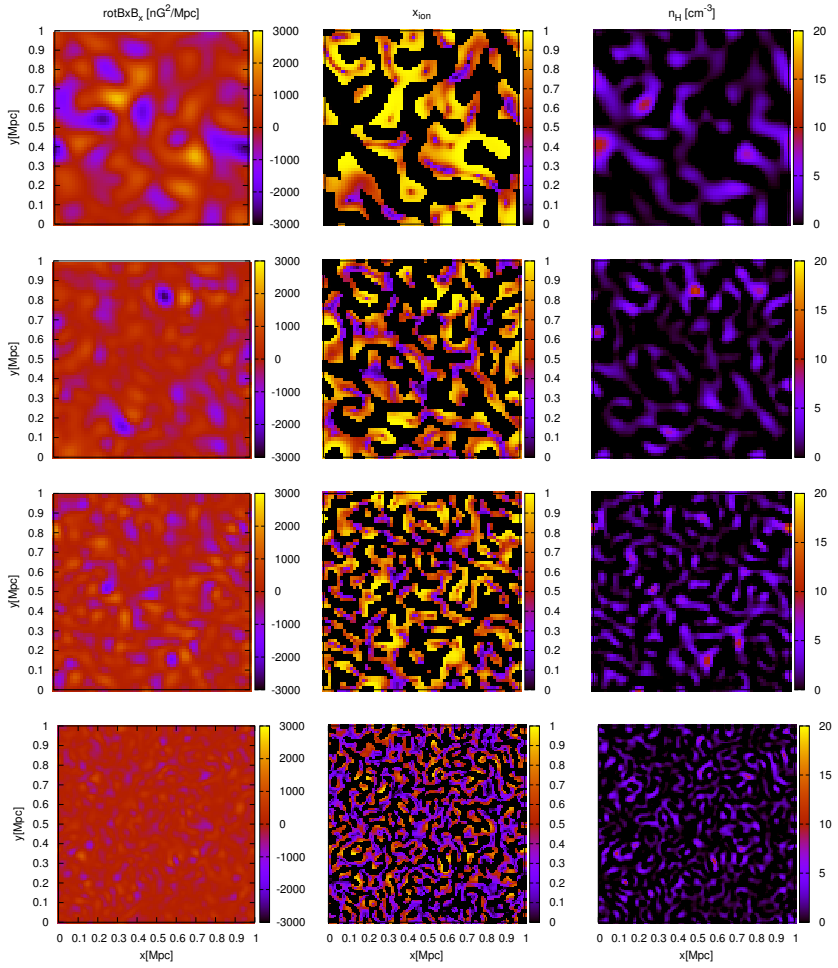

Figure 4.2: Two dimensional illustration of $(\boldsymbol{\nabla} \times \boldsymbol{B}) \times \boldsymbol{B}_x$ (left column), ionization fraction (middle column) and the IGM number density (right column) in the PMFs models 1–4 from top to bottom at $z = 10.0$. From this figures, negative spatial correlation between $x_{\rm i}$ and $n_{\rm H}$ is apparent. It is also visible that the PMFs with smaller values of B_λ and n_B generate more homogeneous structure of the Lorentz force and the gas density distributions.

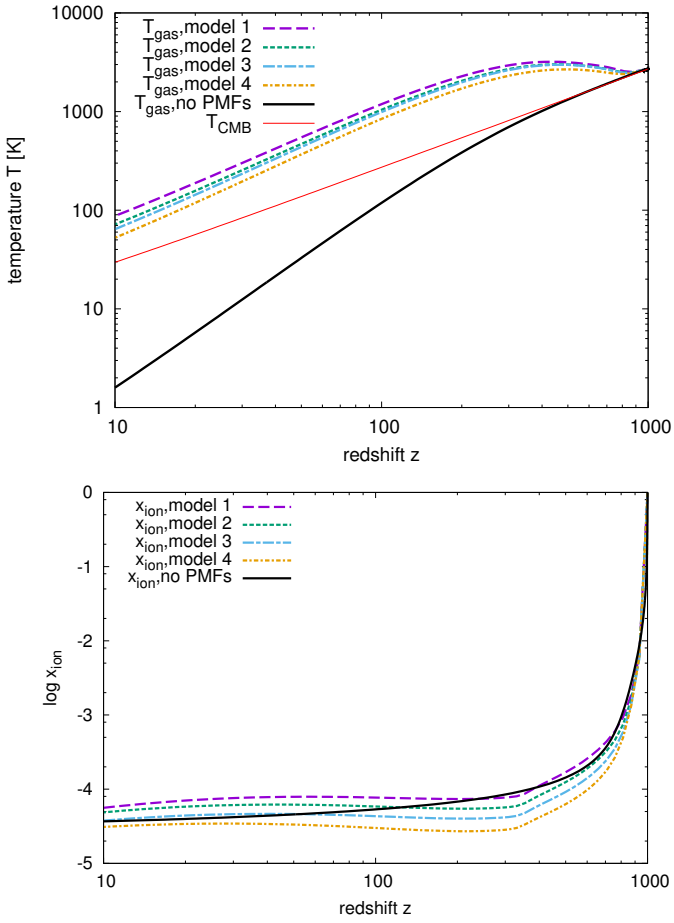

Figure 4.3: Time evolutions of the gas temperature (top) and ionization fraction (bottom), which are averaged per unit mass with and without the PMFs. The black solid lines are time evolutions without the PMFs, and in the top panel, the CMB temperature is also shown with the red solid line. We plot values for different models of the PMFs with dashed, dotted, long-dash-dotted, and short-dash-dotted lines. If the PMFs exist, the gas temperature is always larger than that without the PMFs due to the ambipolar diffusion. On the other hand, the values of the ionization fraction with PMFs tend to be smaller than that without PMFs at high redshifts, and start to increase after $z \sim 300$.

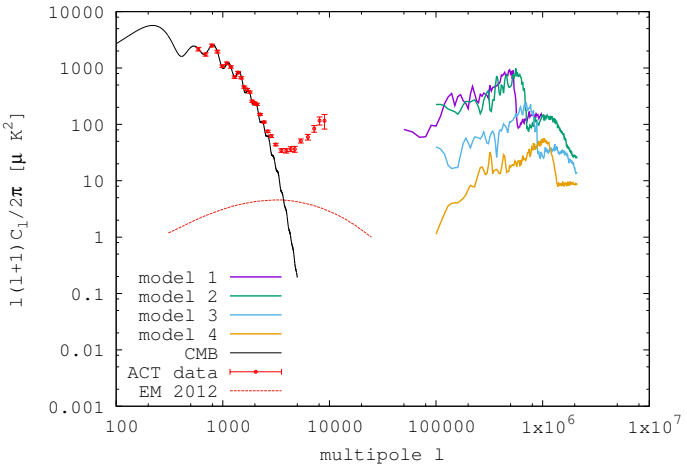

Figure 4.4: Angular power spectra of the tSZ effect induced by the PMFs, obtained by integrating Eq.(4.21) from $z = 1000$ to $z = 10$, for the four models listed in Table 4.3. We also plot the primary CMB angular power spectrum with the black solid line and the observational data with Atacama Cosmology Telescope (ACT) [135] with the red points and error bars. Clearly, the present observational data cannot constrain the PMF models 1–4 because the angular resolution is not enough.

Chapter 5

New constraint from 21-cm global signal

In this chapter, we focus on the 21-cm global signal observation as a cosmological probe to constrain the PMFs. At first, in section 5.1, we describe the physics around the 21-cm line radiation and cosmological signature in its global signal, which is the all-sky averaged value. And then, we review the observation of the 21-cm global signal recently reported by Experiment to Detect the Global Epoch of Reionization Signature (EDGES) in section 5.2. Finally, we investigate the constraint on the PMFs from the EDGES observation in section 5.3 and 5.4.

5.1 21-cm global signal

21-cm line is an electromagnetic wave emitted by transition of two states of a neutral hydrogen atom due to its hyperfine structure. Its wavelength is about 21 cm, and therefore it is called 21-cm line. The intensity of 21-cm line depends on the physical state of the atomic hydrogen such as the number density, the temperature, and the ionization fraction. Thus the observation of redshifted 21-cm line can open a new window in the observational cosmology. The observable of the 21-cm line global signal, which is all-sky averaged intensity, is given by the differential brightness temperature as

$$\delta T_{\rm b}(z) \simeq 27 x_{\rm HI}(z) \left[1 - \frac{T_\gamma(z)}{T_{\rm spin}(z)}\right] \times \left(\frac{\Omega_{\rm b}h^2}{0.02}\right) \left(\frac{0.15}{\Omega_{\rm m}h^2}\right)^{1/2} \left(\frac{1+z}{10}\right)^{1/2} \quad [\rm mK] \ , \tag{5.1}$$

where $x_{\rm HI}$ is the neutral fraction of hydrogen, T_γ is the CMB temperature and $T_{\rm spin}$ is the spin temperature [137]. The spin temperature is defined by the population ratio of the hyperfine levels in a neutral hydrogen as

$$\frac{n_1}{n_0} = \frac{g_1}{g_0} \exp\left(-\frac{\Delta T_{10}}{T_{\rm spin}}\right) \ . \tag{5.2}$$

Here, n_1 and n_0 are number densities in the excited state and bound state of the hyperfine structure, and g_1 and g_0 are their statistical weights, respectively.

When the spin temperature is the same as the CMB one, the 21-cm signal vanishes as shown in Eq. (5.1). In the cosmological context, there are two processes to make the spin temperature deviate from the CMB one. One is the collisional interaction and the other is the interaction with Ly-α flux field [138, 139]. They can couple the hyperfine structure with the IGM gas temperature. Besides the CMB interaction (the 21-cm photon emission and absorption), these processes control the evolution of the spin temperature. In literature [140], the spin temperature evolves between the values of the CMB and the IGM gas temperatures as

$$T_{\rm spin}^{-1} = \frac{T_\gamma^{-1} + x_\alpha T_\alpha^{-1} + x_c T_{\rm K}^{-1}}{1 + x_\alpha + x_c} \tag{5.3}$$

Here, T_α is the color temperature of the background Ly-α photons, and it is considered to be coupled with the kinetic gas temperature $T_{\rm K}$ because the Ly-α photons repeatedly experience the resonant scattering with the hydrogen atoms. Also, x_α and x_c are coupling coefficients for Ly-α interaction and collisional interaction, respectively. Although many effects have been considered with the numerical and analytical calculations, history of the spin temperature has ambiguity of baryon physics.

Time evolution of the spin temperature in the standard picture is shown in Fig. 5.1. In Fig. 5.1, the spin temperature evolution can be divided into four regimes. First, after the decoupling of the gas temperature from the CMB one around $z \sim 200$, the spin temperature follows the gas temperature through the collisional coupling as $T_{\rm K} \simeq T_{\rm spin} < T_\gamma$. Then at the second stage, the spin temperature approaches to the CMB one because the collisional interaction becomes weak due to the cosmic expansion as $T_{\rm K} < T_{\rm spin} \simeq T_\gamma$. In the third regime, the first luminous objects play important roles. They can produce the strong Ly-α field and the Ly-α interaction becomes effective. So far the gas temperature evolves adiabatically after the decoupling from the CMB one and the gas is cooler than the CMB again, as

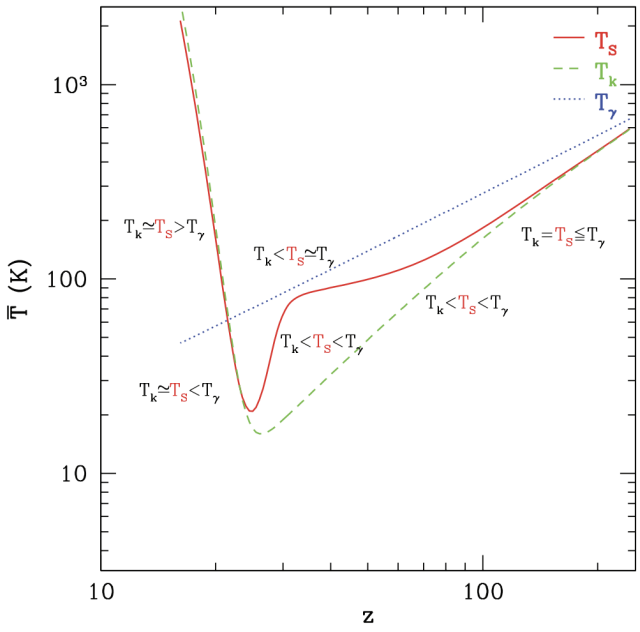

Figure 5.1: A typical spin temperature evolution from semi-numerical calculation [141].

$T_{\rm K} \simeq T_{\rm spin} < T_\gamma$. Accordingly the spin temperature also gets lower than the CMB one. Eq. (5.1) tells us that the global 21-cm signal becomes negative in this regime. In other words, the signals are observed as the absorption trough. After that, as the star and galaxy formation becomes active, a lot of UV photons are produced at this regime. They start to ionize and heat up the gas. Quickly the gas temperature increases and surpasses the CMB temperature. The spin temperature also becomes higher than the CMB and the signal is measured as emission. Gradually the IGM gas is ionized and, finally, the ionization of the IGM is completed. At this point the global 21-cm signal totally vanishes again.

5.2 EDGES observation

Recently, Bowman et al. [142] has reported the detection of the strong radio absorption signal around 78 MHz with the Experiment to Detect the Global Epoch of Reionization Signature (EDGES) as shown in Fig. 5.2. This signal can be considered as the redshifted 21-cm line as $15 \lesssim z \lesssim 20$, and observing the absorption signal implies that the neutral hydrogen hyperfine structure coupled well with the gas temperature through Ly-α field from the first generation stars, and the IGM gas was cooler than the CMB photons around these redshifts. Therefore, the EDGES result can be interpreted as a constraint on a cosmological heating source. Note that the EDGES result is difficult to be explained by the standard scenario: the amplitude of the absorption trough is almost twice as large as the maximal value expected in the standard cosmology. However, instead of giving the explanation on this anomaly, several authors have already applied the EDGES result to constrain some models: the Hawking evaporation of small Primordial Black Holes (PBHs) [143], the emission from the accretion disks around large PBHs [144], the decaying [143, 145] or annihilating dark matter [146,147], warm dark matter [148], primordial power spectrum [149] and so on. In the next section, we show how the PMFs affect the evolution of the IGM gas temperature.

Now the measurement of cosmological 21-cm line signatures is also expected to be a useful tool to constrain the PMFs. The 21-cm line signal depends on the physical states of neutral hydrogen gas such as its number density, its temperature and so on. The PMFs can provide the effect on them through the magnetohydrodynamic (MHD) effects [119]. Ref. [151] has pointed out that the measurements of 21-cm fluctuations by future radio interferometer telescopes can provide a strong constraint on the PMFs

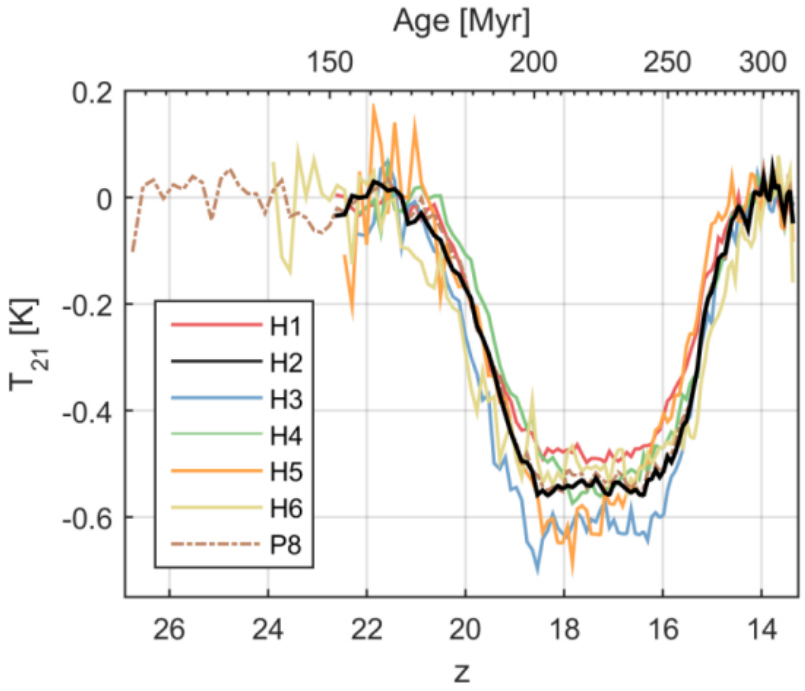

Figure 5.2: Best-fit 21 cm absorption profiles from the EDGES observation against redshift and age of the Universe. Different lines represent different hardware configurations for their data analyses, and the thick black line is one with the highest signal-to-noise ratio among them. This figure is from Ref. [142].

and has stimulated further detailed studies [152, 153].

In this work, we study the implication of the EDGES result to the PMFs and derive a constraint on them. The PMFs work as extra cosmological heating sources through the so-called ambipolar diffusion, in particular, in the late universe. Several authors have already pointed out that the measurement of the global 21-cm signal can put the constraint on the PMFs [154, 155]. Following these works, we evaluate the global thermal history with the PMFs and obtain a constraint on the amplitude and the scale dependence of the PMFs.

5.3 Impact of the PMFs on the gas temperature

After the recombination epoch, the magnetic fields dissipate their energy and heat the IGM gas through two processes [119]. One is the decaying turbulence and the other is the ambipolar diffusion. According to Ref. [119], it has been shown that, while the first one is active around the recombination epoch, the latter becomes effective at the late universe ($z < 500$). The evolution of the IGM gas temperature $T_{\rm K}$ with the above heating effects from the PMFs is given by

$$\frac{dT_{\rm K}}{dt} = -2HT_{\rm K} + \frac{x_e}{1+x_e}\frac{8\rho_\gamma\sigma_{\rm T}}{3m_e c}(T_\gamma - T_{\rm K}) + \frac{2}{3k_{\rm B}n_{\rm b}}(\dot{Q}_{\rm AD} + \dot{Q}_{\rm DT}) \ , \quad (5.4)$$

where H, x_e, ρ_γ, m_e, c, $k_{\rm B}$ and $n_{\rm b}$ is the Hubble parameter, the ionization fraction of the baryon gas, the energy density of CMB photons, the rest mass of an electron, the speed of light, the Boltzmann constant, and the number density of the baryon gas, respectively. $\dot{Q}_{\rm AD}$ and $\dot{Q}_{\rm DT}$ in the right hand side represent the global heating rate due to the ambipolar diffusion (AD) and the decaying turbulence (DT), respectively. These two heating rates are written as [119]

$$\dot{Q}_{\rm AD} = \frac{|(\nabla\times\boldsymbol{B})\times\boldsymbol{B}|^2}{16\pi^2\xi\rho_{\rm b}^2}\frac{1-x_e}{x_e} \ , \quad (5.5)$$

$$\dot{Q}_{\rm DT} = \frac{3w_B}{2}H\frac{|\boldsymbol{B}|^2}{8\pi}a^4\frac{[\ln(1+t_{\rm d}/t_{\rm rec})]^{w_B}}{[\ln(1+t_{\rm d}/t_{\rm rec})+\ln(t/t_{\rm rec})]^{1+w_B}} \ , \quad (5.6)$$

with the time-dependence of the decaying turbulence $w_B \equiv 2(n_B+3)/(n_B+5)$, the mass density of the baryon gas $\rho_{\rm b}$, the physical time-scale for the decaying turbulence $t_{\rm d}$ and the drag coefficient $\xi = 1.9\times10^{14}\ (T_{\rm K}/1\ {\rm K})^{0.375}\ {\rm cm^3 g^{-1} s^{-1}}$ as referred in [156]. Here, since we assume a blue spectrum of the PMFs,

$n_{\rm B} > -3$, we can take $t_{\rm d} = (k_{\rm cut} V_{\rm A})^{-1}$ as the Alfvén time scale at the cut-off scale of the PMFs, as referred in [119].

We can calculate the absolute value of the Lorentz force and the magnetic energy in Eqs. (5.5) and (5.6) with the PMF model parameters, B_n and n_B as

$$|(\nabla \times \boldsymbol{B}) \times \boldsymbol{B}|^2 = \int \frac{d^3k_1}{(2\pi)^3} \int \frac{d^3k_2}{(2\pi)^3}\, k_1^2 P_B(k_1) P_B(k_2)\; f^{2n_B+8}(t)(1+z)^{10}\ , \tag{5.7}$$

$$|\boldsymbol{B}|^2 = \int \frac{d^3k}{(2\pi)^3}\, P_B(k)\; f^{n_B+3}(t)(1+z)^4\ . \tag{5.8}$$

Here, $f(t)$ is an evolutionary function of the cut-off wave-number as $k_{\rm cut}(t) = k_{\rm cut,rec} f(t)$. One can remind that $k_{\rm cut,rec}$ is given by Eq. (2.30). As described in Chapter 2, the PMFs evolve adiabatically as $\boldsymbol{B}(\boldsymbol{x}, t) \propto 1/a^2(t)$ at high redshifts. However, when considering the energy dissipation of the PMFs to the intergalactic medium (IGM) gas, which is introduced here, the PMF energy can decrease by a few orders during the Dark Ages. Since the dissipation of the PMFs is effective on smaller scales, the dissipation could evolve the cut-off scales. In this study, we obtain the evolution of $f(t)$ based on the energy conservation law of PMFs including the energy dissipation given in Eqs. (5.5) and (5.6),

$$\frac{d}{dt}\left(\frac{|\boldsymbol{B}|^2}{8\pi}\right) = -4H\frac{|\boldsymbol{B}|^2}{8\pi} - \dot{Q}_{\rm AD} - \dot{Q}_{\rm DT}\ . \tag{5.9}$$

Rewriting this equations in terms of the PMF power spectrum with the cut-off scales, we can obtain the time evolution of $f(t)$.

In this study, we neglect two effects on the thermal evolution of the IGM gas included in the previous work [156]. First, we do not take into account any radiative cooling effects, such as collisional excitation and ionization, recombination, and bremsstrahlung. We have confirmed these terms are negligible for the PMF model parameters of our interest. The other assumption here is that there are no astrophysical objects. We mention this point in Chapter 6.

In order to solve Eq. (5.4), we also need to follow the evolution of the

ionization fraction,

$$\frac{dx_e}{dt} = \gamma_e n_{\rm b} x_e + \frac{1 + K_\alpha \Lambda n_{\rm b}(1 - x_e)}{1 + K_\alpha(\Lambda + \beta_e) n_{\rm b}(1 - x_e)} \times \left[-\alpha_e n_{\rm b} x_e^2 + \beta_e (1 - x_e) \exp\left(-\frac{3E_{\rm ion}}{4k_{\rm B}T_\gamma} \right) \right] , \tag{5.10}$$

where K_α, Λ, α_e, β_e and γ_e are the parameters for the ionization and the recombination processes. For these parameters, we adopt the functions in Refs. [131] and [130] with the modifications suggested in Ref. [120]. In Eqs. (5.4) and (5.10), we neglect the primordial helium and the heavier elements for simplicity.

Now, assuming the power spectrum of the PMFs, we solve Eqs. (5.4), (5.10) and (5.9) simultaneously, and we can uniquely obtain the evolution of $T_{\rm K}$, x_e, and $f(t)$ for a given PMF model with (n_B, B_n).

5.4 Results

Figure 5.3 shows the gas temperature evolution $T_{\rm K}$ for different B_n with the nearly scale-invariant PMFs ($n_B = -2.9$). Even below the nano Gauss PMFs, kinetic gas temperature is strongly affected by the PMFs. In this case, the gas temperature starts to be well deviated from the one in the case without the PMFs ($B_n = 0$ nG) around $z \sim 100 - 300$, depending on the normalized PMF strength B_n.

We have confirmed that the ambipolar diffusion is the dominant contribution to the heating mechanisms of the IGM at the redshifts of our interest. Then, the redshift dependence of the PMF heating rate due to the ambipolar diffusion can be described as

$$\begin{aligned} \dot{Q}_{\rm AD} &= \frac{1}{16\pi^2 \xi x_e} \frac{\langle |(\nabla \times \boldsymbol{B}) \times \boldsymbol{B}|^2 \rangle (1+z)^{10}}{\rho_{\rm b,0}^2 (1+z)^6} \\ &= \frac{(2\pi)^{2(n_B+2)} B_n^4 k_n^2}{\xi \rho_{\rm b,0}^2 x_e (n_B+3)(n_B+5) \Gamma^2\left(\frac{n_B+3}{2}\right)} \left(\frac{k_{\rm cut}}{k_n} \right)^{2(n_B+4)} (1+z)^4 , \end{aligned} \tag{5.11}$$

except for the redshift dependence of the ionization fraction x_e. Therefore the redshift dependence of the PMF heating term in Eq. (5.5) follows as $2\dot{Q}_{\rm AD}/3k_{\rm B}n_{\rm b} \propto (1+z)$. On the other hand, the dominant cooling term in the right hand side of Eq. (5.4) for $z \ll 200$ is the first one, and $-2HT_{\rm K} \propto$

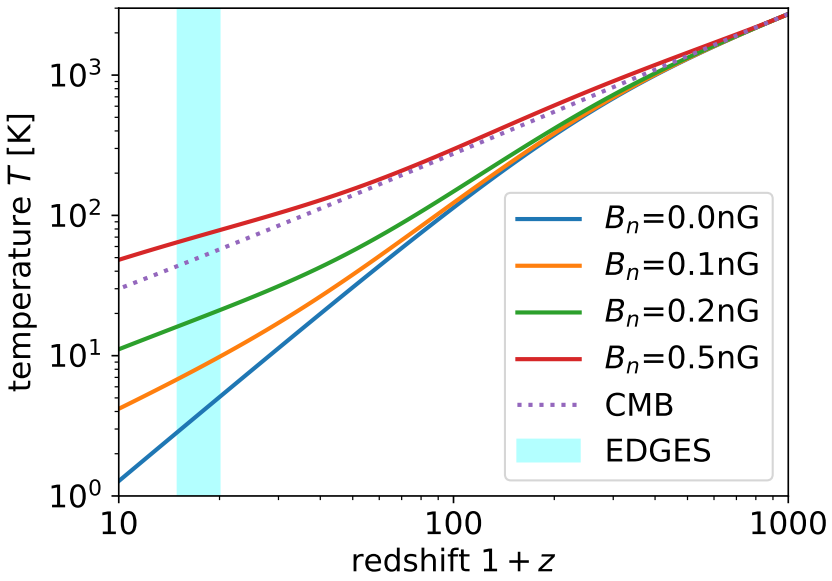

Figure 5.3: The gas temperature evolutions with the PMFs. The dotted line is the CMB temperature, and solid lines are the gas temperature for the cases with $B_n = 0.0, 0.1, 0.2, 0.5$ nG, respectively. In this figure, n_B is fixed to -2.9 for these lines. The blue shaded region represents the redshift range $15 \lesssim z \lesssim 20$ corresponding to the strong absorption signal reported by EDGES.

$(1+z)^{3.5}$, which decreases faster than the heating term due to the ambipolar diffusion. Therefore as we take larger values of B_n, the heating of the IGM gas due to the ambipolar diffusion becomes more effective and dominates the cooling terms at higher redshifts. After the IGM is heated well and the magnetic energy is significantly dissipated, the values for the heating source terms in Eq. (5.5) start to decrease. As a result, the kinetic gas temperature $T_{\rm K}$ starts to deviate from the adiabatic evolution ($B_n = 0$ nG) at first, and the IGM gas is getting cooler slowly after the saturation. We find that the larger value of B_n makes the earlier and stronger heating, and the value of n_B determines the duration of the PMF heating.

As we explained in section 5.2, the EDGES experiment has reported the detection of the global 21-cm absorption signal in the redshifts range of

$15 \lesssim z \lesssim 20$ [157]. In order to compare this observational signature to our results, we highlight these redshift regions with the blue shade in Fig. 5.3. Because the global signal is detected as an absorption, the spin temperature must have been cooler than background radiation temperature, that is $T_{\rm K} \sim T_{\rm spin} < T_\gamma$. Therefore, we can exclude a PMF parameter region (n_B, B_n) which gives $T_{\rm K} > T_\gamma$ at $z_{\rm abs}$. Based on the EDGES reported detection, we set $z_{\rm abs} = 17$ which is the central redshift of the absorption signal in the EDGES experiment. Calculating the evolution of the gas temperature for different B_n with some given spectral indices of the PMFs n_B, we get a novel constraint on the PMFs from the condition $T_{\rm K} < T_\gamma$ at $z_{\rm abs} = 17$. The obtained constraints are $B_n \lesssim 1.2 \times 10^{-1}$ nG for $n_B = -2.9$, $B_n \lesssim 6.3 \times 10^{-3}$ nG for $n_B = -2.0$, and $B_n \lesssim 2.0 \times 10^{-4}$ nG for $n_B = -1.0$. We can fit our new constraint in a linear relation between B_n and n_B as

$$\log\left(\frac{B_n}{1\ {\rm nG}}\right) \lesssim -\frac{(3n_B + 10)}{2} \quad \text{for } -3.0 < n_B < -1.0. \tag{5.12}$$

We plot our PMF constraint on the (n_B, B_n) plane in Fig. 5.4 with a solid line. For comparison, we also show the constraint from [82] and the one from the magnetic reheating before the recombination [84] in the dotted and dashed lines, respectively. In the range of $-3.0 < n_B < -2.0$, the EDGES experiment could constrain the PMF amplitude most tightly.

Finally, by varying $z_{\rm abs}$ from 15 to 20, we have investigated the dependence of the PMF constraint on $z_{\rm abs}$. We have found out that the resultant upper limit differs less than 10 per cent for different $z_{\rm abs}$ between 15 and 20. We can conclude that the dependence on $z_{\rm abs}$ is very weak.

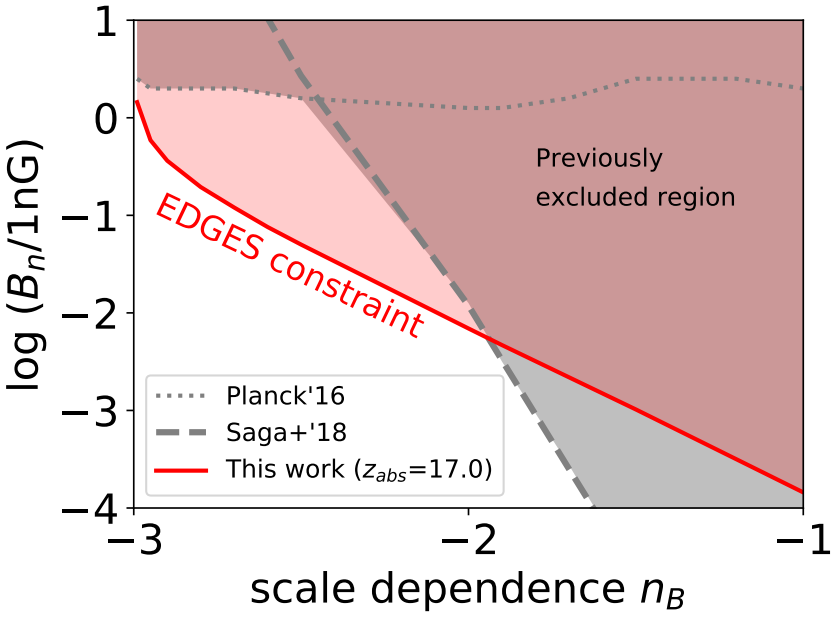

Figure 5.4: The upper limit of the PMFs parameters obtained by the recent observation of 21-cm line absorption by EDGES experiment (solid). The gray shaded region is the excluded region by previous works; [82] in the dotted line and [84] in the dashed line.

Chapter 6

Conclusion

First, we revisited the impact of the PMFs on the primary CMB anisotropies in Chapter 3. The stress-energy tensor of the PMFs induces the metric perturbation besides the primordial curvature perturbation, and the Lorentz force acts on the motion of primordial baryon-photon plasma. To obtain the CMB anisotropy angular power spectra with the PMFs, we have performed a numerical calculation to solve the Einstein-Boltzmann equation system including the above two effects of the PMFs. The PMFs can source the scalar-, vector-, and tensor-type perturbations, and the contribution of the vector-type perturbation is dominant for small angular scales as $\ell \gtrsim 4000$. Since the vector-type CMB anisotropies are caused by the Doppler effect, we investigated the evolution of the baryon velocity perturbation including the Lorentz force of the PMFs. In particular, we have analytically solved the Euler equation below the photon mean-free-path scale for the first time. The derived baryon velocity perturbation on such small scales induces the dominant CMB anisotropies on $\ell \gtrsim 4000$, depending on the spectral indices of the PMFs. Then we also provided the constraint on the PMFs from the CMB temperature and polarization anisotropies observed by the latest Planck and SPT data. As a result, the high-resolution measurement of the CMB anisotropies with SPT favors the nearly scale-invariant PMFs. Finally, we have obtained the constraint on the PMFs as $B_{1\mathrm{Mpc}} < 1.52$ nG and $n_B < -1.14$ for 95 % C.L. with the Planck 2015 and SPT 2015/2017 bandpowers. Our analysis improves the PMF constraint compared with the Planck 2015 constraint, which is $B_{1\mathrm{Mpc}} < 4.4$ nG. We have found that the cosmological parameter estimation can be biased when including the PMF parameter and SPT data. The PMF induced perturbation with the small spectral index n_B enhances the low-ℓ polarization anisotropies, and this

results in the smaller Thomson optical depth τ and the primordial scalar power spectrum amplitude A_s. While the high-resolution CMB anisotropies measured by SPT as $\ell \leq 8000$ provide a tighter constraint on the PMFs, there arises the degeneracy between the PMF and foreground parameters on such small scales. Subtracting the foreground is important not only to improve the constraint on the PMFs but also to understand tSZ clusters [99], the CMB gravitational lensing [158], and the reionization process with the kSZ effect [159]. In principle, the multi-frequency observations might help to remove the CMB foreground and improve our constraint.

Second, in Chapter 4, we have investigated the secondary CMB temperature anisotropies caused by the tSZ effect in the IGM with the PMFs. Here we have taken into account two effects of PMFs on the IGM gas; the generation of the IGM density fluctuations by the Lorentz force, and the heating of the IGM through the ambipolar diffusion. The spatially inhomogeneous PMFs can induce the fluctuations of the density, temperature and ionization fraction in the IGM through these effects. These fluctuated IGM gas induce the anisotropy of y-type distortions of the CMB photons via the tSZ effect after the recombination epoch, which can be observed as the CMB temperature anisotropy. We estimated the CMB angular power spectrum due to the tSZ effect, assuming the PMF statistical properties, i.e., the amplitude of the power spectrum B_n and the spectral index n_B. To evaluate the tSZ angular power spectrum, we solved the non-linear evolutionary equations for the IGM baryon gas in Dark Ages with the realization of random Gaussian PMFs. This is the first attempt to investigate the effects of PMFs on the spatial distributions of the IGM gas properties consistently. Our simulations for different PMF models revealed that the characteristic scales of the spatial distributions correspond to the cut-off scales of the PMFs. Our results indicate that the heating rate of the IGM gas per unit mass is small in over-dense regions, and therefore the IGM temperature is not effectively heated. The ionization fraction in such regions remains small because the recombination rate increase due to the high density. On the other hand, the IGM temperature and ionization fraction can be still high even in low redshifts as $T_{\rm gas} \sim 20000$ K and $x_{\rm i} \sim 1$ when $10 \lesssim z \lesssim 300$ in the low density regions. Thus, there are strong anti-correlations between the IGM density and temperature, and also between density and ionization fraction. From the results of our simulations, we have calculated the tSZ angular power spectrum due to the IGM with PMFs. We have found that since high density regions are almost neutral, their contributions to the tSZ power spectrum are almost negligible. Therefore the SZ measurement can probe mainly lower density regions heated by the PMFs. The tSZ angular

power spectrum has a peak around the cut-off scale of the PMFs ($\ell \sim 10^6$ for sub-nG PMFs) and its amplitude depends on the PMF strength at the cutoff scale. On such small scales, the tSZ effect in galaxy clusters and the kSZ effect due to the patchy reionization can produce the CMB temperature anisotropies. However these signals have the peaks around $\ell \lesssim 10^4$ and decay on high ℓ modes. On the other hand, the tSZ angular power spectrum even for 0.1 nano Gauss PMFs keeps increasing up to $\ell \sim 10^6$. In this work, we have used the linearized equation to calculate the density evolution of the IGM. It is known that the density fluctuations generated by the PMFs have the blue spectrum. Therefore, in our simulations, there are many regions where the IGM density contrast is greater than unity and the linearized equation is no longer valid there. However, as mentioned above, such high density regions have significantly small ionization fraction and their contributions to the Compton y-parameter are expected to be negligibly small. That is, the existence of much higher density contrast than unity does not make us overestimate the tSZ angular power spectrum. In low density regions, we set the bound of the density contrast, $\delta_{\rm b} > -0.9$ to avoid the negative density. Imposing this bound, we intend to take into account approximately the nonlinear effect of the structure formation in a low density region, i.e., a void formation. The density evolution is determined by the local strength of the Lorentz force in our simulation based on the linear density perturbation theory. However, the formation of voids also depends on the environmental condition. Therefore, it is required to include the nonlinear effect of the structure formation to evaluate the tSZ angular power spectrum properly. Besides, we only consider the cosmological expansion in the PMF evolution. Even in low ionization fraction, PMFs could be frozen in the IGM and the density evolution gives the effect on the PMF evolution. This PMF evolution can affect the thermal history of the IGM, in particular, in high density regions and may enhance the tSZ angular power spectrum. To improve these simplified treatments, the detailed MHD simulation of cosmological structure formation with PMFs is required. Furthermore, such a simulation allows us to investigate the PMF effect on the collapse condition [160] and the enhancement of the tSZ angular power spectrum due to galaxy clusters [74,161]. We have shown that the PMFs can generate tSZ signal on small scales after the recombination epoch. Therefore it is worth mentioning about the possibility to provide constraints on the PMFs from small-scale CMB observations. In the current observation status, the foreground emissions dominate on small scales where the tSZ signal from the PMFs arises, and it is difficult to remove the foreground. In addition to the tSZ signal studied in this work, the existence of PMFs can

create non-negligible small-scale CMB anisotropy before the recombination epoch through the Doppler effect due to the velocity perturbations induced by the PMFs [162, 163]. Therefore, in order to obtain constraints on the PMFs, it is required to precisely investigate the CMB anisotropies on small scales including all of these contributions. However, it is beyond the scope of this paper and we address this issue in the future.

Third, we applied the heating effects of the IGM baryon gas from the PMFs to 21-cm line global signal in Chapter 5. 21-cm line intensity depends on the temperature difference between baryons and CMB photons. When the cosmic baryon gas is cooler than the CMB photons, the 21-cm global signal can be measured as an absorption signal. The EDGES experiment has reported the 21-cm absorption signals in redshifts between $15 \lesssim z \lesssim 20$. Therefore, this result suggests that the IGM gas is cooler than the CMB during these periods, and provides a constraint on the PMFs as a heating source of the IGM gas. We numerically evaluated the thermal evolution of the IGM gas with the PMFs via decaying turbulence and ambipolar diffusion. By requiring $T_{\rm K} < T_\gamma$ at $z_{\rm abs} = 17.0$ as the center redshift of the EDGES absorption profile, we obtained a stringent upper limit on the PMF strength roughly about $B_n \lesssim 0.1$ nG. We also found that the PMF constraint is not so changed in case the absorption redshift is deviated from $z_{\rm abs} = 17.0$. Finally, we briefly discuss the impact of the astrophysical objects on the PMF constraint. Of course they can significantly heat up and ionise the IGM gas, and the constraint from the 21-cm absorption signal might become tighter if we include such astrophysical processes (e.g., the star formation and the AGN activity). On the other hand, some previous works have pointed out that the condition of the astrophysical object formation is also affected by the PMFs [126, 160]. In order to calculate the global 21-cm signal history with these effects, we should solve the fully non-linear MHD equations and the realistic astrophysical processes [153, 164]. We leave these points to future work.

Bibliography

[1] T. Akahori, H. Nakanishi, Y. Sofue, Y. Fujita, K. Ichiki, S. Ideguchi, O. Kameya, T. Kudoh, Y. Kudoh, M. Machida, Y. Miyashita, H. Ohno, T. Ozawa, K. Takahashi, M. Takizawa, and D. G. Yamazaki. Cosmic magnetism in centimeter- and meter-wavelength radio astronomy. PASJ, December 2017.

[2] Rainer Beck and Richard Wielebinski. *Magnetic Fields in Galaxies*, volume 5, page 641. 2013.

[3] V. L. Ginzburg and S. I. Syrovatskii. Cosmic Magnetobremsstrahlung (synchrotron Radiation). ARA&A, 3:297, 1965.

[4] V. L. Ginzburg and S. I. Syrovatskii. Developments in the Theory of Synchrotron Radiation and its Reabsorption. ARA&A, 7:375, 1969.

[5] R. Wielebinski. Magnetic Fields in the Milky Way, Derived from Radio Continuum Observations and Faraday Rotation Studies. In R. Wielebinski and R. Beck, editors, *Cosmic Magnetic Fields*, volume 664 of *Lecture Notes in Physics, Berlin Springer Verlag*, page 89, 2005.

[6] J. C. Brown. The Magnetic Field of the Milky Way Galaxy. In R. Kothes, T. L. Landecker, and A. G. Willis, editors, *The Dynamic Interstellar Medium: A Celebration of the Canadian Galactic Plane Survey*, volume 438 of *Astronomical Society of the Pacific Conference Series*, page 216, December 2010.

[7] M. Haverkorn. Magnetic Fields in the Milky Way. In A. Lazarian, E. M. de Gouveia Dal Pino, and C. Melioli, editors, *Magnetic Fields in Diffuse Media*, volume 407 of *Astrophysics and Space Science Library*, page 483, 2015.

[8] R. Beck and B. M. Gaensler. Observations of magnetic fields in the Milky Way and in nearby galaxies with a Square Kilometre Array. New A Rev., 48:1289–1304, December 2004.

[9] J. Han. Magnetic fields in our Milky Way Galaxy and nearby galaxies. In A. G. Kosovichev, E. de Gouveia Dal Pino, and Y. Yan, editors, *Solar and Astrophysical Dynamos and Magnetic Activity*, volume 294 of *IAU Symposium*, pages 213–224, July 2013.

[10] C. L. Carilli and G. B. Taylor. Cluster Magnetic Fields. ARA&A, 40:319–348, 2002.

[11] R. Beck. Galactic and Extragalactic Magnetic Fields. In F. A. Aharonian, W. Hofmann, and F. Rieger, editors, *American Institute of Physics Conference Series*, volume 1085 of *American Institute of Physics Conference Series*, pages 83–96, December 2008.

[12] R. Beck. Cosmic Magnetic Fields: Observations and Prospects. In F. A. Aharonian, W. Hofmann, and F. M. Rieger, editors, *American Institute of Physics Conference Series*, volume 1381 of *American Institute of Physics Conference Series*, pages 117–136, September 2011.

[13] R. Beck. Magnetic fields in spiral galaxies. A&A Rev., 24:4, December 2015.

[14] J. L. Han. Observing Interstellar and Intergalactic Magnetic Fields. ARA&A, 55:111–157, August 2017.

[15] T. E. Clarke, P. P. Kronberg, and H. Böhringer. A New Radio-X-Ray Probe of Galaxy Cluster Magnetic Fields. ApJ, 547:L111–L114, February 2001.

[16] F. Govoni and L. Feretti. Magnetic Fields in Clusters of Galaxies. *International Journal of Modern Physics D*, 13:1549–1594, 2004.

[17] C. Pfrommer and T. A. Enßlin. Estimating galaxy cluster magnetic fields by the classical and hadronic minimum energy criterion. MNRAS, 352:76–90, July 2004.

[18] A. Bonafede, L. Feretti, M. Murgia, F. Govoni, G. Giovannini, and V. Vacca. Galaxy cluster magnetic fields from radio polarized emission. *ArXiv e-prints*, September 2010.

[19] M. Lemoine, G. Sigl, and P. Biermann. Supercluster Magnetic Fields and Anisotropy of Cosmic Rays above 10**(19) eV. *ArXiv Astrophysics e-prints*, March 1999.

[20] J. P. Vallée. Faraday Screen and Reversal of Rotation Measure in the Local Supercluster Plane. AJ, 124:1322–1327, September 2002.

[21] C. Isola and G. Sigl. Large scale magnetic fields and the number of cosmic ray sources above the Greisen-Zatsepin-Kuzmin cutoff. Phys. Rev. D, 66(8):083002, October 2002.

[22] Y. Xu, P. P. Kronberg, S. Habib, and Q. W. Dufton. A Faraday Rotation Search for Magnetic Fields in Large-scale Structure. ApJ, 637:19–26, January 2006.

[23] Shin'ichiro Ando and Alexander Kusenko. Evidence for Gamma-ray Halos Around Active Galactic Nuclei and the First Measurement of Intergalactic Magnetic Fields. ApJ, 722(1):L39–L44, October 2010.

[24] A. Neronov and I. Vovk. Evidence for Strong Extragalactic Magnetic Fields from Fermi Observations of TeV Blazars. *Science*, 328:73, April 2010.

[25] W. Essey, S. Ando, and A. Kusenko. Determination of intergalactic magnetic fields from gamma ray data. *Astroparticle Physics*, 35:135–139, October 2011.

[26] K. Takahashi, M. Mori, K. Ichiki, and S. Inoue. Lower Bounds on Intergalactic Magnetic Fields from Simultaneously Observed GeV-TeV Light Curves of the Blazar Mrk 501. ApJ, 744:L7, January 2012.

[27] K. Takahashi, M. Mori, K. Ichiki, S. Inoue, and H. Takami. Lower Bounds on Magnetic Fields in Intergalactic Voids from Long-term GeV-TeV Light Curves of the Blazar Mrk 421. ApJ, 771:L42, July 2013.

[28] W. Chen, J. H. Buckley, and F. Ferrer. Search for GeV γ -Ray Pair Halos Around Low Redshift Blazars. *Physical Review Letters*, 115(21):211103, November 2015.

[29] H. Tashiro and T. Vachaspati. Parity-odd correlators of diffuse gamma-rays and intergalactic magnetic fields. MNRAS, 448:299–306, March 2015.

[30] R. Plaga. Detecting intergalactic magnetic fields using time delays in pulses of γ-rays. Nature, 374:430–432, March 1995.

[31] F. Tavecchio, G. Ghisellini, L. Foschini, G. Bonnoli, G. Ghirlanda, and P. Coppi. The intergalactic magnetic field constrained by Fermi/Large Area Telescope observations of the TeV blazar 1ES0229+200. MNRAS, 406:L70–L74, July 2010.

[32] F. A. Aharonian, P. S. Coppi, and H. J. Voelk. Very high energy gamma rays from active galactic nuclei: Cascading on the cosmic background radiation fields and the formation of pair halos. ApJ, 423:L5–L8, March 1994.

[33] J. D. Bray and A. M. M. Scaife. An Upper Limit on the Strength of the Extragalactic Magnetic Field from Ultra-high-energy Cosmic-Ray Anisotropy. ApJ, 861(1):3, July 2018.

[34] L. Biermann. Über den Ursprung der Magnetfelder auf Sternen und im interstellaren Raum (miteinem Anhang von A. Schlüter). *Zeitschrift Naturforschung Teil A*, 5:65, 1950.

[35] R. M. Kulsrud, R. Cen, J. P. Ostriker, and D. Ryu. The Protogalactic Origin for Cosmic Magnetic Fields. ApJ, 480:481–491, May 1997.

[36] N. Y. Gnedin, A. Ferrara, and E. G. Zweibel. Generation of the Primordial Magnetic Fields during Cosmological Reionization. ApJ, 539:505–516, August 2000.

[37] H. Hanayama, K. Takahashi, K. Kotake, M. Oguri, K. Ichiki, and H. Ohno. Biermann Mechanism in Primordial Supernova Remnant and Seed Magnetic Fields. ApJ, 633:941–945, November 2005.

[38] H. Xu, B. W. O'Shea, D. C. Collins, M. L. Norman, H. Li, and S. Li. The Biermann Battery in Cosmological MHD Simulations of Population III Star Formation. ApJ, 688:L57, December 2008.

[39] M. Ando, K. Doi, and H. Susa. Generation of Seed Magnetic Field Around First Stars: Effects of Radiation Force. ApJ, 716:1566–1572, June 2010.

[40] J.-B. Durrive and M. Langer. Intergalactic magnetogenesis at Cosmic Dawn by photoionization. MNRAS, 453:345–356, October 2015.

[41] R. E. Pudritz and J. Silk. The origin of magnetic fields and primordial stars in protogalaxies. ApJ, 342:650–659, July 1989.

[42] R. A. Daly and A. Loeb. A possible origin of galactic magnetic fields. ApJ, 364:451–455, December 1990.

[43] H. J. Völk and A. M. Atoyan. Early Starbursts and Magnetic Field Generation in Galaxy Clusters. ApJ, 541:88–94, September 2000.

[44] S. R. Furlanetto and A. Loeb. Intergalactic Magnetic Fields from Quasar Outflows. ApJ, 556:619–634, August 2001.

[45] S. R. Furlanetto and A. Loeb. Intergalactic Magnetic Fields from Quasar Outflows. In M. Gilfanov, R. Sunyeav, and E. Churazov, editors, *Lighthouses of the Universe: The Most Luminous Celestial Objects and Their Use for Cosmology*, page 450, 2002.

[46] H. Li, G. Lapenta, J. M. Finn, S. Li, and S. A. Colgate. Modeling the Large-Scale Structures of Astrophysical Jets in the Magnetically Dominated Limit. ApJ, 643:92–100, May 2006.

[47] Michael S. Turner and Lawrence M. Widrow. Inflation-produced, large-scale magnetic fields. *Phys. Rev. D*, 37:2743–2754, May 1988.

[48] Bharat Ratra. Cosmological "Seed" Magnetic Field from Inflation. ApJ, 391:L1, May 1992.

[49] A. D. Dolgov. Breaking of conformal invariance and electromagnetic field generation in the universe. *Phys. Rev. D*, 48:2499–2501, Sep 1993.

[50] J. Martin and J. Yokoyama. Generation of large scale magnetic fields in single-field inflation. J. Cosmology Astropart. Phys., 1:025, January 2008.

[51] T. Fujita, R. Namba, Y. Tada, N. Takeda, and H. Tashiro. Consistent generation of magnetic fields in axion inflation models. J. Cosmology Astropart. Phys., 5:054, May 2015.

[52] Craig J. Hogan. Magnetohydrodynamic effects of a first-order cosmological phase transition. *Phys. Rev. Lett.*, 51:1488–1491, Oct 1983.

[53] Tanmay Vachaspati. Magnetic fields from cosmological phase transitions. *Physics Letters B*, 265(3-4):258–261, August 1991.

[54] D. Grasso and A. Riotto. On the nature of the magnetic fields generated during the electroweak phase transition. *Physics Letters B*, 418:258–265, February 1998.

[55] M. Gasperini, M. Giovannini, and G. Veneziano. Primordial magnetic fields from string cosmology. *Phys. Rev. Lett.*, 75:3796–3799, Nov 1995.

[56] Massimo Giovannini. Magnetogenesis and the dynamics of internal dimensions. *Phys. Rev. D*, 62:123505, Nov 2000.

[57] K. Ichiki, K. Takahashi, H. Ohno, H. Hanayama, and N. Sugiyama. Cosmological Magnetic Field: A Fossil of Density Perturbations in the Early Universe. *Science*, 311:827–829, February 2006.

[58] Kumar Atmjeet, Isha Pahwa, T. R. Seshadri, and Kandaswamy Subramanian. Cosmological magnetogenesis from extra-dimensional gauss-bonnet gravity. *Phys. Rev. D*, 89:063002, Mar 2014.

[59] K. Subramanian. Magnetic fields in the early Universe. *Astronomische Nachrichten*, 331:110, January 2010.

[60] A. Kandus, K. E. Kunze, and C. G. Tsagas. Primordial magnetogenesis. Phys. Rep., 505:1–58, August 2011.

[61] K. Subramanian. The origin, evolution and signatures of primordial magnetic fields. *Reports on Progress in Physics*, 79(7):076901, July 2016.

[62] Andres Aramburo Garcia, Kyrylo Bondarenko, Alexey Boyarsky, Dylan Nelson, Annalisa Pillepich, and Anastasia Sokolenko. Magnetization of the intergalactic medium in the IllustrisTNG simulations: the importance of extended, outflow-driven bubbles. *arXiv e-prints*, page arXiv:2011.11581, November 2020.

[63] E. N. Parker. Hydromagnetic Dynamo Models. ApJ, 122:293, September 1955.

[64] Axel Brandenburg and Kandaswamy Subramanian. Astrophysical magnetic fields and nonlinear dynamo theory. Phys. Rep., 417(1-4):1–209, October 2005.

[65] M. J. Rees. The origin and cosmogonic implications of seed magnetic fields. QJRAS, 28:197–206, September 1987.

[66] A.-C. Davis, M. Lilley, and O. Törnkvist. Relaxing the bounds on primordial magnetic seed fields. Phys. Rev. D, 60(2):021301, July 1999.

[67] L. L. Kitchatinov and G. Rüdiger. Seed fields for galactic dynamos by the magnetorotational instability. A&A, 424:565–570, September 2004.

[68] R. Durrer and A. Neronov. Cosmological magnetic fields: their generation, evolution and observation. A&A Rev., 21:62, June 2013.

[69] Robi Banerjee and Karsten Jedamzik. Evolution of cosmic magnetic fields: From the very early Universe, to recombination, to the present. Phys. Rev. D, 70(12):123003, December 2004.

[70] C. Fedeli and L. Moscardini. Constraining primordial magnetic fields with future cosmic shear surveys. J. Cosmology Astropart. Phys., 11:055, November 2012.

[71] Kanhaiya L. Pandey and Shiv K. Sethi. Probing Primordial Magnetic Fields Using Lyα Clouds. ApJ, 762(1):15, January 2013.

[72] Tina Kahniashvili, Yurii Maravin, Aravind Natarajan, Nicholas Battaglia, and Alexander G. Tevzadze. Constraining Primordial Magnetic Fields through Large-scale Structure. ApJ, 770(1):47, June 2013.

[73] Kerstin E. Kunze and Eiichiro Komatsu. Constraints on primordial magnetic fields from the optical depth of the cosmic microwave background. J. Cosmology Astropart. Phys., 2015(6):027, Jun 2015.

[74] H. Tashiro and N. Sugiyama. Sunyaev-Zel'dovich power spectrum produced by primordial magnetic fields. MNRAS, 411:1284–1292, February 2011.

[75] Teppei Minoda, Kiyotomo Ichiki, and Hiroyuki Tashiro. Small-scale CMB anisotropies induced by the primordial magnetic fields. *arXiv e-prints*, page arXiv:2012.12542, December 2020.

[76] Teppei Minoda, Kenji Hasegawa, Hiroyuki Tashiro, Kiyotomo Ichiki, and Naoshi Sugiyama. Thermal Sunyaev-Zel'dovich effect in the intergalactic medium with primordial magnetic fields. *Phys. Rev. D*, 96:123525, Dec 2017.

[77] Teppei Minoda, Kenji Hasegawa, Hiroyuki Tashiro, Kiyotomo Ichiki, and Naoshi Sugiyama. Thermal Sunyaev-Zel'dovich Effect in the IGM due to Primordial Magnetic Fields. *Galaxies*, 6(4):143, December 2018.

[78] Teppei Minoda, Hiroyuki Tashiro, and Tomo Takahashi. Insight into primordial magnetic fields from 21-cm line observation with EDGES experiment. MNRAS, 488(2):2001–2005, September 2019.

[79] Planck Collaboration, P. A. R. Ade, N. Aghanim, M. Arnaud, M. Ashdown, J. Aumont, C. Baccigalupi, A. J. Banday, R. B. Barreiro, J. G. Bartlett, and et al. Planck 2015 results. XIII. Cosmological parameters. A&A, 594:A13, September 2016.

[80] A. S. Monin and A. M. Iaglom. *Statistical fluid mechanics: Mechanics of turbulence. Volume 2 /revised and enlarged edition/.* 1975.

[81] L. D. Landau and E. M. Lifshitz. *Statistical physics. Pt.1, Pt.2.* 1980.

[82] Planck Collaboration, P. A. R. Ade, N. Aghanim, M. Arnaud, F. Arroja, M. Ashdown, J. Aumont, C. Baccigalupi, M. Ballardini, A. J. Banday, and et al. Planck 2015 results. XIX. Constraints on primordial magnetic fields. A&A, 594:A19, September 2016.

[83] C. Fedeli and L. Moscardini. Constraining primordial magnetic fields with future cosmic shear surveys. J. Cosmology Astropart. Phys., 11:055, November 2012.

[84] S. Saga, H. Tashiro, and S. Yokoyama. Magnetic reheating. MNRAS, 474:L52–L55, February 2018.

[85] M. Giovannini. Growth rate of matter perturbations as a probe of large-scale magnetism. Phys. Rev. D, 84(6):063010, September 2011.

[86] K. Jedamzik, V. Katalinić, and A. V. Olinto. Damping of cosmic magnetic fields. Phys. Rev. D, 57:3264–3284, March 1998.

[87] K. Subramanian and J. D. Barrow. Magnetohydrodynamics in the early universe and the damping of nonlinear Alfvén waves. Phys. Rev. D, 58(8):083502, October 1998.

[88] Andrew Mack, Tina Kahniashvili, and Arthur Kosowsky. Microwave background signatures of a primordial stochastic magnetic field. Phys. Rev. D, 65(12):123004, June 2002.

[89] A. Friedmann. Über die Krümmung des Raumes. *Zeitschrift fur Physik*, 10:377–386, 1922.

[90] G. Lemaître. Un Univers homogène de masse constante et de rayon croissant rendant compte de la vitesse radiale des nébuleuses extra-galactiques. *Annales de la Société Scientifique de Bruxelles*, 47:49–59, 1927.

[91] E. Hubble. A Relation between Distance and Radial Velocity among Extra-Galactic Nebulae. *Proceedings of the National Academy of Science*, 15:168–173, March 1929.

[92] V. M. Slipher. The radial velocity of the Andromeda Nebula. *Lowell Observatory Bulletin*, 2:56–57, 1913.

[93] R. A. Alpher, H. Bethe, and G. Gamow. The Origin of Chemical Elements. *Physical Review*, 73:803–804, April 1948.

[94] C. Hayashi. Proton-Neutron Concentration Ratio in the Expanding Universe at the Stages preceding the Formation of the Elements. *Progress of Theoretical Physics*, 5:224–235, March 1950.

[95] R. A. Alpher and R. C. Herman. Neutron-Capture Theory of Element Formation in an Expanding Universe. *Physical Review*, 84:60–68, October 1951.

[96] A. A. Penzias and R. W. Wilson. A Measurement of Excess Antenna Temperature at 4080 Mc/s. ApJ, 142:419–421, July 1965.

[97] D. J. Fixsen. The Temperature of the Cosmic Microwave Background. ApJ, 707(2):916–920, December 2009.

[98] L. D. Landau and E. M. Lifshitz. *Quantum mechanics*. 1965.

[99] R. A. Sunyaev and Y. B. Zeldovich. Small-Scale Fluctuations of Relic Radiation. Ap&SS, 7:3–19, April 1970.

[100] P. J. E. Peebles and J. T. Yu. Primeval Adiabatic Perturbation in an Expanding Universe. ApJ, 162:815, December 1970.

[101] J. Silk. Cosmic Black-Body Radiation and Galaxy Formation. ApJ, 151:459, February 1968.

[102] Scott Dodelson. *Modern cosmology*. 2003.

[103] Alex Zucca, Yun Li, and Levon Pogosian. Constraints on primordial magnetic fields from Planck data combined with the South Pole Telescope CMB B -mode polarization measurements. Phys. Rev. D, 95(6):063506, March 2017.

[104] J. W. Henning, J. T. Sayre, C. L. Reichardt, P. A. R. Ade, A. J. Anderson, J. E. Austermann, J. A. Beall, A. N. Bender, B. A. Benson, L. E. Bleem, J. E. Carlstrom, C. L. Chang, H. C. Chiang, H. M. Cho, R. Citron, C. Corbett Moran, T. M. Crawford, A. T. Crites, T. de Haan, M. A. Dobbs, W. Everett, J. Gallicchio, E. M. George, A. Gilbert, N. W. Halverson, N. Harrington, G. C. Hilton, G. P. Holder, W. L. Holzapfel, S. Hoover, Z. Hou, J. D. Hrubes, N. Huang, J. Hubmayr, K. D. Irwin, R. Keisler, L. Knox, A. T. Lee, E. M. Leitch, D. Li, A. Lowitz, A. Manzotti, J. J. McMahon, S. S. Meyer, L. Mocanu, J. Montgomery, A. Nadolski, T. Natoli, J. P. Nibarger, V. Novosad, S. Padin, C. Pryke, J. E. Ruhl, B. R. Saliwanchik, K. K. Schaffer, C. Sievers, G. Smecher, A. A. Stark, K. T. Story, C. Tucker, K. Vanderlinde, T. Veach, J. D. Vieira, G. Wang, N. Whitehorn, W. L. K. Wu, and V. Yefremenko. Measurements of the Temperature and E-mode Polarization of the CMB from 500 Square Degrees of SPTpol Data. ApJ, 852(2):97, Jan 2018.

[105] J. R. Shaw and A. Lewis. Massive neutrinos and magnetic fields in the early universe. Phys. Rev. D, 81(4):043517, February 2010.

[106] R. Durrer. Gauge Invariant Cosmological Perturbation Theory: A General Study and It's Application to the Texture Scenario of Structure Formation. Fund. Cosmic Phys., 3:209–339, January 1994.

[107] James M. Bardeen. Gauge-invariant cosmological perturbations. Phys. Rev. D, 22(8):1882–1905, October 1980.

[108] Wayne Hu and Martin White. CMB anisotropies: Total angular momentum method. Phys. Rev. D, 56(2):596–615, July 1997.

[109] K. Jedamzik, V. Katalinić, and A. V. Olinto. Damping of cosmic magnetic fields. Phys. Rev. D, 57:3264–3284, March 1998.

[110] Antony Lewis, Anthony Challinor, and Anthony Lasenby. Efficient computation of CMB anisotropies in closed FRW models. *Astrophys. J.*, 538:473–476, 2000.

[111] A. Lewis and S. Bridle. Cosmological parameters from CMB and other data: A Monte Carlo approach. Phys. Rev. D, 66(10):103511, November 2002.

[112] Planck Collaboration, P. A. R. Ade, N. Aghanim, M. Arnaud, F. Arroja, M. Ashdown, J. Aumont, C. Baccigalupi, M. Ballardini, A. J. Banday, R. B. Barreiro, N. Bartolo, E. Battaner, K. Benabed, A. Benoît, A. Benoit-Lévy, J. P. Bernard, M. Bersanelli, P. Bielewicz, J. J. Bock, A. Bonaldi, L. Bonavera, J. R. Bond, J. Borrill, F. R. Bouchet, M. Bucher, C. Burigana, R. C. Butler, E. Calabrese, J. F. Cardoso, A. Catalano, A. Chamballu, H. C. Chiang, J. Chluba, P. R. Christensen, S. Church, D. L. Clements, S. Colombi, L. P. L. Colombo, C. Combet, F. Couchot, A. Coulais, B. P. Crill, A. Curto, F. Cuttaia, L. Danese, R. D. Davies, R. J. Davis, P. de Bernardis, A. de Rosa, G. de Zotti, J. Delabrouille, F. X. Désert, J. M. Diego, K. Dolag, H. Dole, S. Donzelli, O. Doré, M. Douspis, A. Ducout, X. Dupac, G. Efstathiou, F. Elsner, T. A. Enßlin, H. K. Eriksen, J. Fergusson, F. Finelli, E. Florido, O. Forni, M. Frailis, A. A. Fraisse, E. Franceschi, A. Frejsel, S. Galeotta, S. Galli, K. Ganga, M. Giard, Y. Giraud-Héraud, E. Gjerløw, J. González-Nuevo, K. M. Górski, S. Gratton, A. Gregorio, A. Gruppuso, J. E. Gudmundsson, F. K. Hansen, D. Hanson, D. L. Harrison, G. Helou, S. Henrot-Versillé, C. Hernández-Monteagudo, D. Herranz, S. R. Hildebrand t, E. Hivon, M. Hobson, W. A. Holmes, A. Hornstrup, W. Hovest, K. M. Huffenberger, G. Hurier, A. H. Jaffe, T. R. Jaffe, W. C. Jones, M. Juvela, E. Keihänen, R. Keskitalo, J. Kim, T. S. Kisner, J. Knoche, M. Kunz, H. Kurki-Suonio, G. Lagache, A. Lähteenmäki, J. M. Lamarre, A. Lasenby, M. Lattanzi, C. R. Lawrence, J. P. Leahy, R. Leonardi, J. Lesgourgues, F. Levrier, M. Liguori, P. B. Lilje, M. Linden-Vørnle, M. López-Caniego, P. M. Lubin, J. F. Macías-Pérez, G. Maggio, D. Maino, N. Mand olesi, A. Mangilli, M. Maris, P. G. Martin, E. Martínez-González, S. Masi, S. Matarrese, P. McGehee, P. R. Meinhold, A. Melchiorri, L. Mendes, A. Mennella, M. Migliaccio, S. Mitra, M. A. Miville-Deschênes, D. Molinari, A. Moneti, L. Montier, G. Morgante, D. Mortlock, A. Moss, D. Munshi, J. A. Murphy, P. Naselsky, F. Nati, P. Natoli, C. B. Netterfield, H. U. Nørgaard-Nielsen, F. Noviello, D. Novikov, I. Novikov, N. Oppermann, C. A. Oxborrow, F. Paci, L. Pagano, F. Pajot, D. Paoletti, F. Pasian, G. Patanchon, O. Perdereau, L. Perotto, F. Perrotta, V. Pettorino, F. Piacentini, M. Piat, E. Pierpaoli, D. Pietrobon, S. Plaszczynski,

E. Pointecouteau, G. Polenta, L. Popa, G. W. Pratt, G. Prézeau, S. Prunet, J. L. Puget, J. P. Rachen, R. Rebolo, M. Reinecke, M. Remazeilles, C. Renault, A. Renzi, I. Ristorcelli, G. Rocha, C. Rosset, M. Rossetti, G. Roudier, J. A. Rubiño-Martín, B. Ruiz-Granados, B. Rusholme, M. Sandri, D. Santos, M. Savelainen, G. Savini, D. Scott, M. D. Seiffert, E. P. S. Shellard, M. Shiraishi, L. D. Spencer, V. Stolyarov, R. Stompor, R. Sudiwala, R. Sunyaev, D. Sutton, A. S. Suur-Uski, J. F. Sygnet, J. A. Tauber, L. Terenzi, L. Toffolatti, M. Tomasi, M. Tristram, M. Tucci, J. Tuovinen, G. Umana, L. Valenziano, J. Valiviita, B. Van Tent, P. Vielva, F. Villa, L. A. Wade, B. D. Wandelt, I. K. Wehus, D. Yvon, A. Zacchei, and A. Zonca. Planck 2015 results. XIX. Constraints on primordial magnetic fields. A&A, 594:A19, September 2016.

[113] R. Keisler, S. Hoover, N. Harrington, J. W. Henning, P. A. R. Ade, K. A. Aird, J. E. Austermann, J. A. Beall, A. N. Bender, B. A. Benson, L. E. Bleem, J. E. Carlstrom, C. L. Chang, H. C. Chiang, H. M. Cho, R. Citron, T. M. Crawford, A. T. Crites, T. de Haan, M. A. Dobbs, W. Everett, J. Gallicchio, J. Gao, E. M. George, A. Gilbert, N. W. Halverson, D. Hanson, G. C. Hilton, G. P. Holder, W. L. Holzapfel, Z. Hou, J. D. Hrubes, N. Huang, J. Hubmayr, K. D. Irwin, L. Knox, A. T. Lee, E. M. Leitch, D. Li, D. Luong-Van, D. P. Marrone, J. J. McMahon, J. Mehl, S. S. Meyer, L. Mocanu, T. Natoli, J. P. Nibarger, V. Novosad, S. Padin, C. Pryke, C. L. Reichardt, J. E. Ruhl, B. R. Saliwanchik, J. T. Sayre, K. K. Schaffer, E. Shirokoff, G. Smecher, A. A. Stark, K. T. Story, C. Tucker, K. Vanderlinde, J. D. Vieira, G. Wang, N. Whitehorn, V. Yefremenko, and O. Zahn. Measurements of Sub-degree B-mode Polarization in the Cosmic Microwave Background from 100 Square Degrees of SPTpol Data. ApJ, 807(2):151, July 2015.

[114] Tina Kahniashvili, Axel Brandenburg, Ruth Durrer, Alexander G. Tevzadze, and Winston Yin. Scale-invariant helical magnetic field evolution and the duration of inflation. J. Cosmology Astropart. Phys., 2017(12):002, December 2017.

[115] Ramkishor Sharma, Kandaswamy Subramanian, and T. R. Seshadri. Generation of helical magnetic field in a viable scenario of inflationary magnetogenesis. Phys. Rev. D, 97(8):083503, April 2018.

[116] Tomohiro Fujita and Ruth Durrer. Scale-invariant helical magnetic fields from inflation. J. Cosmology Astropart. Phys., 2019(9):008, September 2019.

[117] Teerthal Patel, Hiroyuki Tashiro, and Yuko Urakawa. Resonant magnetogenesis from axions. J. Cosmology Astropart. Phys., 2020(1):043, January 2020.

[118] K. Subramanian and J. D. Barrow. Magnetohydrodynamics in the early universe and the damping of nonlinear Alfvén waves. Phys. Rev. D, 58(8):083502, October 1998.

[119] S. K. Sethi and K. Subramanian. Primordial magnetic fields in the post-recombination era and early reionization. MNRAS, 356:778–788, January 2005.

[120] J. Chluba, D. Paoletti, F. Finelli, and J. A. Rubiño-Martín. Effect of primordial magnetic fields on the ionization history. MNRAS, 451:2244–2250, August 2015.

[121] Shohei Saga, Hiroyuki Tashiro, and Shuichiro Yokoyama. Magnetic reheating. MNRAS, 474(1):L52–L55, February 2018.

[122] Karsten Jedamzik, Višnja Katalinić, and Angela V. Olinto. Limit on Primordial Small-Scale Magnetic Fields from Cosmic Microwave Background Distortions. Phys. Rev. Lett., 85(4):700–703, July 2000.

[123] Kerstin E. Kunze and Eiichiro Komatsu. Constraining primordial magnetic fields with distortions of the black-body spectrum of the cosmic microwave background: pre- and post-decoupling contributions. J. Cosmology Astropart. Phys., 2014(1):009, Jan 2014.

[124] Maresuke Shiraishi, Daisuke Nitta, Shuichiro Yokoyama, Kiyotomo Ichiki, and Keitaro Takahashi. Cosmic microwave background bispectrum of vector modes induced from primordial magnetic fields. Phys. Rev. D, 82(12):121302, Dec 2010.

[125] Maresuke Shiraishi, Daisuke Nitta, Shuichiro Yokoyama, Kiyotomo Ichiki, and Keitaro Takahashi. Cosmic microwave background bispectrum of tensor passive modes induced from primordial magnetic fields. Phys. Rev. D, 83(12):123003, Jun 2011.

[126] I. Wasserman. On the origins of galaxies, galactic angular momenta, and galactic magnetic fields. ApJ, 224:337–343, September 1978.

[127] E.-J. Kim, A. V. Olinto, and R. Rosner. Generation of Density Perturbations by Primordial Magnetic Fields. ApJ, 468:28, September 1996.

[128] M. Fukugita and M. Kawasaki. Reionization during Hierarchical Clustering in a Universe Dominated by Cold Dark Matter. MNRAS, 269:563, August 1994.

[129] F. H. Shu. *The physics of astrophysics. Volume II: Gas dynamics.* 1992.

[130] S. Seager, D. D. Sasselov, and D. Scott. How Exactly Did the Universe Become Neutral? ApJS, 128:407–430, June 2000.

[131] S. Seager, D. D. Sasselov, and D. Scott. A New Calculation of the Recombination Epoch. ApJ, 523:L1–L5, September 1999.

[132] R. A. Sunyaev and Y. B. Zeldovich. Distortions of the Background Radiation Spectrum. Nature, 223:721–722, August 1969.

[133] Y. B. Zeldovich and R. A. Sunyaev. The Interaction of Matter and Radiation in a Hot-Model Universe. Ap&SS, 4:301–316, July 1969.

[134] J. E. Carlstrom, G. P. Holder, and E. D. Reese. Cosmology with the Sunyaev-Zel'dovich Effect. ARA&A, 40:643–680, 2002.

[135] M. Hasselfield, M. Hilton, T. A. Marriage, G. E. Addison, L. F. Barrientos, N. Battaglia, E. S. Battistelli, J. R. Bond, D. Crichton, S. Das, M. J. Devlin, S. R. Dicker, J. Dunkley, R. Dünner, J. W. Fowler, M. B. Gralla, A. Hajian, M. Halpern, A. D. Hincks, R. Hlozek, J. P. Hughes, L. Infante, K. D. Irwin, A. Kosowsky, D. Marsden, F. Menanteau, K. Moodley, M. D. Niemack, M. R. Nolta, L. A. Page, B. Partridge, E. D. Reese, B. L. Schmitt, N. Sehgal, B. D. Sherwin, J. Sievers, C. Sifón, D. N. Spergel, S. T. Staggs, D. S. Swetz, E. R. Switzer, R. Thornton, H. Trac, and E. J. Wollack. The Atacama Cosmology Telescope: Sunyaev-Zel'dovich selected galaxy clusters at 148 GHz from three seasons of data. J. Cosmology Astropart. Phys., 7:008, July 2013.

[136] D. C. Pan, M. S. Vogeley, F. Hoyle, Y.-Y. Choi, and C. Park. Cosmic voids in Sloan Digital Sky Survey Data Release 7. MNRAS, 421:926–934, April 2012.

[137] S. R. Furlanetto, S. P. Oh, and F. H. Briggs. Cosmology at low frequencies: The 21 cm transition and the high-redshift Universe. Phys. Rep., 433:181–301, October 2006.

[138] S. A. Wouthuysen. On the excitation mechanism of the 21-cm (radio-frequency) interstellar hydrogen emission line. AJ, 57:31–32, 1952.

[139] G. B. Field. The Spin Temperature of Intergalactic Neutral Hydrogen. ApJ, 129:536, May 1959.

[140] Jonathan R. Pritchard and Abraham Loeb. 21 cm cosmology in the 21st century. *Reports on Progress in Physics*, 75(8):086901, August 2012.

[141] Andrei Mesinger, Steven Furlanetto, and Renyue Cen. 21CMFAST: a fast, seminumerical simulation of the high-redshift 21-cm signal. MNRAS, 411(2):955–972, February 2011.

[142] Judd D. Bowman, Alan E. E. Rogers, Raul A. Monsalve, Thomas J. Mozdzen, and Nivedita Mahesh. An absorption profile centred at 78 megahertz in the sky-averaged spectrum. Nature, 555(7694):67–70, March 2018.

[143] S. J. Clark, B. Dutta, Y. Gao, Y.-Z. Ma, and L. E. Strigari. 21 cm limits on decaying dark matter and primordial black holes. Phys. Rev. D, 98(4):043006, August 2018.

[144] A. Hektor, G. Hütsi, L. Marzola, M. Raidal, V. Vaskonen, and H. Veermäe. Constraining primordial black holes with the EDGES 21-cm absorption signal. Phys. Rev. D, 98(2):023503, July 2018.

[145] A. Mitridate and A. Podo. Bounds on Dark Matter decay from 21 cm line. J. Cosmology Astropart. Phys., 5:069, May 2018.

[146] H.-C. Cheng, L. Li, and R. Zheng. Coscattering/coannihilation dark matter in a fraternal twin Higgs model. *Journal of High Energy Physics*, 9:98, September 2018.

[147] G. D'Amico, P. Panci, and A. Strumia. Bounds on Dark-Matter Annihilations from 21-cm Data. Phys. Rev. Lett., 121(1):011103, July 2018.

[148] M. Safarzadeh, E. Scannapieco, and A. Babul. A Limit on the Warm Dark Matter Particle Mass from the Redshifted 21 cm Absorption Line. ApJ, 859:L18, June 2018.

[149] S. Yoshiura, K. Takahashi, and T. Takahashi. Impact of EDGES 21-cm global signal on the primordial power spectrum. Phys. Rev. D, 98(6):063529, September 2018.

[150] S. K. Sethi and K. Subramanian. Primordial magnetic fields in the post-recombination era and early reionization. MNRAS, 356:778–788, January 2005.

[151] H. Tashiro and N. Sugiyama. Probing primordial magnetic fields with the 21-cm fluctuations. MNRAS, 372:1060–1068, November 2006.

[152] M. Shiraishi, H. Tashiro, and K. Ichiki. 21Â cm fluctuations from primordial magnetic fields. Phys. Rev. D, 89(10):103522, May 2014.

[153] Kerstin E. Kunze. 21 cm line signal from magnetic modes. J. Cosmology Astropart. Phys., 2019(1):033, January 2019.

[154] D. R. G. Schleicher, R. Banerjee, and R. S. Klessen. Influence of Primordial Magnetic Fields on 21 cm Emission. ApJ, 692:236–245, February 2009.

[155] S. K. Sethi and K. Subramanian. Primordial magnetic fields and the HI signal from the epoch of reionization. J. Cosmology Astropart. Phys., 11:021, November 2009.

[156] D. R. G. Schleicher, R. Banerjee, and R. S. Klessen. Reionization: A probe for the stellar population and the physics of the early universe. Phys. Rev. D, 78(8):083005, October 2008.

[157] J. D. Bowman, A. E. E. Rogers, R. A. Monsalve, T. J. Mozdzen, and N. Mahesh. An absorption profile centred at 78 megahertz in the sky-averaged spectrum. Nature, 555:67–70, March 2018.

[158] A. Blanchard and J. Schneider. Gravitational lensing effect on the fluctuations of the cosmic background radiation. A&A, 184(1-2):1–6, October 1987.

[159] J. P. Ostriker and E. T. Vishniac. Generation of Microwave Background Fluctuations from Nonlinear Perturbations at the ERA of Galaxy Formation. ApJ, 306:L51, July 1986.

[160] Y. Shibusawa, K. Ichiki, and K. Kadota. The influence of primordial magnetic fields on the spherical collapse model in cosmology. J. Cosmology Astropart. Phys., 8:017, August 2014.

[161] J. Richard Shaw and Antony Lewis. Constraining primordial magnetism. Phys. Rev. D, 86(4):043510, August 2012.

[162] Kandaswamy Subramanian and John D. Barrow. Microwave Background Signals from Tangled Magnetic Fields. Phys. Rev. Lett., 81(17):3575–3578, October 1998.

[163] Massimo Giovannini. Tight coupling expansion and fully inhomogeneous magnetic fields. Phys. Rev. D, 74(6):063002, September 2006.

[164] Teppei Minoda, Kenji Hasegawa, Hiroyuki Tashiro, Kiyotomo Ichiki, and Naoshi Sugiyama. Thermal Sunyaev-Zel'dovich effect in the intergalactic medium with primordial magnetic fields. Phys. Rev. D, 96(12):123525, Dec 2017.

[165] M. Abramowitz and I. A. Stegun. *Handbook of Mathematical Functions*. 1972.

Appendix A

Special functions

A.1 Bessel function

Bessel's differential equation for any complex number l is given by

$$x^2\frac{d^2y}{dx^2}+x\frac{dy}{dx}+(x^2-l^2)y=0\ . \tag{A.1}$$

For non-negative integer $l=0,1,2,...$, two linearly independent solutions are obtained

$$J_l(x)=\sum_{m=0}^{\infty}\frac{(-1)^m}{m!\Gamma(m+l+1)}\left(\frac{x}{2}\right)^{2m+l}\ , \tag{A.2}$$

$$N_l(x)=\lim_{\alpha\to l}\frac{J_\alpha(x)\cos(\alpha\pi)-J_{-\alpha}(x)}{\sin(\alpha\pi)}\ . \tag{A.3}$$

Here, $\Gamma(\alpha)$ is Euler's gamma function for real number α.

In the polar coordinates system, there are useful functions as the solutions of the differential equation,

$$\frac{d^2y}{dx^2}+\frac{2}{x}\frac{dy}{dx}+\left[1-\frac{l(l+1)}{x^2}\right]y=0\ . \tag{A.4}$$

The equation is called the spherical Bessel differential equation. The solu-

tions for Eq. (A.4) are written as

$$j_l(x) = \left(\frac{\pi}{2x}\right)^{\frac{1}{2}} J_{l+\frac{1}{2}}(x) \ , \tag{A.5}$$

$$n_l(x) = \left(\frac{\pi}{2x}\right)^{\frac{1}{2}} N_{l+\frac{1}{2}}(x) \ . \tag{A.6}$$

They are called the spherical Bessel functions of the first kind and second kind (also known as the spherical Neumann functions), respectively.

The recurrence relation for the first kind spherical Bessel function is

$$j_{l-1} + j_{l+1} = \frac{2l+1}{x} j_l, \qquad l = 1, 2, ... \tag{A.7}$$

$$l j_{l-1} - (l+1) j_{l+1} = (2l+1)\frac{dj_l}{dx}, \qquad l = 0, 1, 2, ... \tag{A.8}$$

Removing j_{l-1} from these three-term recurrence relations, we obtain the following two-term recurrence relation as

$$j_{l+1} = \frac{l}{x} j_l - \frac{dj_l}{dx} \ . \tag{A.9}$$

For $l = 0$, we solve Eq. (A.4) and obtain

$$j_0(x) = \frac{\sin x}{x} \ . \tag{A.10}$$

From the two-term recurrence relation (A.9), the Bessel function of the first kind for $l = 0, 1, 2, ...$ is generally expressed by

$$j_l(x) = (-1)^l x^l \left(\frac{1}{x}\frac{d}{dx}\right)^l j_0(x) \ . \tag{A.11}$$

This is called Rayleigh's formula of the spherical Bessel function.

A.2 Legendre polynomial and spherical harmonics

Legendre polynomial in order of a non-negative integer n is defined as the solution of the following equation

$$(1-x^2)\frac{d^2 P_n}{dx^2} - 2x\frac{dP_n}{dx} + n(n+1)P_n = 0 \ , \tag{A.12}$$

in range for $-1 \leq x \leq 1$. We note that this solution is normalized as

$$P_n(1) = 1 \ . \tag{A.13}$$

Legendre polynomial satisfies the three-term recurrence relation

$$(2n+1)xP_n - nP_{n-1} = (n+1)P_{n+1} \ , \tag{A.14}$$

and

$$nxP_n - nP_{n-1} = (x^2-1)\frac{dP_n}{dx} \ . \tag{A.15}$$

These relations are called Bonnet's recursion formula, and equivalently represented as

$$P_{n+1} = xP_n + \frac{x^2-1}{n+1}\frac{dP_n}{dx} \ . \tag{A.16}$$

Eq. (A.12) and (A.13) lead

$$P_0(x) = 1 \ . \tag{A.17}$$

Substituting this into Eq. (A.16), the Legendre polynomials are concretely written down as

$$P_1(x) = x, \ \ P_2(x) = \frac{3x^2-1}{2}, \ \ P_3(x) = \frac{5x^3-3x}{2}, \ \ ..., \tag{A.18}$$

and generally expressed by

$$P_n(x) = \frac{1}{n!2^n}\frac{d^n}{dx^n}(x^2-1)^n \ . \tag{A.19}$$

The latter representation is commonly called the Rodrigues' formula of the Legendre polynomials. We note that the Legendre polynomials satisfy

$$P_n(-x) = (-1)^n P_n(x) \ , \tag{A.20}$$

under a parity transformation. We can find that $P_n(x)$ is a n-th order polynomial from Eq. (A.19). Then, we use the following relation

$$\begin{aligned} \frac{d^2}{dx^2}(x^2-1)^n &= \frac{d^2}{dx^2}\sum_{m=0}^{n}(-1)^{n-m}\frac{n!x^{2m}}{m!(n-m)!} \\ &= \sum_{m=0}^{n}(-1)^{n-m}\frac{n!2m(2m-1)}{m!(n-m)!}x^{2m-2} \end{aligned} \tag{A.21}$$

and Eq. (A.19) to obtain

$$P_n(x) = \frac{1}{2^n} \sum_{m=[n/2]}^{n} (-1)^{n-m} \frac{2m(2m-1)\cdots(2m-n+1)}{m!(n-m)!} x^{2m-n} \ . \quad \text{(A.22)}$$

Here, $[n/2]$ is the floor function of $n/2$ introduced by Gauss, which is the largest integer less than or equal to $n/2$. Then we can rewrite Eq. (A.22) as the summation for $k = n - m$, and obtain the simple expression by multiplying the numerator and the denominator by $(n-2k)!$. Finally the general formula of Legendre polynomials is

$$P_n(x) = \frac{1}{2^n} \sum_{k=0}^{[n/2]} \frac{(-1)^k (2n-2k)!}{k!(n-k)!(n-2k)!} x^{n-2k} \ . \quad \text{(A.23)}$$

Here, we discuss the orthogonality of the Legendre polynomials. By multiplying Eq. (A.19) by x^m, where m is an integer such that $0 \leq m < n$, and integrating for x, we can derive

$$\begin{aligned} \int_{-1}^{1} x^m P_n(x) dx &= \frac{1}{n! 2^n} \int_{-1}^{1} x^m \frac{d^n}{dx^n} (x^2-1)^n dx \\ &= (-1)^m \frac{m!}{n! 2^n} \int_{-1}^{1} \frac{d^{n-m}}{dx^{n-m}} (x^2-1)^n dx = 0 \ . \end{aligned} \quad \text{(A.24)}$$

In the second line, we integrate by parts m times, and used the fact that the surface term (x^2-1) goes to zero. Because $P_n(x)$ is orthogonal to x^m for $m < n$ and $P_n(x)$ is a polynomial of n-th order, each Legendre polynomial is orthogonal to all others as

$$\int_{-1}^{1} P_n(x) P_m(x) dx = 0, \quad m \neq n. \quad \text{(A.25)}$$

$$\int_{-1}^{1} P_n^2(x) dx = \frac{(-1)^n}{4^n (n!)^2} \int_{-1}^{1} dx (x^2-1)^n \frac{d^{2n}}{dx^{2n}} (x^2-1)^n \ . \quad \text{(A.26)}$$

Using

$$\int_{-1}^{1} (x^2-1)^n dx = (-1)^n \frac{\sqrt{\pi}\Gamma(n+1)}{\Gamma\left(n+\frac{3}{2}\right)} \ , \quad \text{(A.27)}$$

and

$$\frac{d^{2n}}{dx^{2n}} (x^2-1)^n = (2n)! \ , \quad \text{(A.28)}$$

Eq. (A.26) leads to

$$\int_{-1}^{1} P_n^2(x)dx = \frac{2}{2n+1} \, . \tag{A.29}$$

From Eqs. (A.25) and (A.29), Legendre polynomials for $-1 \leq x \leq 1$ are orthonormalized by

$$\int_{-1}^{1} P_n(x)P_m(x)dx = \frac{2\delta_{nm}}{2n+1} \, . \tag{A.30}$$

We can expand the plane wave with the Legendre polynomials as

$$\mathrm{e}^{-ix\cos\theta} = \sum_{l=0}^{\infty}(2l+1)(-i)^l j_l(x)P_l(\cos\theta) \, . \tag{A.31}$$

We introduce a new variable $y = \cos\theta$, and rewrite Eq. (A.31) as

$$\int_{-1}^{1} \mathrm{e}^{-ixy}P_n(y)dy = 2(-i)^n j_n(x). \tag{A.32}$$

Legendre polynomial is asymptotically expressed by

$$P_n(\cos\theta) = \sqrt{\frac{2}{n\pi\sin\theta}}\cos\left[\left(n+\frac{1}{2}\right)\theta - \frac{\pi}{4}\right] + \mathcal{O}\left(\frac{1}{n^{\frac{3}{2}}}\right) \, , \tag{A.33}$$

for large n [165]. We can find that $P_n(\cos\theta)$ oscillates with the period of $2\pi/n$ for large n.

The spherical harmonics are given by

$$Y_{lm}(\theta,\phi) = (-1)^{\frac{m+|m|}{2}} \cdot \sqrt{\frac{2l+1}{4\pi}\frac{(l-|m|)!}{(l+|m|)!}} \cdot \sin^{|m|}\theta \cdot \frac{d^{|m|}P_l(\cos\theta)}{(d\cos\theta)^{|m|}} \cdot \mathrm{e}^{im\phi} \, , \tag{A.34}$$

and they satisfy

$$\int d\mathbf{n} \; Y^*_{lm}(\mathbf{n})Y_{l'm'}(\mathbf{n}) = \int \sin\theta \; d\theta \; d\phi \; Y^*_{lm}(\theta,\phi)Y_{l'm'}(\theta,\phi) = \delta_{ll'}\delta_{mm'} \, . \tag{A.35}$$

The asymptotic form of the spherical harmonics is

$$Y_{lm}(\theta,\phi) = \frac{1}{\pi\sqrt{\sin\theta}}\cos\left[\left(l+\frac{1}{2}\right)\theta - \frac{\pi}{4} + \frac{m\pi}{2}\right] \cdot \mathrm{e}^{im\phi} + \mathcal{O}\left(\frac{1}{l}\right) \, . \tag{A.36}$$

This asymptotic form is valid for $l \gg 1, l \gg m$.